Pion Structure from the Lattice

Dissertation

zur Erlangung des Doktorgrades
der Naturwissenschaften (Dr. rer. nat.)
der naturwissenschaftlichen Fakultät II – Physik
der Universität Regensburg

vorgelegt von
Dirk Brömmel
aus Regensburg

Mai 2007

Promotionsgesuch eingereicht am:		25.05.2007
Die Arbeit wurde angeleitet von:		Prof. Dr. A. Schäfer
Prüfungsausschuß:	Vorsitzender:	Prof. Dr. F.J. Gießibl
	1. Gutachter:	Prof. Dr. A. Schäfer
	2. Gutachter:	Dr. M. Diehl
	weiterer Prüfer:	Prof. Dr. J. Fabian

Contents

Preface

Today's established description of particles and their interactions are incorporated into the standard model of particle physics. It can be seen as a combination of very successful relativistic quantum field theories, as there are: the electro-weak theory, unifying weak interactions and the electromagnetic force, and *Quantum Chromodynamics* (QCD) describing the strong force. Still missing for a true 'theory of everything' is the fourth fundamental force, gravity. Leaving aside gravity, we know that extensions to the standard model are inevitable, e.g. from cosmological observations that find unexplained non-baryonic dark matter or from neutrino oscillations which require massive neutrinos. These extensions, however, enter only at energies present for example shortly after the big bang. Hence the standard model remains the valid effective description for physics at lower energies. In particular, QCD is the accepted theory of the strong force, which is a conviction, coming from a long history of fascinating physics that can and will be explained with QCD.

Originating in the need for an additional *colour charge* to keep the Pauli principle intact for certain particles like the Δ^{++}-resonance, QCD turned out to be responsible for many more aspects of modern physics. Most prominent here is *asymptotic freedom*, which states that the strength of the interaction of the particles of the theory, *quarks* and *gluons*, becomes weaker at higher energies until the particles can be treated as quasi-free. Conversely, at very small energy scales, colour *confinement* occurs that makes it impossible to find free quarks or gluons. The two extremes are covered by the running of the coupling and explained within QCD.

These two energy regions are also rather distinct in terms of the applicable calculational tools. At high energies, a perturbative expansion in the coupling constant can be made, well suited for calculations of scattering experiments at particle accelerators. On the other hand, a description of the particle spectrum or the internal dynamics of particles is governed by long distance physics. Since the effective degrees of freedom at these low energies are pions, an effective theory based on pions, the so-called chiral perturbation theory, is one possibility for a description of low energy QCD. Another, in some sense more powerful approach, was developed by K. Wilson in 1974. He proposed the *lattice regularisation* for gauge theories, working in a discretised, Euclidean space-time. This has several advantages. First of all, the finite lattice spacing removes ultra-violet divergencies appearing in loop integrals. Combined with a finite volume that suppresses infrared divergencies, one arrives at a rigorous mathematical formulation of QCD. Second, the similarity of this Euclidean formulation and statistical mechanics made the numerical solution of QCD possible. So by numerically evaluating path integral expressions, the lattice approach provides insight into QCD from first principles. However, what turns out to be necessary for mathematical rigour is at the same time connected to inherent limitations of lattice QCD. Even though computational power has continuously increased over the years and substantial algorithmic improvements have been made, lattice simulations still suffer from rather large lattice spacings and small physical volumes, and it is not possible to perform simulations at realistic quark masses. Thus, in order to arrive at physical

meaningful quantities that can be compared to experiments, one has to extrapolate to the physical pion mass and find the continuum and infinite volume limit.

In this work, we will apply lattice QCD to investigate the inner structure of hadrons. More precisely, we compute matrix elements that are related to probability densities of quarks inside the pion, the lightest mesonic bound state of a quark and anti-quark. We already mentioned the importance of the pion for low energy dynamics. It also plays a central rôle in the breaking of chiral symmetry. While its global features like charge, spin and isospin are well known, little is known about its internal structure. Because of the aforementioned confining nature of QCD, perturbative calculations cannot describe physics at the related hadronic energy scales and the lattice provides important theoretical input for understanding the formation of hadrons.

The detailed description of the microscopic structure of hadrons in terms of quarks and gluons is obtained from the concept of *generalised parton distributions* (GPDs). These generalised distributions have matured to a powerful tool leading to many new observations, like for example the distribution of transverse quark spin inside hadrons. GPDs combine well known phenomenological functions like distribution amplitudes, parton distributions and form factors. The latter have their analogues in atomic physics forming our foundation of the understanding of matter.

Outline of this work

We begin in Chapter 1 with a short introduction to QCD phenomenology, stressing where non-perturbative effects are important. In Chapter 2 we then discuss some aspects of GPDs starting with an intuitive picture. After a definition of GPDs for the pion we also focus on the generalised form factors that can be calculated on the lattice. This is followed by a chapter on the basic ingredients of lattice QCD, where we recall the QCD Lagrangian and the path integral formalism before we elaborate on our choice of lattice actions. We will pay special attention to the lattice techniques necessary for the calculation of matrix elements in Chapter 4. The introduction is then completed by explaining how the observables are extracted from the lattice data.

To start the discussion of our results, we take a brief look at pion two-point functions from which pion energies are obtained. The pion electromagnetic form factor is the subject of Chapter 6. We use it to introduce our analysis techniques and discuss in detail the limits to arrive at meaningful physical numbers. Furthermore, we make an attempt to connect to chiral perturbation theory. The discussion of our results then continues with higher moments of the pion structure in Chapter 7. This includes information about well known parton distribution functions that are also obtained from experiments. Finally, we will stress the importance of our work in the context of the transverse spin structure of hadrons, by presenting an outlook on results that can be expected for the pion in the near future. We then close with a summary.

1 Introduction to Phenomenology

Quantum Chromodynamics (QCD) is the theory of the strong force. The particles described by this field theory are *quarks* and gauge bosons which mediate the strong force. Quarks are of spin $\frac{1}{2}$, carry (fractional) electric and colour charge and come in three generations or families, with flavours *up*, *down*, *charm*, *strange*, *top*, and *bottom*:

$$\underset{\text{increasing mass}}{\overrightarrow{\begin{pmatrix}\mathrm{u}\\ \mathrm{d}\end{pmatrix}\ \begin{pmatrix}\mathrm{c}\\ \mathrm{s}\end{pmatrix}\ \begin{pmatrix}\mathrm{t}\\ \mathrm{b}\end{pmatrix}}} \qquad \begin{matrix}+2/3e\\ -1/3e\end{matrix}$$

In this work, we will only be concerned with the light u and d quarks.

The gauge bosons on the other hand, which provide the interaction between the quarks are *gluons* that themselves have colour charge. This causes *self-interaction* between the gluons and makes QCD considerably more involved than Quantum Electrodynamics (QED). Another consequence is that there are no free quarks or gluons – known as *confinement*.

This chapter aims at providing a first idea of QCD and introduces two experimental observables substantiating it. At the same time, these two processes marked the beginning of the successful description of hadronic structure. They do not depend on any special hadron, we will however already focus on the pion here. Furthermore, the two processes can be seen as special cases of a more general framework that will be introduced in the following chapter and that is the motivation of this work.

Since this is a brief introduction only, we refer to standard textbooks like [1, 2, 3] for more details and an in-depth discussion. We also motivate where lattice QCD can provide non-perturbative input to these processes.

1.1 Asymptotic freedom vs Confinement

One of the remarkable features of QCD was already mentioned in the preface: the running of the coupling constant that finally causes *asymptotic freedom*. This can be shown using the β-function that provides the rate of change of the coupling constant with the energy scale μ

$$\frac{\mathrm{d}g(\mu)}{\mathrm{d}(\log\mu^2)} = \beta(g)\,. \tag{1.1}$$

For a non-Abelian $SU(3)$ gauge theory, one finds [2]

$$\beta(g) = -\frac{g^3}{(4\pi)^2}\left(11 - \frac{2}{3}N_\mathrm{f}\right) < 0 \quad \text{for } N_\mathrm{f} \leq 16\,. \tag{1.2}$$

Here N_f is the number of fermion species. The differential equation Eq. (1.1) can be solved perturbatively and to lowest order gives

$$g^2(\mu) = \frac{g^2}{1 - \beta(g)\log(\mu^2/\mu_0^2)}\,, \tag{1.3}$$

with some initial integration scale μ_0. At high energy scales μ and not too many flavours of fermions, the coupling constant is hence found to decrease (as is the case for QCD). This is known as asymptotic freedom since then quarks no longer interact and can be treated as 'free' particles. High energy scales can be reached in experiments where particles collide with high momenta, providing information on short distances.

The other extreme is no less important and valid for our investigation: if the energy scale becomes smaller and smaller, the coupling constant of the theory grows logarithmically, binding quarks into hadrons giving rise to *confinement*. Perturbative methods break down and no longer provide a valid description. Non-perturbative methods that do not rely on a small coupling constant have to take over.

While QCD is successful in describing certain experimental processes at high energies, most of them inevitably contain also soft or long distance parts if only for the initial and final states which are confined to hadrons. We will try and picture two examples in the following, leading to the application of lattice QCD.

1.2 Form Factors

A form factor relates to the substructure of a particle and appears for example in elastic electron scattering. The fact that, e.g. nucleons do have an internal structure was discovered back in the 1950's. At that time experiments at SLAC found that the corresponding Dirac and Pauli form factors were not constant with respect to the probing momentum transfer, as they should be for point-like particles [4]. For the differential cross section this can be seen from

$$\frac{\mathrm{d}\sigma}{\mathrm{d}\Omega} = \left(\frac{\mathrm{d}\sigma}{\mathrm{d}\Omega}\right)_{\text{point}} \left|F(q^2)\right|^2\,, \tag{1.4}$$

where the form factor is denoted by F and q is the momentum transfer. The electromagnetic (point-like) part of the underlying scattering amplitude can be calculated using perturbation theory. The remaining form factor is the so-called soft part of the process and is not accessible in the same way. Its calculation requires the use of non-perturbative methods like for example lattice QCD.

The Feynman diagram for elastic scattering of an electron off a pion is shown in Fig. 1.1 where we also define the momenta of the particles. The scattering amplitude from initial to final state is given by

$$T_\mathrm{fi} = (-\mathrm{i}e)^2\,\bar{u}(k')\gamma^\mu u(k)\,\frac{-\mathrm{i}}{q^2}\,\left\langle \pi^+(\boldsymbol{p}')\right|V_\mu(0)\left|\pi^+(\boldsymbol{p})\right\rangle\,, \tag{1.5}$$

with u, $\bar{u}$ electron spinors and the vector current between the two pion states defined as

$$V_\mu(x) = \frac{2}{3}\bar{u}(x)\gamma_\mu u(x) - \frac{1}{3}\bar{d}(x)\gamma_\mu d(x)\,. \tag{1.6}$$

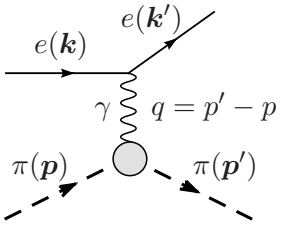

Figure 1.1 | A diagram for pion-electron scattering, with momentum transfer $q = p' - p$.

Here u and d refer to the two light quarks involved. The matrix element in Eq. (1.5) contains the pion form factor F_π in the following way

$$\left\langle \pi^+(\boldsymbol{p}') \right| V_\mu(0) \left| \pi^+(\boldsymbol{p}) \right\rangle = (p'_\mu + p_\mu)\, F_\pi(Q^2)\,, \tag{1.7}$$

where we have used $Q^2 = -q^2$. Because of charge conservation we have $F_\pi = 1$ in the forward limit, i.e. for vanishing momentum transfer. Thus the electron only sees the electric charge of the pion. The matrix element on the l.h.s. of Eq. (1.7) can in principle be evaluated using the path integral. This is the soft contribution mentioned above that will be computed from first principles with lattice QCD.

In the non-relativistic limit, the form factor can be related to the charge radius by writing it as the Fourier transform of the charge distribution $\rho(x)$. Assuming spherical symmetry one then finds

$$F_\pi(Q^2) = 1 - \frac{1}{6} \left\langle r^2 \right\rangle Q^2 + \mathcal{O}(Q^4)\,, \tag{1.8}$$

so that the root mean square radius of the pion is given by

$$\left\langle r^2 \right\rangle = -6\, \frac{\mathrm{d}F_\pi(Q^2)}{\mathrm{d}Q^2}\bigg|_{Q^2=0}\,. \tag{1.9}$$

Experimental data for the pion form factor will be shown along with the results from our lattice calculation in Chapter 6.

1.3 Structure Functions

Of course it is not only interesting that hadrons do have an internal structure, we also want to know what the internal degrees of freedom are and what their dynamics is. Today we know that the internal particles are quarks which was first shown at SLAC from *deep inelastic scattering* experiments (DIS) [5]. In these experiments, one has a high energy lepton (usually an electron) scattering off a parton in the probed hadron and thereby producing a different final state: $lh \to lX$, shown in Fig. 1.2. To evaluate the cross section, we start by considering the scattering amplitude T_{fi}. It is similar to that of the form factor, Eq. (1.5), except that the pion now breaks up into the set of final states X

$$T_{\mathrm{fi}} = (-\mathrm{i}e)^2\, \bar{u}(k')\gamma^\mu u(k)\, \frac{-\mathrm{i}}{q^2}\, \left\langle X \right| V_\mu(0) \left| \pi^+(\boldsymbol{p}) \right\rangle\,. \tag{1.10}$$

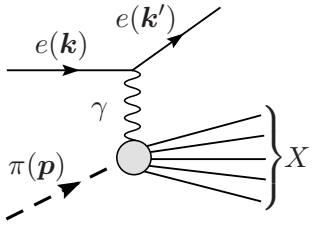

Figure 1.2 | Diagram for deep inelastic scattering of an electron off a pion breaking it up into a number of final states denoted X.

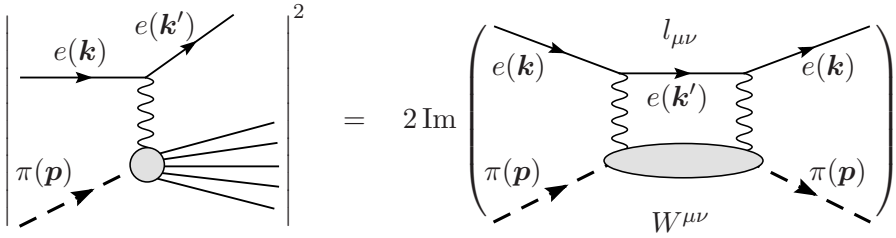

Figure 1.3 | A visualisation of the optical theorem as applied to inclusive scattering. The leptonic and hadronic tensors correspond to the upper and lower parts of the r.h.s. diagram.

As before, the momentum transfer is $q = k - k'$, c.f. Fig. 1.2. For an inclusive process where we sum over all particles X, the optical theorem can be used to relate the forward scattering amplitude and the total cross section. This is sketched in Fig. 1.3 and we obtain

$$\sigma[e^-(\boldsymbol{k})\pi(\boldsymbol{p}) \to e^-(\boldsymbol{k}')X] \propto T_{\mathrm{fi}} T_{\mathrm{fi}}^* = 2\,\mathrm{Im}\, l_{\mu\nu} W^{\mu\nu}\,. \tag{1.11}$$

Here $l_{\mu\nu}$ and $W^{\mu\nu}$ are the leptonic and hadronic tensor. The leptonic tensor can be evaluated perturbatively within QED; we are interested in the hadronic part. In case of the pion it can be parametrised by two structure functions F_1 and F_2

$$W^{\mu\nu} = F_1(x, Q^2)\left(-g^{\mu\nu} + \frac{q^\mu q^\nu}{q^2}\right) + F_2(x, Q^2)\frac{1}{M^2}\left(p^\mu - \frac{p\cdot q}{q^2}q^\mu\right)\left(p^\nu - \frac{p\cdot q}{q^2}q^\nu\right). \tag{1.12}$$

This parametrisation is solely obtained by using Lorentz symmetry and current conservation. At this point, it does not contain any further knowledge.

The information about the structure functions can be improved within the parton model.[1] Due to the very high energies, the electron no longer probes the hadron as one particle, but it rather scatters off the quarks and gluons as quasi-free particles inside the hadron. This is connected to the running of the coupling mentioned in Sec. 1.1 where higher energies imply a smaller coupling constant of the strong force. We are thus leaving the confinement region, entering the region of asymptotic freedom where the partons can be assumed to be free. This is pictorially shown in Fig. 1.4.a. We can think of it as

$$\sigma[e^-(\boldsymbol{k})\pi^+(\boldsymbol{p}) \to e^-(\boldsymbol{k}')X] = \int_0^1 \mathrm{d}x \sum_q q(x) \times \sigma[e^-(\boldsymbol{k})\psi^q(xp) \to e^-(\boldsymbol{k}')\psi^q(\boldsymbol{p}')]\,, \tag{1.13}$$

where $q(x)$ is the probability density of finding a parton ψ^q with the momentum fraction $x = p_q/p$ inside the hadron. To lowest order in the parton model, one finds for the

[1] The term 'parton' refers to (anti-)quarks and gluons as constituents inside hadrons.

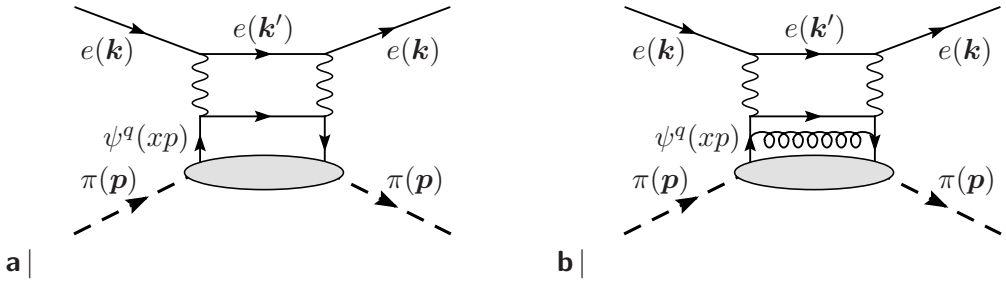

Figure 1.4 | A visualisation of the parton model: **a** | To lowest order. **b** | Including a simple correction where an additional gluon is emitted.

structure functions

$$F_1(x, Q^2) = \sum_q \frac{e_q^2}{2} \left[q(x) + \bar{q}(x)\right] \tag{1.14}$$

$$F_2(x, Q^2) = 2x\, F_1(x, Q^2)\,. \tag{1.15}$$

where the sum runs over the different quarks, weighted with their charge e_q. The second line is known as Callan-Gross relation, reflecting the spin $\frac{1}{2}$ nature of the quarks.

To this order, the cross section is independent of the square of the probing momentum transfer Q^2 and neglecting any interaction between the struck quark and the spectators that 'remain in the pion'. This approximate relation is known as Bjorken scaling. Corrections to that introduce a logarithmic dependence on Q^2. One such possibility is shown in Fig. 1.4.b. Bjorken scaling, or rather its violation, is very well established for electron-proton scattering, c.f. [6] for recent data.

The parton distribution functions $q(x)$ are universal to the hadron and do not depend on the process considered, thus being of great interest. They cannot be calculated using perturbative QCD. Similar to the form factor, it is a soft process that determines the structure of the hadron as a bound state of quarks and gluons. Again lattice QCD is a tool that can provide input for this by calculating the matrix element appearing in Eq. (1.10). Two recent discussions of the parton distribution functions for the pion as they can be obtained from experiment can be found in [7, 8]. Our lattice results will be subject of Chapter 7.

2 Generalised Parton Distributions

While pure group theory, based on elementary quarks, their spin and colour, successfully explains some features of the particle spectrum [9], QCD as a field theory provides insight to the structure of these bound states. Initial ideas on that and the related processes were the subject of the previous chapter. In recent years a more involved experimental programme and the theoretical framework connected to it prove even more powerful in the description of the internal structure of hadrons. The necessary functions are the *generalised parton distribution functions* – in short GPDs – also known as off-forward or skewed parton distributions.

GPDs are of interest for the solution to a problem referred to as the spin crisis of the nucleon (originating from [10]). This refers to the fact that the total spin of the nucleon is not just the sum of the intrinsic spins of the three valence quarks. In addition, one has to take into account the contribution of the sea quarks and the angular momentum of the quarks and gluons. This can be accomplished using Ji's sum rule [11].

Other prominent results that can be related to GPDs are the so-called single spin asymmetries that arise in different fashion in experiments: the Boer-Mulders [12] and the Sivers effect [13]. In both cases the outcome of the experiment depends crucially on the polarisation of the scattering particles, leading to different densities of the active quark in the transverse plane. According to Burkardt, these densities can be calculated with the help of GPDs [14].

While the above examples were for the nucleon in particular, similar considerations apply to the pion. We will try and mention some aspects of GPDs that are connected to this work. For extensive reviews see [15, 16]. In order to stress the interesting features, we begin in a somewhat unconventional ordering with an outlook on the interpretation of GPDs. This is followed by their definition for the pion case and general properties that will be important for the subsequent chapters. We then give a short summary of the interpretation of GPDs in the transverse plane. Our lattice calculations furthermore require a digression to Mellin moments. We also provide a decomposition of the GPDs into generalised form factors.

2.1 In a Nutshell

We begin the discussion of GPDs with an illustration in order to provide some intuition right from the start. While this seems to be a straightforward interpretation and link between the different observables, there are some subtleties that have to be considered. For simplicity these will mostly be neglected for the moment being.

We have introduced two QCD processes at the end of the previous chapter that can be used to describe some aspects of the internal structure of hadrons. The first one was the pion form factor that, after performing a Fourier transform, is interpreted as charge distribution ρ. Since the particles in accelerators usually have very high momenta

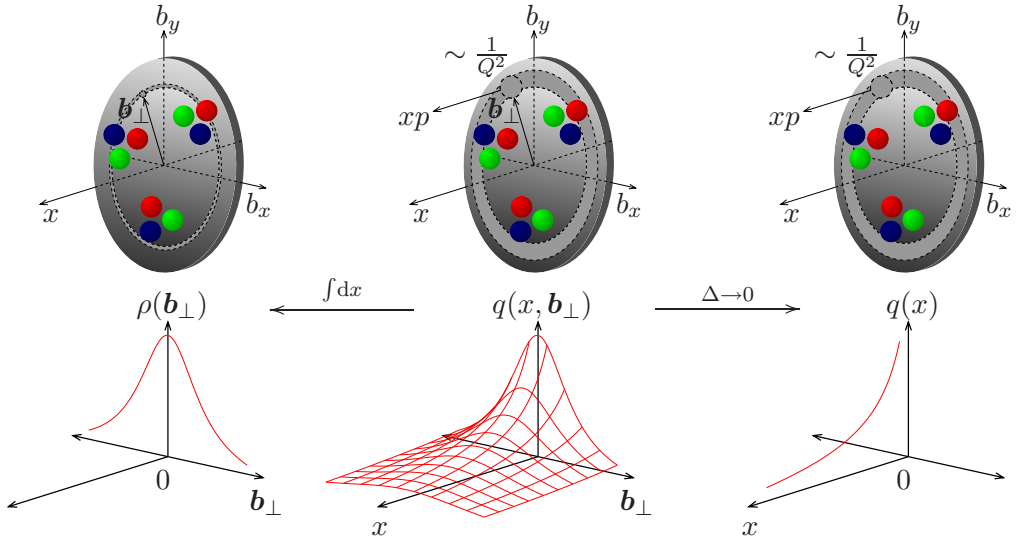

a | Form factor **b** | GPD, $\xi = 0$ **c** | Parton density

Figure 2.1 | A simplified sketch of the different phenomenological observables and their interpretation in the infinite momentum frame: **a** | The form factor as a charge density in the perpendicular plane (after a Fourier transform, Sec. 1.2). **b** | A probabilistic interpretation for GPDs in the case of vanishing longitudinal momentum transfer, $\xi = 0$, with a resolution $\sim 1/Q^2$. **c** | A parton distribution for the forward momentum case (Sec. 1.3). For a detailed explanation see text. [Pictures inspired by [17]]

(conventionally the z-direction) they can be seen as Lorentz contracted 'discs' rather than spherical objects.[1] We will later argue that this infinite momentum frame is necessary for the GPDs. For the moment, we thus think of a two-dimensional distribution with respect to $\boldsymbol{b}_\perp$ in the transverse plane, sketched in Fig. 2.1.a. The z-direction is also suppressed in favour of the fractional (longitudinal) momentum x of the partons.

The second process led to parton distribution functions (PDFs) $q(x)$ with the momentum fraction x carried by the parton. They give the probability of finding the parton q with this momentum inside the hadron and they are sketched in Fig. 2.1.c. One can also give a resolution $\sim 1/Q^2$ that can be resolved inside the hadron. So for different Q^2 partons of a 'different size' can be probed, consequently the parton content of the hadron changes.

To achieve a deeper understanding of the distribution of the quarks inside the hadron, it would be nice to combine the two cases, i.e. know the distribution in the transverse plane for quarks with a given momentum fraction. This is exactly one interpretation of GPDs. During the discussion of the form factor and the PDFs, we already mentioned the similarity of the matrix elements appearing in Eqs. (1.5) and (1.10). The initial and final states of the two processes differed only in their momenta (after applying the optical theorem). There are indeed processes with different asymptotic states that can be related to the two aforementioned, thus coining the term *generalised distributions*. We will later consider the problems arising from the complete freedom of the two momenta. For the moment, note that a density interpretation is possible if the longitudinal momentum transfer ξ vanishes. A Fourier transform of the remaining transverse momentum transfer then yields

[1] Neglecting relativistic corrections, this would not be necessary for the form factor where we have elastic scattering with momenta down to zero.

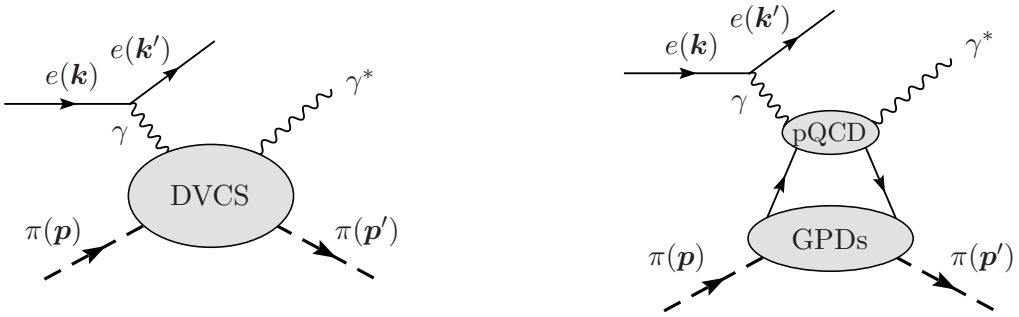

Figure 2.2 | A diagram showing the DVCS amplitude and the factorisation into hard (pQCD) and soft parts (GPDs).

the probability $q(x, \boldsymbol{b}_\perp)$ for finding a quark with momentum fraction x at the position $\boldsymbol{b}_\perp$, the impact parameter, in the transverse plane, Fig. 2.1.b. Since this probability is obtained for all (anti-) quarks including their flavour and a possible polarisation of the quarks, a much richer structure can be accessed.

If one considers suitable limits, the two types of observables discussed before are obtained. Obvious is the forward limit $\Delta \to 0$ for vanishing momentum transfer. The GPDs are then equivalent to the 'usual' parton densities (Fig. 2.1.b → Fig. 2.1.c). Keeping the momentum transfer and integrating over the fraction x carried by the quark is equivalent to the form factor (Fig. 2.1.b → Fig. 2.1.a). The two known cases are thus included in the generalisation to GPDs.

2.2 A Definition for the Pion

After trying to provide some intuition where GPDs can lead to new insights, let us now turn to a rigorous definition. In Section 1.3 we described how high energetic leptons can be used to asses the structure of hadrons in DIS. We considered an inclusive process, where one sums over all final state particles instead of focusing on a specific combination. Via the optical theorem, we could infer to the scattering cross section of the so-called forward Compton amplitude: $\gamma^* h \to \gamma^* h$. On the other hand, there also exists another process in colliding experiments whose amplitude looks similar to the total cross section in DIS: *deeply virtual Compton scattering* (DVCS). This is an exclusive process where the final states are detected. We again have a lepton scattering off a hadron, but this time the hadron stays intact; in addition the scattered lepton and a real photon is detected: $lh \to lh\gamma$.

A factorisation theorem now takes the role of the parton model, separating the DVCS process into a hard (or short distance) and soft (or long distance) part [18]. The first one can be calculated perturbatively while the latter is an intrinsically non-perturbative quantity, parametrised by GPDs. The situation is shown in Fig. 2.2. The amplitude of the process is then found via a convolution of the hard (pQCD) and the soft (GPD) part. The important bit to note is that the DVCS amplitude exhibits the generalisation in terms of initial and final momenta mentioned in the previous section. This happens because the virtual photon γ^* is turned into a real photon γ in the final state, requiring a momentum

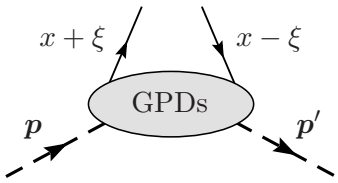

Figure 2.3 | The handbag diagram for GPDs, defining the kinematics.

transfer onto the struck hadron:

$$\left\langle \pi(\boldsymbol{p}') \right| \mathcal{O} \left| \pi(\boldsymbol{p}) \right\rangle \,. \tag{2.1}$$

The initial (final) state here has momentum p^μ (p'^μ) and the GPD is given as an abstract operator $\mathcal{O}$. From Eq. (2.1) we see the GPD no longer represents the square of an amplitude and thus a probability. One rather has an *interference* of two hadrons. This has to be kept in mind for the interpretation of GPDs as announced above.

We define the kinematical variables with the handbag diagram of GPDs in Fig. 2.3. As just said, the momenta of the incoming and outgoing hadron are labelled p^μ and p'^μ, respectively. The parton that leaves and enters the blob has the momentum fraction (of the hadron) $x \pm \xi$. We then define as further variables

$$P^\mu = \frac{1}{2}(p^\mu + p'^\mu)\,, \qquad \Delta^\mu = p'^\mu - p^\mu\,, \qquad t = \Delta^2 \tag{2.2}$$

and have $Q^2 = -q^2$ as before. The skewness parameter ξ is the fractional longitudinal momentum transfer and given by

$$\xi = \frac{p^+ - p'^+}{p^+ + p'^+}\,, \tag{2.3}$$

where we have used light cone coordinates p^+, p'^+ for the pion momenta. Light cone coordinates are defined by

$$\begin{aligned} v^\pm = \frac{1}{\sqrt{2}}\,(v^0 \pm v^3)\,, \quad \boldsymbol{v}_\perp = (v^1, v^2) \\ \text{or } v^+ = vn_-\,, \quad v^- = vn_+ \\ \text{with } n_+ = (1,0,0,1)/\sqrt{2}\,, \quad n_- = (1,0,0,-1)/\sqrt{2}\,. \end{aligned} \tag{2.4}$$

These coordinates are a natural way to describe the infinite momentum frame in which parton distributions can be explained in the physical picture of the parton model. The close connection is evident for the light cone momentum p^+ since it becomes proportional to the momentum of the particle in the infinite momentum frame $p^3 \to \infty$. We will thus use light cone variables for GPDs.

In analogy to the usual parton distribution functions, GPDs can be written as a Fourier transform of matrix elements of quark operators at a light-like separation (we omit gluon operators and the corresponding GPDs since these will not be considered on the lattice).

The pion GPDs are defined by

$$2P^+ \, H^q_\pi(x,\xi,t) = \int \frac{\mathrm{d}z^-}{2\pi} \, e^{\mathrm{i}xP^+z^-} \, \big\langle \pi(\boldsymbol{p}') \big| \, \bar{\psi}^q(-\tfrac{1}{2}z^-) \, \gamma^+ \, \mathcal{U} \, \psi^q(\tfrac{1}{2}z^-) \, \big| \pi(\boldsymbol{p}) \big\rangle \Big|_{\substack{z^+=0 \\ \boldsymbol{z}_\perp=0}} , \tag{2.5a}$$

$$\frac{P^{[+}\Delta^{j]}}{m_\pi} \, E^q_{\mathrm{T},\pi}(x,\xi,t) = \int \frac{\mathrm{d}z^-}{2\pi} \, e^{\mathrm{i}xP^+z^-} \, \big\langle \pi(\boldsymbol{p}') \big| \, \bar{\psi}^q(-\tfrac{1}{2}z^-) \, \mathrm{i}\sigma^{+j} \, \mathcal{U} \, \psi^q(\tfrac{1}{2}z^-) \, \big| \pi(\boldsymbol{p}) \big\rangle \Big|_{\substack{z^+=0 \\ \boldsymbol{z}_\perp=0}} . \tag{2.5b}$$

The GPDs are labelled with H^q_π ($E^q_{\mathrm{T},\pi}$) for the vector (tensor) operator matrix elements and are given for each quark flavour q separately; the index j labels the two transverse components and $^{[\ldots]}$ denotes anti-symmetrisation. We will see in Section 2.6.1 that a GPD from an axial-vector operator vanishes because of time-reversal.[2] The separation on the light cone is denoted with z^-. To ensure gauge invariance of the matrix elements, a Wilson line $\mathcal{U}$ has to be included connecting the two quarks. It is given by

$$\mathcal{U} = \mathcal{P} \exp\left(\mathrm{i}g \int_{-\frac{1}{2}z^-}^{\frac{1}{2}z^-} \mathrm{d}x^- A^+(x^- n_-) \right) , \tag{2.6}$$

where $\mathcal{P}$ indicates a path ordered integral. Note that the Wilson line is identical to one in the light cone gauge defined by $A^+ = 0$ for the gauge fields. For simplicity, we will hence drop the gauge link in the following and assume light cone gauge unless explicitly noted.

The matrix elements in the definition of the pion GPDs, Eqs. (2.5a) and (2.5b), and the diagram connected to it, Fig. 2.2, show that GPDs are more general than the form factor or the structure functions. In contrast to the latter they are not based on model assumptions and in principle contain all the physics. From that point of view they are also far more rigorous. What remains are means to extract the physics from the GPDs, especially in view of their non-probabilistic and non-perturbative nature.

2.3 Some General Properties

After the definition of the pion GPDs H^q_π and $E^q_{\mathrm{T},\pi}$ we take a look at some of their properties and do this by connecting to the discussion at the beginning of this chapter. The GPDs depend on three kinematical variables: the momentum fraction of the struck parton x, the skewness parameter ξ for the momentum transfer and its invariant t. Reducing the number parameters 'de-generalises' the GPDs. We restrict ourselves to the vector case in this section, since the limits we discuss will then recover the well known observables. Let us start with a ...

Parton Interpretation

Looking at the kinematics of the GPDs, we can distinguish three different regions for the momentum fraction x running from -1 to 1, c.f. Fig. 2.4:

[2] In contrast to e.g. the nucleon case where it is then related to polarised GPDs.

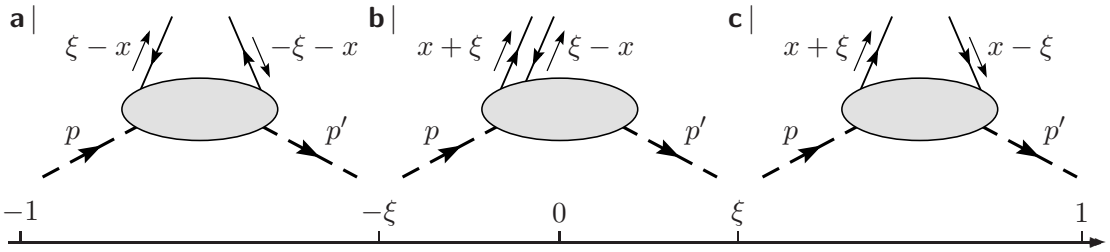

Figure 2.4 | Different kinematical regions in x with their interpretation in the parton model: **a** | emission and reabsorption of anti-quarks, $x \in [-1, -\xi]$. **b** | emission of a quark/anti-quark pair, $x \in [-\xi, \xi]$. **c** | emission and reabsorption of quarks, $x \in [\xi, 1]$.

a | for $x \in [1, -\xi]$ both parton momenta in the handbag diagram (Fig. 2.3) are negative. This corresponds to the emission and reabsorption of anti-quarks. Their momenta are then $\xi - x$ and $-\xi - x$.

b | if the momentum fraction x lies between $-\xi$ and ξ we find that one of the parton lines has positive (or zero) momentum while the other momentum is negative (or zero). We thus have the emission of a quark and anti-quark. The GPDs behave like a meson distribution amplitude and contain new information not accessible in DIS (obtained for $\xi \to 0$).

c | finally, for $x \in [\xi, 1]$ both parton momenta are positive. So in this region a quark is first emitted and then reabsorbed with momenta $x + \xi$ and $x - \xi$.

The Forward Limit

The straight-*forward* limit is when the momentum transfer vanishes: $\Delta \to 0$. In this case the known PDFs are recovered. There are two cases for the values of x:

$x > 0$: corresponding to Fig. 2.4.c, so we have $H^q_\pi(x, 0, 0) = q(x)$,

$x < 0$: equivalent to Fig. 2.4.a and thus $H^q_\pi(x, 0, 0) = -\bar{q}(-x)$.

These are the usual probability densities of finding a (anti-)quark with momentum fraction x. Notice that by extending the interval to $-1 \leq x \leq 1$ the PDFs for (anti-)quarks can practically be combined while still being defined for positive fractions.

The Form Factor

The other interesting limit of GPDs reduces them to form factors as noted in the introduction. The reduction is obtained by

$$\int_{-1}^{1} \mathrm{d}x \, H^q_\pi(x, \xi, t) = F^q(\Delta^2) \,, \tag{2.7}$$

where the superscript denotes the quark flavour. For the 'full' form factor as in Eq. (1.4) we have to sum over the flavours weighting with their charge, e.g. for the π^+

$$F_{\pi^+} = e_u F^u - e_d F^d \,. \tag{2.8}$$

Equation (2.7) can be understood looking at the definition of the GPD, Eq. (2.5a): integrating over x causes a δ-function forcing the quark fields on the same space-time point after the z^- integration. We then have the same matrix element as in Eq. (1.7). This is known as the lowest moment in the momentum fraction x. These Mellin moments are again subject of Sections 2.5-2.7 which will again reveal this relation.

2.4 A Probabilistic Interpretation

From what we have said so far, we see that an easy interpretation of GPDs is only possible for limiting cases, where we either get no information about the momentum of the constituents or we have no insight in their spatial distribution. So new information on the structure of pions beyond the known PDFs and the form factor is encoded in the interplay of x and Δ^2. However, we also noticed that GPDs do not have a probabilistic interpretation straight away because we have different momentum states for the incoming and the outgoing pion. Furthermore, since GPDs depend on the longitudinal momentum fraction of the struck quark, we cannot access the spatial z-coordinate due to Heisenberg's uncertainty principle. On the other hand, it has been shown that with a Fourier transform in the transverse momentum distributions in the transverse plane are conceivable [14, 17, 19, 20, 21]. In the following, we mention some of the necessary arguments and important relations.

Let us start by noting that without taking special care of the reference frame and the shape of the wave packets used to describe the particles, the interpretation of the form factor becomes unclear already. For wave packets that are very localised in position space (smaller than their Compton wave length), the form factor in the rest frame acquires contributions due to the intrinsic size of the wave packet, Lorentz contraction (the localisation implies high momentum) and other relativistic effects. These problems continue to GPDs as well. As it turns out these corrections can be neglected in the infinite momentum frame, thus allowing for a clean physical picture [17].

The key for an interpretation of our observables is the infinite momentum frame and wave packets that are only localised in transverse position. We will define our momentum states as

$$\left|p^+, \boldsymbol{b}_\perp\right\rangle = \int \frac{\mathrm{d}\boldsymbol{p}_\perp}{16\pi^3}\, e^{-\mathrm{i}\boldsymbol{p}_\perp \boldsymbol{b}_\perp} \left|p^+, \boldsymbol{p}_\perp\right\rangle \tag{2.9}$$

leaving the transverse momentum undefined. We can now define a centre of transverse momentum for the pion

$$\boldsymbol{R}_\perp = \frac{\sum_i x_i \boldsymbol{b}_{\perp,i}}{\sum_i x_i} = \sum_i x_i \boldsymbol{b}_{\perp,i}\,, \tag{2.10}$$

where we sum over all partons in the pion. Note that this centre of momentum is in analogy to the centre of mass in non-relativistic situations, [21]. Assuming for the centre of momentum $\boldsymbol{R}_\perp = 0$ we find the active quark at position $\boldsymbol{b}_{\perp,\mathrm{a}}$ whereas the spectators have their centre at $\boldsymbol{b}_{\perp,\mathrm{s}} = \boldsymbol{b}_{\perp,\mathrm{a}}/(1-x) - \boldsymbol{b}_{\perp,\mathrm{s}}$, see Fig. 2.5. Without any additional constraints on the kinematics, the pion changes its position during DVCS [20]. While the system of the incoming and outgoing pion is centred at $\boldsymbol{b}_\perp = 0$, the pion is 'shifted sideways' because the longitudinal momentum transfer ξ on the struck quark changes its momentum fraction and thus its weight inside the pion, Eq. (2.10). However, the matrix elements become diagonal (w.r.t. p^+ and $\boldsymbol{b}_\perp$) for purely transverse momentum transfer

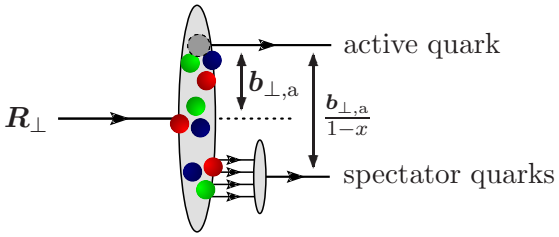

Figure 2.5 | Distances of the active quark and (w.r.t. this parton) of the spectators inside the pion, centred at $\boldsymbol{R}_\perp = 0$.

$\Delta^+ = 0$ or $\xi = 0$ which we will assume for now. Notice that $\xi = 0$ is not possible in DVCS experiments since some longitudinal momentum transfer is required to convert the virtual to a real photon. However, the case $\xi \to 0$ is relevant for DVCS nevertheless. We use a state that is localised at $\boldsymbol{R}_\perp = \boldsymbol{0}_\perp$ and define a transverse (impact parameter dependent) PDF as

$$q(x, \boldsymbol{b}_\perp) = \int \frac{z^-}{2\pi}\, e^{\mathrm{i}xp^+z^-} \left\langle \pi(p'^+, \boldsymbol{0}_\perp) \right| \bar{\psi}_q(-\frac{z^-}{2}, \boldsymbol{b}_\perp)\gamma^+\psi_q(\frac{z^-}{2}, \boldsymbol{b}_\perp) \left| \pi(p^+, \boldsymbol{0}_\perp) \right\rangle , \tag{2.11}$$

where the active parton depends on the impact parameter and where we have again assumed light cone gauge for simplicity. Writing the matrix element in Eq. (2.11) in momentum space and applying a transverse translation to the operator we recover the same form used for the GPDs in Eqs. (2.5a) and (2.5b). We thus have

$$q(x, \boldsymbol{b}_\perp) = \int \frac{\mathrm{d}^2\boldsymbol{\Delta}_\perp}{4\pi^2}\, e^{-\mathrm{i}\boldsymbol{b}_\perp\boldsymbol{\Delta}_\perp} H^q_\pi(x, 0, -\boldsymbol{\Delta}^2_\perp) \quad \text{and} \tag{2.12a}$$

$$q_\mathrm{T}(x, \boldsymbol{b}_\perp) = \int \frac{\mathrm{d}^2\boldsymbol{\Delta}_\perp}{4\pi^2}\, e^{-\mathrm{i}\boldsymbol{b}_\perp\boldsymbol{\Delta}_\perp} E^q_{\mathrm{T},\pi}(x, 0, -\boldsymbol{\Delta}^2_\perp) , \tag{2.12b}$$

for which we also used $\boldsymbol{\Delta}_\perp = \boldsymbol{p}'_\perp - \boldsymbol{p}_\perp$ and the fact that the GPDs do not depend on $(\boldsymbol{p}_\perp + \boldsymbol{p}'_\perp)$.

In order to derive positivity bounds for the transverse distributions and to make the information obtained by them even more explicit, one has to use the wave function representation [14, 21]. The transverse parton distributions can then be interpreted as probability densities.

For a given momentum faction x, the width of the distribution of partons forming the pion is then obtained from

$$\left\langle \boldsymbol{r}^2_\perp \right\rangle_x = \frac{\int \mathrm{d}^2\boldsymbol{b}_\perp\, \boldsymbol{b}^2_\perp\, q(x, \boldsymbol{b}_\perp)}{\int \mathrm{d}^2\boldsymbol{b}_\perp\, q(x, \boldsymbol{b}_\perp)} = 4\frac{\partial}{\partial\boldsymbol{\Delta}^2_\perp} \log H^q_\pi(x, 0, -\boldsymbol{\Delta}^2_\perp) . \tag{2.13}$$

This average impact parameter should vanish as $x \to 1$ because the struck quark gets closer and closer to the centre of momentum defined in (2.10) since its weight increases. Alternatively we expect that $H^q(x, 0, -\boldsymbol{\Delta}^2_\perp)$ becomes independent of $\boldsymbol{\Delta}^2_\perp$ as $x \to 1$.

2.5 Mellin Moments of Generalised Parton Distributions

For a successful application of lattice QCD to GPDs we are facing the problem that we can only calculate local matrix elements on the lattice. However, the matrix elements we

considered so far, Eqs. (2.5a) and (2.5b), are non-local matrix elements with a certain separation z on the light-cone. As it turns out, considering Mellin transformations is a partial solution to that. In general, the $(n+1)$-th Mellin moment of a function f can be written as

$$M_{n+1}(f) = \int \mathrm{d}x\, x^n f(x)\,, \quad \text{with } n = 0, 1, 2, 3, \ldots \tag{2.14}$$

Knowledge of all moments in x makes it possible to find an analytic continuation and perform an inverse Mellin transformation. Knowing all Mellin moments hence is equivalent to knowing the function itself.

We can now look at moments of the light cone operator as it appears in the definition of our pion GPDs, e.g. (2.5a) (in light cone gauge)

$$\int \mathrm{d}x\, x^n \int \frac{\mathrm{d}z^-}{2\pi} e^{\mathrm{i}xP^+z^-} \left[\bar\psi^q(-\tfrac{1}{2}z)\gamma^+\psi^q(\tfrac{1}{2}z)\right]_{z^+=0,\boldsymbol{z}_\perp=0}. \tag{2.15}$$

After an n-fold partial integration with respect to z^- we arrive at

$$\begin{aligned}
&\sum_{m=0}^{n-1} \int \mathrm{d}x\, \frac{-\mathrm{i}}{2\pi}(P^+)^{-(m+1)} x^{n-m} e^{\mathrm{i}xP^+z^-} \left(\mathrm{i}\frac{\mathrm{d}}{\mathrm{d}z^-}\right)^m \left[\bar\psi^q(-\tfrac{1}{2}z)\gamma^+\psi^q(\tfrac{1}{2}z)\right]_{z^+=0,\boldsymbol{z}_\perp=0} \\
&\qquad + \frac{1}{(P^+)^n} \int \mathrm{d}z^- \int \mathrm{d}x\, e^{\mathrm{i}xP^+z^-} \left(\mathrm{i}\frac{\mathrm{d}}{\mathrm{d}z^-}\right)^n \left[\bar\psi^q(-\tfrac{1}{2}z)\gamma^+\psi^q(\tfrac{1}{2}z)\right]_{z^+=0,\boldsymbol{z}_\perp=0} \\
&= \frac{1}{(P^+)^n} \left(\mathrm{i}\frac{\mathrm{d}}{\mathrm{d}z^-}\right)^n \left[\bar\psi^q(-\tfrac{1}{2}z)\gamma^+\psi^q(\tfrac{1}{2}z)\right]_{z=0} = \frac{1}{(P^+)^n} \left[\bar\psi^q(0)\gamma^+ \left(\mathrm{i}\overleftrightarrow{\partial}^+\right)^n \psi^q(0)\right].
\end{aligned} \tag{2.16}$$

The sum in the first line vanishes because the quark fields have to be zero at infinity; the last line is then obtained after evaluating the resulting δ-function in z^- and with using $\overleftrightarrow{\partial} = \frac{1}{2}(\overrightarrow{\partial} - \overleftarrow{\partial})$.

Had we not been using light cone gauge, the additional gauge link would have caused a covariant derivative to appear. Since the lattice does not know about light cone gauge either, we will use the covariant form in the following and replace $\partial^\mu \to D^\mu$.

The GPDs are defined and valid for light cone components only. This corresponds to contracting a general operator with arbitrary indices with n light cone projectors n_-. Hence only symmetrised and traceless operators (representing twist-2 operators from the operator product expansion) contribute. Similar arguments are valid for the tensor GPD. So from the non-local operators, taking Mellin moments we finally arrive at towers of local bilinear operators

$$\mathcal{O}_q^{\{\mu\mu_1\ldots\mu_n\}}(0) = \bar\psi^q(0)\,\gamma^{\{\mu}\mathrm{i}\overleftrightarrow{D}^{\mu_1}\ldots\mathrm{i}\overleftrightarrow{D}^{\mu_n\}}\,\psi^q(0) - \text{traces}\,, \tag{2.17a}$$

$$\mathcal{O}_{q,\mathrm{T}}^{[\mu\{\nu]\mu_2\ldots\mu_n\}}(0) = \bar\psi^q(0)\,\mathrm{i}\sigma^{[\mu\{\nu]}\mathrm{i}\overleftrightarrow{D}^{\mu_2}\ldots\mathrm{i}\overleftrightarrow{D}^{\mu_n\}}\,\psi^q(0) - \text{traces}\,. \tag{2.17b}$$

The $^{\{\ldots\}}$ and $^{[\ldots]}$ refer to symmetrisation and anti-symmetrisation of the indices (performed in this order). The subtracted trace terms are of the form $g_{\mu_i\mu_j}\mathcal{O}^{\mu_1\ldots\mu_i\ldots\mu_j\ldots\mu_n} = 0$.

2.6 Generalised Form Factors

The previous section outlined the relation between the non-local bi-linear matrix elements and their local counterparts appearing in the definition of GPDs. Matrix elements of

the individual operators from the towers of operators of Eqs. (2.17a) and (2.17b) can be parametrised into generalised form factors (GFFs) with some kinematical pre-factors. This is similar to decomposing the hadronic tensor into the structure functions in Sec. 1.3. In this section, we will also include the axial vector current for which we claimed that the GPDs vanish.

2.6.1 Counting Generalised Form Factors

We start by counting the number of GFFs for the individual operators. This will present a check of the actual decomposition we derive in the following section. Of course a check only makes sense if the number of occurring terms is found with a different method.

Here, the counting of GFFs is done analogous to [22, 23]. The idea is that instead of studying off-forward matrix elements like $\langle \pi | \, \mathcal{O} \, | \pi \rangle$ one can consider the crossed channel with matrix elements between a two particle continuum state and the vacuum, $\langle 0 | \, \mathcal{O} \, | \pi\bar{\pi} \rangle$. The task then is to match the quantum numbers J^{PC} of the continuum state and the operator. This yields the number of form factors by simple comparison.

We start with identifying the quantum numbers of a state of two pions $|\pi\bar{\pi}\rangle$. This is done in a standard textbook manner, e.g. as for the positronium in [24]. Using a non-relativistic ansatz for the wavefunction of the bound state, we find the following quantum numbers J^{PC}:

$$|\pi\bar{\pi}\rangle \; : \quad 0^{++},\; 1^{--},\; 2^{++},\; 3^{--},\; \dots \; . \tag{2.18}$$

This is exactly as stated in [22]. The corresponding quantum numbers for the operators $\mathcal{O}$ are taken from [22] and [23]:

$$\begin{aligned} \bar{\psi}\, \gamma^{\{\mu} \mathrm{i}D^{\mu_1} \cdots \mathrm{i}D^{\mu_n\}}\, \psi \; &: \; j^{(-)^j\,(-)^{n+1}}, \\ \bar{\psi}\, \gamma_5 \gamma^{\{\mu} \mathrm{i}D^{\mu_1} \cdots \mathrm{i}D^{\mu_n\}}\, \psi \; &: \; j^{(-)^{j+1}\,(-)^{n}}, \\ \bar{\psi}\, \mathrm{i}\sigma^{[\mu\{\nu]} \mathrm{i}D^{\mu_1} \cdots \mathrm{i}D^{\mu_n\}}\, \psi \; &: \; j^{(-)^{j+1}\,(-)^{n+1}} \text{ and } j^{(-)^{j}\,(-)^{n+1}}, \end{aligned} \tag{2.19}$$

where we have $j = 0, 1, \dots, n+1$ for the vector and axial-vector operators and in case of the tensor operators $j = 1, \dots, n+1$.

With Equations (2.18) and (2.19) we can identify the number of generalised form factors to be:

$$\begin{aligned} \text{vector operator:} \quad & \lceil \tfrac{n}{2} \rceil + 1, \\ \text{axial vector operator:} \quad & 0, \\ \text{tensor operator:} \quad & \lfloor \tfrac{n}{2} \rfloor + 1. \end{aligned} \tag{2.20}$$

Here n corresponds again to the number of derivative terms in the operator and $\lceil\,\rceil$, $\lfloor\,\rfloor$ represent the next largest or smallest integer value, respectively. Note that the matching of the quantum numbers show that there are no axial vector GFFs, thus the corresponding GPDs vanish.

2.6.2 Decomposition into Generalised Form Factors

The general form of this decomposition is given by Lorentz structure of the matrix element. We abbreviate the matrix elements with $\mathcal{M}$, $\mathcal{M}_5$, and $\mathcal{M}_\sigma$ for the vector, axial vector and

tensor operator, respectively:

$$\mathcal{M}^{\{\mu\mu_1\mu_2\ldots\mu_n\}}(P,\Delta) = \left\langle \pi(p') \right| \bar{\psi}(0)\, \gamma^{\{\mu}\, \mathrm{i}\overleftrightarrow{D}^{\mu_1} \mathrm{i}\overleftrightarrow{D}^{\mu_2} \ldots \mathrm{i}\overleftrightarrow{D}^{\mu_n\}}\, \psi(0) \left| \pi(p) \right\rangle , \tag{2.21a}$$

$$\mathcal{M}_5^{\{\mu\mu_1\mu_2\ldots\mu_n\}}(P,\Delta) = \left\langle \pi(p') \right| \bar{\psi}(0)\, \gamma_5\gamma^{\{\mu}\, \mathrm{i}\overleftrightarrow{D}^{\mu_1} \mathrm{i}\overleftrightarrow{D}^{\mu_2} \ldots \mathrm{i}\overleftrightarrow{D}^{\mu_n\}}\, \psi(0) \left| \pi(p) \right\rangle , \tag{2.21b}$$

$$\mathcal{M}_{\mathrm{T}}^{[\mu\{\nu]\mu_1\mu_2\ldots\mu_n\}}(P,\Delta) = \left\langle \pi(p') \right| \bar{\psi}(0)\, \mathrm{i}\sigma^{[\mu\{\nu]}\, \mathrm{i}\overleftrightarrow{D}^{\mu_1} \mathrm{i}\overleftrightarrow{D}^{\mu_2} \ldots \mathrm{i}\overleftrightarrow{D}^{\mu_n\}}\, \psi(0) \left| \pi(p) \right\rangle . \tag{2.21c}$$

Without any additional knowledge the decomposition of the matrix elements (2.21a)-(2.21c) only has to obey the Lorentz structure given by $\mathcal{M}$, $\mathcal{M}_5$, and $\mathcal{M}_\sigma$. This means we can have any combination of the momenta P and Δ having the same Lorentz symmetry. To obtain additional constraints on the possible number of generalised form factors, we use the transformations under parity $\mathcal{P}$ and time-reversal $\mathcal{T}$.

Applying both transformations to all the matrix elements we end up with the following general relations providing constraints due to the stated symmetry:

$$\mathcal{M}^{\{\mu\mu_1\mu_2\ldots\mu_n\}}(P,\Delta) \xrightarrow{\mathcal{T}} \quad \mathcal{M}^{\{\mu\mu_n\ldots\mu_2\mu_1\}}(P,-\Delta)\,, \tag{2.22a}$$

$$\mathcal{M}_5^{\{\mu\mu_1\mu_2\ldots\mu_n\}}(P,\Delta) \xrightarrow{\mathcal{P}} -\mathcal{M}_5^{\{\mu\mu_1\mu_2\ldots\mu_2\}}(P,\Delta)\,, \tag{2.22b}$$

$$\mathcal{M}_{\mathrm{T}}^{[\mu\{\nu]\mu_1\mu_2\ldots\mu_n\}}(P,\Delta) \xrightarrow{\mathcal{T}} -\mathcal{M}_{\mathrm{T}}^{[\mu\{\nu]\mu_n\ldots\mu_2\mu_1\}}(P,-\Delta)\,. \tag{2.22c}$$

From (2.22b) we immediately see that for any given number n of derivatives $\overleftrightarrow{D}$ the matrix elements $\mathcal{M}_5$ vanish. This matches the counting in Section 2.6.1, Eq. (2.20). Relations (2.22a) and (2.22c) on the other hand show that we expect an odd, respectively even number of momenta Δ within the decomposition into generalised form factors. Further conditions that have to be kept in mind are that in general we want the form factors to be real and dimensionless. It is also of interest to have a straightforward matching to the already known electromagnetic form factor of the pion,

$$\left\langle \pi(\boldsymbol{p}') \right| V^\mu \left| \pi(\boldsymbol{p}) \right\rangle = 2P^\mu F(Q^2)\,, \tag{1.7}$$

and suggestive correspondence to the generalised form factors of the nucleon [16, 23, 25, 26]. The decomposition of the pion matrix elements into generalised form factors can then be written as

$$\begin{aligned}\mathcal{M}^{\{\mu\mu_1\mu_2\ldots\mu_n\}}(P,\Delta) = {} & 2P^{\{\mu}P^{\mu_1}\ldots P^{\mu_n\}}A_{n+1,0}(\Delta^2) \\ & + 2\sum_{\substack{i=1\\ \text{odd}}}^{n} \Delta^{\{\mu}\Delta^{\mu_1}\ldots\Delta^{\mu_i}P^{\mu_{i+1}}\ldots P^{\mu_n\}}\, A_{n+1,i+1}(\Delta^2),\end{aligned} \tag{2.23a}$$

$$\mathcal{M}_{\mathrm{T}}^{[\mu\{\nu]\mu_1\mu_2\ldots\mu_n\}}(P,\Delta) = \frac{1}{m_\pi}\sum_{\substack{i=0\\ \text{even}}}^{n} P^{[\mu}\Delta^{\{\nu]}\,\Delta^{\mu_1}\ldots\Delta^{\mu_i}P^{\mu_{i+1}}\ldots P^{\mu_n\}}\, B_{\mathrm{T}\,n+1,i}(\Delta^2). \tag{2.23b}$$

We again see that the matrix elements $\mathcal{M}_5$ vanish due to parity conservation. We can also read off that in the forward limit $\Delta \to 0$ only the GFFs $A_{n+1,0}$ will be accessible experimentally since the other kinematic pre-factors of decompositions tend to zero. Thus the remaining form factors can only be extracted from the actual limiting procedures.

2.7 Mellin Moments and Generalised Form Factors

In Section 2.3 we integrated $H^q_\pi(x,\xi,t)$ over the momentum fraction x and obtained the pion form factor (2.7). This is the lowest possible Mellin transformation, as introduced in Section 2.5. Similar relations hold for higher moments in x and the GFFs.

In order to calculate the moments $M_{n+1}(H^q_\pi)$ (analogous for $M_{n+1}(E^q_{\mathrm{T}\,\pi})$) we start by inserting Eqs. (2.16) and (2.17a) into the definition of the GPD

$$2P^+ \int \mathrm{d}x\, x^n H^q_\pi(x,\xi,t) = \frac{1}{(P^+)^n} \mathcal{M}^{\{\mu\mu_1\mu_2\ldots\mu_n\}}(P,\Delta) \tag{2.24}$$

where we have also used $\mathcal{M}^{\{\mu\mu_1\mu_2\ldots\mu_n\}}(P,\Delta)$ from (2.21a). Remembering that the twist-2 operators and hence their matrix elements involve + tensor components, and bearing in mind the definition for the skewness $\Delta^+ = -2\xi P^+$ we find

$$\int \mathrm{d}x\, x^n H^q_\pi(x,\xi,t) = A_{n+1,0}(\Delta^2) + \sum_{\substack{i=1\\ \text{odd}}}^{n} (-2\xi)^{i+1}\, A_{n+1,i+1}(\Delta^2)\,, \tag{2.25a}$$

and for the tensor GPD

$$\int \mathrm{d}x\, x^n E^q_{\mathrm{T}\,\pi}(x,\xi,t) = \sum_{\substack{i=0\\ \text{even}}}^{n} (-2\xi)^{i}\, B_{\mathrm{T}\,n+1,i}(\Delta^2)\,. \tag{2.25b}$$

We can again read off the correspondence of F^q_π and $A^q_{1,0}$ from Eq. (2.25a) as claimed (and demanded) earlier.

The forward limit of these two relations is again easier: since $\xi = 0$ only the vector GPD H^q_π has non-vanishing Mellin moments and we readily obtain

$$\int \mathrm{d}x\, x^n H^q_\pi(x,0,-\boldsymbol{\Delta}^2_\perp) = A_{n+1,0}(\Delta^2) \tag{2.26}$$

which, as demanded, is the pion form factor for $n = 0$ with $A_{1,0} = F_\pi$.

3 QCD on the Lattice

This chapter is devoted to an introduction to the discretised, Euclidean version of QCD first discussed by Wilson [27]: *Lattice QCD*. This is our method of choice to test the theory of the strong force and evaluate certain properties of hadrons.

As mentioned in the preface, lattice QCD is a non-perturbative approach and requires no model assumptions. Thus all calculations are from first principles. Apart from simulation specific parameters (like the lattice volume or specialities of the simulation algorithm) there are no additional parameters to the field theory in comparison to its continuum formulation. Like the Lagrangian of QCD, the lattice simulation has parameters to determine the quark masses and the coupling constant. These parameters can be – and have to be – tuned to eventually extrapolate to the physical theory. While this freedom can be an advantage if one wants to study what our world would look like at different quark masses, the unphysical regime of current simulations poses problems when comparing to physical observables. Lattice QCD also suffers from limitations concerning the volume and discretisation effects. However, if the simulation spans a large enough parameter space, one can attempt to perform all necessary limits. We will come back to this when we discuss our results.

Here we focus on the basics of the lattice approach and mention the techniques that are important for this work. We start with the continuum QCD Lagrangian and continue with the lattice formulation of the path integral including correlation functions. This naturally leads to a connection to Monte Carlo methods. We then explain the action used in our simulation. For an exhaustive introduction to lattice field theory, see [28].

3.1 The QCD Lagrangian

The starting point of every quantum field theory is its Lagrangian[1] from which the equations of motion and thus the dynamics of the theory can be derived. We provide the continuum formulation in this section. Since the matter fields of QCD are fermions, the *free* theory is described by the Dirac equation. The corresponding fermionic Lagrangian is[2]

$$\mathscr{L}_{\mathrm{F}}(x) = \bar{\psi}^{(f)}(x)\left(\mathrm{i}\gamma^{\mu}\partial_{\mu} - m^{(f)}\right)\psi^{(f)}(x)\,, \tag{3.1}$$

with x a space-time four-vector and where we have used a matrix notation to suppress Dirac and colour indices (α, c) for the fermion fields $\psi^{(f)}_{\alpha,c}$. Each of the n_f quarks with flavour f is of mass $m^{(f)}$. The γ^{μ} are 4×4 Dirac matrices with the Greek index running over space-time, defined by the anti-commutation relation

$$\left\{\gamma^{\mu}, \gamma^{\nu}\right\} = 2g^{\mu\nu}. \tag{3.2}$$

[1] We adopt the usual, somewhat sloppy language that does not distinguish between Lagrangian density and the Lagrangian.

[2] With Einstein's summing convention for repeated indices.

Because QCD is a locally gauge-invariant theory, the kinetic term is changed to include the covariant derivative

$$\partial_\mu \longrightarrow D_\mu(x) = \partial_\mu - \mathrm{i}gA^c_\mu(x)\, t_c \tag{3.3}$$

with g the coupling constant, A^c_μ the gauge fields and t^c the generators of the algebra su(3). The covariant derivative introduces interactions between the quark and gauge fields and is the first part of the transition to an interacting theory. The still missing part of the QCD Lagrangian describes the dynamics and interaction of the gauge fields themselves, its given by

$$\mathscr{L}_\mathrm{G}(x) = -\frac{1}{4} F^c_{\mu\nu}(x) F^{\mu\nu}_c(x)\,. \tag{3.4}$$

The self-interaction of the gluons emerges from the non-Abelian nature of QCD, which is hidden in the field strength tensor

$$F^c_{\mu\nu}(x) = \partial_\mu A^c_\nu(x) - \partial_\nu A^c_\mu(x) + g\, f^{cde} A^d_\mu(x), A^e_\nu(x)\,, \tag{3.5}$$

where f^{cde} are the structure constants of the group SU(3), encoding the commutation relations of the generators t^c. In standard form, these are written as

$$[t^d, t^e] = \mathrm{i} f^{cde} t^c. \tag{3.6}$$

Notice that the last term in Eq. (3.5) is absent in QED and causes cubic and quartic terms in the gauge fields. The final QCD Lagrangian is the sum of the fermionic and the gauge part, $\mathscr{L}_\mathrm{QCD} = \mathscr{L}_\mathrm{F} + \mathscr{L}_\mathrm{G}$.

3.2 Path Integral and Correlation Functions

Feynman's path integral formulation (or functional integral) can be used to quantise a theory. It is an indispensable tool for quantum field theories because it uses the Lagrangian as its fundamental quantity. Hence the path integral approach preserves all symmetries of a theory and can be applied to any interacting theory from scalar field theories to non-Abelian gauge theories. Since it can also be used to evaluate expectation values, it is very useful to investigate the dynamics of QCD. However, the path integral is only formally defined for continuum variables, by using a limiting process from a functional integral defined on a *discretised* space-time as shown in textbooks, e.g. [1, 2, 28]. This already suggests to use this more rigorous version of the path integral for computer simulations requiring non-continuous formulations and, more important, with a finite number of degrees of freedom.

The very first step on the way to numerical simulations is to simply stick to the definition of the path integral on a set of space-time points:

$$x = a(n_1, n_2, n_3, n_4) \text{ with } n_j \in \{1, 2, 3, \ldots N_j\}\,, \tag{3.7}$$

where we include a lattice spacing a and restrict ourselves to a hypercube with N_j points in the space-time direction j. We use $j = 1, 2, 3$ for spatial and $j = 4$ for the time direction. The fermion fields will now live on the lattice sites x and the gauge fields $A^c_\mu(x)$ will be replaced by parallel transporters $U_\mu(x)$. The latter are located on the links between the lattice sites and hence still are directed quantities like the vector gauge fields. They are

equivalent to path ordered exponentials of the gauge field (this is the discretised version of the Wilson line in (2.6)), given by

$$U_\mu(x) = e^{\mathrm{i}agA^c_\mu(x)t^c}\,, \tag{3.8}$$

With $\Lambda(x)$ as element of the $SU(3)$ gauge group, they transform like

$$U_\mu(x) \quad \to \quad \Lambda(x)U_\mu(x)\Lambda^{-1}(x+a\hat{\mu})\,. \tag{3.9}$$

Here $\hat{\mu}$ is the unit vector in direction μ. The path integral is then given by

$$\int [\mathrm{d}\bar{\psi}][\mathrm{d}\psi][\mathrm{d}U]\, e^{\mathrm{i}S[\bar{\psi},\psi,U]}\,, \tag{3.10}$$

where the integral is over all values of these fields at all space-time points. Formally, the integration measure can be written as

$$[\mathrm{d}\bar{\psi}][\mathrm{d}\psi][\mathrm{d}U] = \prod_{x,c,f,\alpha} \mathrm{d}\bar{\psi}^f_{c,\alpha}(x)\,\mathrm{d}\psi(x)^f_{c,\alpha} \prod_{x,\mu} \mathrm{d}U_\mu(x)\,, \tag{3.11}$$

here explicitly including all indices. The action S in (3.10) is the 'integrated' Lagrangian density on our space-time points x

$$S[\bar{\psi},\psi,U] = a^4 \sum_x \mathscr{L}_{\mathrm{QCD}}[\bar{\psi}^f_{c,\alpha}(x), \psi^f_{c,\alpha}(x), U_\mu(x)]\,. \tag{3.12}$$

We leave the discussion of the explicit form of the action until later in this chapter.

It is worth noting that the lattice approach quite naturally provides a regularisation scheme. This is in contrast to perturbative (continuum) quantum field theories, where one has to use, e.g. Pauli-Villars or dimensional regularisation to render the expressions finite. In discretised space-time, the lattice constant a corresponds to a maximum energy providing an ultraviolet cut-off. Furthermore, since space-time is limited to a finite 'box' of four-volume $V_\mathrm{s}\times T$ we also obtain the necessary infrared cut-off. As with any regularisation scheme, this in turn breaks some symmetries of the theory: the discretisation breaks Lorentz symmetry down to the hypercubic group $H(4)$ and translational invariance only holds for multiples of the lattice spacing a. These symmetries are however restored in the continuum limit, $a \to 0$.

The second step towards a numerical solution is noting that the phase factor including the action in (3.10) has a complex argument. The weights for the different paths in the functional integral are thus oscillating, which would leave the path integral inappropriate for simulations. The solution is a Wick rotation of the time variable to imaginary times $t \to -\mathrm{i}\tau$ ($\tau > 0$). This leads to a Euclidean formulation of QCD with a changed weight factor

$$\{\gamma_\mu, \gamma_\nu\} \to \{\gamma^\mathrm{E}_\mu, \gamma^\mathrm{E}_\nu\} = 2\delta_{\mu\nu}\,, \qquad e^{\mathrm{i}S} \to e^{-S^\mathrm{E}}\,. \tag{3.13}$$

We will drop the superscript 'E' for Euclidean in the remainder and stick to Euclidean space. Instead we will note the use of objects in Minkowski (or Euclidean) space explicitly where necessary. Note that the Euclidean indices run from 1, ..., 4 where the last index is used for the time component.

The vacuum expectation value of an operator $\mathcal{O}$ can now be calculated by

$$\left\langle \mathcal{O}(\bar{\psi},\psi,U)\right\rangle = \frac{1}{Z}\int [\mathrm{d}\bar{\psi}][\mathrm{d}\psi][\mathrm{d}U]\, O(\bar{\psi},\psi,U)\, e^{-S[\bar{\psi},\psi,U]}\,. \tag{3.14}$$

It is important to note that the *operator* on the l.h.s. appears as a *function* of the fermion and gauge fields $(\bar{\psi},\psi,U)$ on the r.h.s. of this equation. The partition function

$$Z = \int [\mathrm{d}\bar{\psi}][\mathrm{d}\psi][\mathrm{d}U]\, e^{-S[\bar{\psi},\psi,U]} \tag{3.15}$$

makes sure that unwanted phase-factors drop out.

We will only be interested in operators of (anti-)quark fields in this work. These will create or annihilate quarks and describe the currents that couple to them. While the time-ordering of these operators is easily observed, the non-commuting nature of the fermion fields has to be taken care of. The use of Grassmann valued fields is a necessity. We also still need a prescription to tell what the function $O(\bar{\psi},\psi,U)$ will look like for a specific correlation function on the l.h.s. of Eq. (3.14). This is achieved by using the generating functional and Wick contractions.

The generating functional is defined as

$$W[\eta,\bar{\eta}] = \int [\mathrm{d}\bar{\psi}][\mathrm{d}\psi][\mathrm{d}U]\, e^{-S[\bar{\psi},\psi,U]}\, e^{\bar{\eta}\psi}\, e^{\bar{\psi}\eta}, \tag{3.16}$$

$$\text{and thus } Z = W_0 = W[\eta,\bar{\eta}]\Big|_{\eta,\bar{\eta}=0}\,.$$

Here additional source terms $\bar{\eta}\psi$ $(\bar{\psi}\eta)$ for the (anti-)quark fields have been introduced. Functional derivatives with respect to the currents $\eta,\bar{\eta}$ connect to the correlation functions. For n quarks and anti-quarks in the correlation function we have

$$\left\langle \psi_{i_1}\bar{\psi}_{i_2}\ldots\psi_{i_{n-1}}\bar{\psi}_{i_n}\right\rangle = \frac{1}{W_0}\frac{\delta}{\delta\bar{\eta}_{i_1}}\frac{-\delta}{\delta\eta_{i_2}}\cdots\frac{\delta}{\delta\bar{\eta}_{i_{n-1}}}\frac{-\delta}{\delta\eta_{i_n}}W[\eta,\bar{\eta}]\Big|_{\eta,\eta'=0}\,. \tag{3.17}$$

Note that this is for a fixed combination of Dirac and colour indices, collectively denoted by an index i. In addition, Eq. (3.17) is also for the given ordering of the quark fields. What we need for calculations in QCD are quark propagators between an initial and a final point in space-time. Even more, we need all possible combinations of these quark lines. This includes closed loops and interchanges of quarks obeying the anti-commuting nature of fermions. The quark propagator (or Green's function) is

$$\mathcal{D}^{-1}_{i,j}(x,x') = \left\langle \psi_i(x)\bar{\psi}_j(x')\right\rangle = \frac{1}{W_0}\frac{\delta}{\delta\bar{\eta}_i}\frac{-\delta}{\delta\eta_j}W[\eta,\bar{\eta}]\Big|_{\eta,\eta'=0}\,. \tag{3.18}$$

The propagator is the inverse of the Dirac operator $\mathcal{D}$, formally given by

$$S_\mathrm{F}[\bar{\psi},\psi,U] = a^4\sum_{i,j,x,x'}\bar{\psi}_i(x)\mathcal{D}_{i,j}(x,x')\psi_j(x')\,, \tag{3.19}$$

with S_F the fermionic part of the QCD action. After completing the square in the fermion fields and a change of variables, the fermionic part of the generating functional can be written as a Gaussian integral. Integrating out the fermion fields one arrives at

$$W[\eta,\bar{\eta}] = \int [\mathrm{d}U]\ \det\mathcal{D}\, e^{-S_\mathrm{G}[U]} e^{\bar{\eta}_i(x)\mathcal{D}^{-1}_{i,j}(x,x')\eta_j(x')}\,. \tag{3.20}$$

The fermion determinant $\det \mathcal{D}$ here contains all so-called sea quark contributions. The action appearing in this integral is now reduced to the contribution of the gauge fields only. Functional derivatives with respect to currents $\eta, \bar{\eta}$ will bring down factors containing the quark propagator. The possible combinations of quark lines are then found by Wick's theorem. It is given by

$$\begin{aligned}\left\langle \psi_{i_1}\bar{\psi}_{j_1}\psi_{i_2}\bar{\psi}_{j_2}\cdots\psi_{i_n}\bar{\psi}_{j_n}\right\rangle \\ = \frac{(-1)^n}{W_0}\sum_{\substack{\text{permutations } p\\ \text{of } 1,2,\ldots,n}} \operatorname{sign}(p)\int [\mathrm{d}U]\,\det\mathcal{D}\,\mathcal{D}^{-1}_{i_1 j_{p_1}}\mathcal{D}^{-1}_{i_2 j_{p_2}}\cdots\mathcal{D}^{-1}_{i_n j_{p_n}} e^{\mathrm{i}S_\mathrm{G}[U]}\,. \end{aligned} \tag{3.21}$$

The permutations make sure we pick up all combinations of quark fields while the sign pre-factor preserves the Pauli principle for the interchange of fermions. We will make use of this procedure when calculating n-point functions later in this chapter.

3.3 Monte Carlo

The similarity of our field theoretic partition function Z, Eq. (3.15), with statistical mechanics led to similar numerical approaches. Our goal of computing the high dimensional path integral in Eq. (3.14) can be done via the *Monte Carlo* technique. Hereby the path integral is replaced by an average over an ensemble of N gauge configurations U_n

$$\langle \mathcal{O}(U)\rangle_\mathrm{G} = \frac{1}{N}\sum_{n=1}^{N}\mathcal{O}(U_n)\,, \tag{3.22}$$

where a single gauge configuration consists of link variables between all lattice sites. Taking the limit $N\to\infty$ the exact average and hence the path integral is recovered

$$\langle \mathcal{O}(U)\rangle_\mathrm{G} \overset{N\to\infty}{\longrightarrow} \langle \mathcal{O}(U)\rangle = \frac{1}{Z}\int [\mathrm{d}U]\det\mathcal{D}\,O(U)e^{-S[U]}\,. \tag{3.23}$$

Estimates of the uncertainty of the Monte Carlo process play an important role. We will use two standard procedures to determine the errors: namely Jackknife or bootstrap errors. The gauge configurations are generated according to their statistical (Boltzmann) weight

$$p(U_n) = \frac{1}{Z}e^{-S[U_n]}\,, \qquad Z = \sum_n e^{-S[U_n]}\,, \tag{3.24}$$

by simulating a *Markov chain*, in this specific case known as *importance sampling*. This process requires strong ergodicity, i.e. every configuration of gauge links can be reached from any other configuration: $P(U'\leftarrow U) > 0$ where P is the transition probability. In order to reach and maintain equilibrium and generate the desired distribution of configurations, the *detailed balance* condition

$$P(U'\leftarrow U)p(U) = P(U\leftarrow U')p(U') \tag{3.25}$$

has to be fulfilled.

There are a variety of updating processes leading from one configuration to a new one, corresponding to different possibilities of the transition probability. For quenched

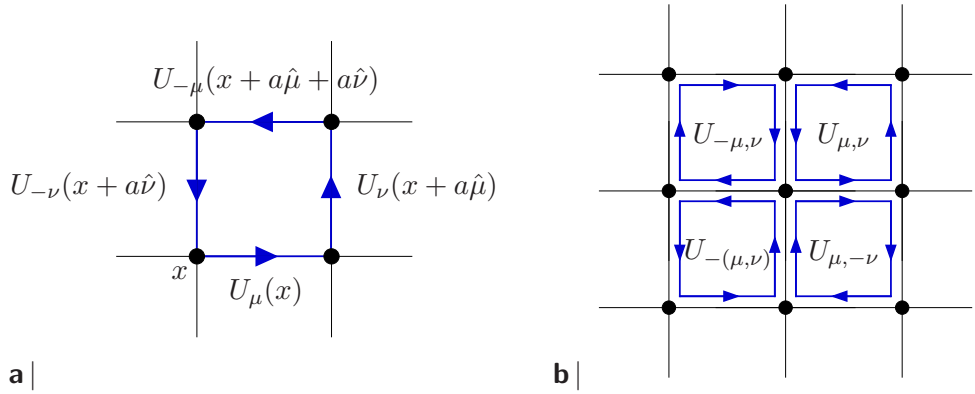

a | **b** |

Figure 3.1 | **a** | The plaquette term $U_{\mu,\nu}(x)$ of the Wilson gauge action, Eq. (3.26). **b** | The clover-leaf of the discretised field strength tensor, Eq. (3.40)

simulations where the fermion determinant is set to a constant, common choices are the Metropolis or Heatbath algorithms. Our dynamical simulation on the other hand includes the fermion determinant which requires additional computational effort. The determinant is included in a purely bosonic effective action and simulated via pseudofermions. This can for example be done by using the Hybrid Monte Carlo algorithm [29]. The Metropolis acceptance is here combined with an updating process based on the evolution of the fields under the Hamiltonian of the system.

3.4 Wilson Glue

The gauge action we used in our simulation was introduced by Wilson [27]. It is known as the *plaquette* action for reason that will become clear within the next lines.

A necessary requirement is that the proper continuum behaviour is recovered. We already noted the transformation properties of the link variables U_μ in Eq. (3.9). Constructing closed loops with these link variables is then easily seen to be invariant under gauge transformations. The simplest of such closed curves is the plaquette shown in Fig. 3.1.a and given by

$$U_{\mu,\nu}(x) = U_\mu(x)U_\nu(x + a\hat{\mu})U_{-\mu}(x + a\hat{\nu} + a\hat{\mu})U_{-\nu}(x + a\hat{\nu}). \tag{3.26}$$

where $\hat{\mu}$ is a unit vector in μ-direction. The Wilson plaquette action for $SU(3)$ then is

$$S_{\mathrm{G}}[U] = \sum_{\mathrm{p}} \frac{\beta}{3} \mathrm{Re}\left[\mathrm{Tr}(1 - U_{\mu,\nu}(x))\right], \tag{3.27}$$

which is real and positive. The summation in (3.27) is over all possible 1×1 plaquettes, the trace is over the colour indices. The constant term in the action is physically insignificant and only included to exactly match the continuum expression in the limit $a \to 0$. To show that this is in fact the case, one has to expand (3.8) for small a and insert it into the trace. Using the Campbell-Baker-Hausdorff relation[3] and the lattice approximation for the derivative of the gauge fields,

$$a \cdot \partial_\mu A^c_\nu(x) = A^c_\nu(x + a\hat{\mu}) - A^c_\nu(x) + \mathcal{O}(a^2)\,, \tag{3.28}$$

[3]The Campbell-Baker-Hausdorff relation reads $e^x e^y = e^{x+y+(1/2)[x,y]+\ldots}$

the Wilson action (3.27) in the continuum limit $a \to 0$ becomes

$$\begin{aligned} S_{\mathrm{G}} &= \frac{\beta}{4 \cdot 3} \sum_x a^4 \operatorname{Tr}\left[F_{\mu\nu}(x) F_{\mu\nu}(x) + \mathcal{O}(a^2)\right] \\ &= \frac{\beta}{8 \cdot 3} \sum_x a^4 \left[F^c_{\mu\nu}(x) F^c_{\mu\nu}(x) + \mathcal{O}(a^2)\right]. \end{aligned} \tag{3.29}$$

Comparing this to the gauge action in (3.4) yields a relation between β and the coupling constant for the continuum:

$$\beta = \frac{6}{g^2}. \tag{3.30}$$

From Eq. (3.29) we can read off that our lattice gauge action has $\mathcal{O}(a^2)$ discretisation effects.

3.5 Lattice Fermion Action

Having introduced the lattice gauge action, we are still missing a lattice version for the fermionic part of the action. We now turn to the discussion of the fermion action used in our work.

Naïve Fermions

With the derivative discretised as the finite difference between neighbouring lattice sites

$$\partial_\mu \psi(x) = \frac{1}{2a}[\psi(x + a\hat{\mu}) - \psi(x - a\hat{\mu})] \tag{3.31}$$

we arrive at a naïve discretisation of the fermion action and Dirac matrix

$$S_{\mathrm{F}}[\bar{\psi}, \psi, U] = \sum_{i,j,x,x'} \bar{\psi}_i(x) \mathcal{D}_{i,j}(x, x') \psi_j(x') \tag{3.19}$$

$$\mathcal{D}_{i,j}(x, x') = m_{i,j} \delta_{x,x'} + \frac{1}{2} \sum_\mu (\gamma_\mu)_{i,j} \, \delta_{x'+a\hat{\mu},x} \, U_\mu(x). \tag{3.32}$$

for which we have re-scaled to dimensionless variables $\psi \to a^{-3/2}\psi$ and $m \to a^{-1}m$ and used the convention

$$\sum_\mu = \sum_{\mu=\pm 1}^{\pm 4}, \quad \gamma_{-\mu} = -\gamma_\mu, \quad \text{and} \quad U_{-\mu}(x) = U_\mu(x - a\hat{\mu})^\dagger. \tag{3.33}$$

The link variables U_μ in (3.32) are included to keep gauge invariance. Although this ansatz has good scaling properties with $\mathcal{O}(a^2)$ discretisation errors, it suffers from the so-called *fermion doubling*. To see this, consider the propagator of free quarks in momentum space

$$\mathcal{D}^{-1}(p_\mu) = \frac{-\mathrm{i}\gamma_\mu \sin(p_\mu) + m}{\sum_\mu \sin^2(p_\mu) + m^2} \tag{3.34}$$

for lattice momenta given by

$$p_i = 2\pi \frac{n_i}{N}, \quad \text{with } n_i = 0, 1, 2, \ldots N_i - 1, i = 1, 2, 3 \quad \text{and } p_4 = \mathrm{i}E \tag{3.35}$$

when E is the particle's energy. The lattice momenta have a discretised spectrum because of the periodic boundary conditions we apply to our lattice. The poles of the propagator (3.34) then define the particles of the free theory. Since the sine function has zeros not only for $p_\mu = 0$ but also at the corners of the Brillouin zone, we find 16 particles for $\mu = 1, \ldots, 4$. The extra 15 fermions are unphysical lattice artifacts that do not vanish in the continuum limit ($a \to 0$).

Wilson Fermions

Since the main constraint on the discretisation is that the right continuum limit is recovered, there is quite some ambiguity in the actual form of the lattice action. Additional operators of higher dimension can be introduced, as long as they vanish for $a \to 0$. It was again Wilson who used this freedom, adding an extra term to the fermion action [30] leading to

$$\mathcal{D}_{i,j}(x, x') = \frac{1}{2\kappa}\delta_{x,x'} + \frac{1}{2}\sum_\mu [r - (\gamma_\mu)_{i,j}]\, \delta_{x'+a\hat{\mu},x}\, U_\mu(x)\,, \tag{3.36}$$

with the *hopping parameter*[4]

$$\kappa = \frac{1}{8r + 2m}\,. \tag{3.37}$$

The parameter r is in the interval $[0, 1]$. For $r = 0$ the naïve discretisation is recovered. Other values for r decouple the unphysical fermions from the theory by giving them a mass proportional to $1/a$. This can again be checked for the free theory and its quark propagator.

However, as usual 'there's no free lunch'. Following Nielsen-Ninomiya's no-go theorem we have to trade exact chiral symmetry against the removal of doublers for a local operator with the correct continuum limit. In fact, the Wilson term we just added in (3.36) explicitly breaks chiral symmetry. The no-go theorem can only be circumvented using the Ginsparg-Wilson relation [31], or, more precisely, a fermion action based on it. In this relation, the exact chiral symmetry used in the no-go theorem is replaced with a lattice version, so that chiral symmetry is recovered for $a \to 0$. Since the re-discovery of this equation, a number of fermion formulations appeared: there are approximate solutions to the Ginsparg-Wilson relation in form of the fixed-point [32] or the chirally improved operator [33]. Other possibilities are the domain wall approach [34] or Neuberger's overlap operator [35]. The former introduces an additional, fifth dimension, removing the doublers and separating left- and right-handed fermions. Here the Ginsparg-Wilson relation holds for the extent of this extra dimension going to infinity. The latter fermion operator is explicitly constructed to satisfy the Ginsparg-Wilson relation. While providing the cleanest description of lattice fermions, it is computationally the most demanding one.

Apart from breaking chiral symmetry, the hopping parameter also affects the bare quark mass of the theory. In the chiral limit $m_\mathrm{q} \to 0$ of a free theory we can set a *critical hopping parameter* $\kappa_c^\mathrm{free} = 1/8r$. In the full theory with interacting fermions, it has to be determined within the simulation, i.e. κ_c corresponds to vanishing quark mass as obtained

[4] We will adopt the usual convention of rescaling the fermions fields by $\sqrt{2\kappa}$ to remove the hopping parameter from the action.

from e.g. vanishing pion mass. For the quark masses one then has

$$am_{\mathrm{q}} \propto \left(\frac{1}{\kappa} - \frac{1}{\kappa_c}\right) . \tag{3.38}$$

Improved Wilson Fermions

There is another draw-back of the Wilson fermion action: discretisation errors now start at $\mathcal{O}(a)$ in contrast to our gauge action (and we prefer a consistent behaviour). A technique generally referred to as *improvement* can be used to remedy these scaling violations. It is once again based on the fact that a lattice action has to reproduce the continuum formulation for $a \to 0$ but can otherwise contain higher-dimensional and thus irrelevant operators, their number only limited by the symmetries of the original action. Those additional terms can then be tuned to improve the continuum limit.

Including the Wilson term, five such terms have been identified by Sheikholeslami and Wohlert [36]. If we restrict ourselves to on-shell quantities, the equations of motion can be used to further reduce the possible operators. The only new contribution to the Wilson action then is the so-called *clover term*:

$$c_{\mathrm{SW}} \frac{\mathrm{i}}{4} a g^2 \bar{\psi}(x)\, \sigma_{\mu\nu} F_{\mu\nu}(x)\, \psi(x) \,, \tag{3.39}$$

with an improvement constant c_{SW} and a discretised field strength tensor $F_{\mu\nu}$. The latter can be written as

$$F_{\mu\nu}(x) = \frac{1}{8\mathrm{i}g} \sum_{\mu,\nu} [U_{\mu\nu}(x) - U_{\mu\nu}(x)^\dagger] \,. \tag{3.40}$$

The field strength tensor is calculated using sums of neighbouring plaquettes (3.26), as pictured in Fig. 3.1.b thus motivating the name clover action. The improved Dirac operator then looks like

$$\mathcal{D}_{i,j}(x,x') = \frac{1}{2\kappa}\delta_{x,x'} \left[1 + c_{\mathrm{SW}} \frac{\mathrm{i}}{2} a\kappa g^2\, \sigma_{\mu\nu} F_{\mu\nu}(x)\right] + \frac{1}{2} \sum_{\mu} [r - (\gamma_\mu)_{i,j}]\, \delta_{x'+a\hat{\mu},x}\, U_\mu(x). \tag{3.41}$$

If we now arrange for one lattice (physical) observable to have no $\mathcal{O}(a)$ terms by tuning c_{SW} we can fix our improvement coefficient. This will depend on the specific lattice (i.e. its coupling constant β) but, together with our $\mathcal{O}(a^2)$ lattice gauge action, ensures that other observables can be improved as well (the lattice version of the operators (2.17a)/(2.17b) require additional attention here).

The value for c_{SW} has been obtained non-perturbatively by the Alpha collaboration

$$c_{\mathrm{SW}} = \frac{1 - 0.454g^2 - 0.175g^4 + 0.012g^6 + 0.045g^8}{1 - 0.720g^2} \,, \tag{3.42}$$

in terms of the bare gauge coupling g, [37]. We use this as input for our simulation.

4 Matrix Elements from the Lattice

We now turn to the discussion of lattice techniques for calculating matrix elements on the lattice. In general, these are n-point functions of fermionic operators that can be evaluated using the Wick contractions discussed in the previous chapter.

Our starting point will be the well known pion two-point function which is connected to the pion energy. We derive its lattice and the continuum representation and mention a possibility to increase the quality of the signal. This is followed by a discussion of the Euclidean operators that we use to evaluate the moments of GPDs. The necessary three-point functions can exhibit so-called fermion disconnected lines as we will show. A separate section explains the sequential source technique, simplifying the lattice calculation of three-point functions. Finally, a closer look is taken at the extraction of the operator matrix elements from the lattice data. A ratio of three- and two-point functions is specially suited for that and we note differences to the better known nucleon case.

4.1 Two-Point Functions

We start with pion two-point functions and their representation on the lattice and in continuum. Two-point functions can be seen to create a particle with certain momentum $\boldsymbol{p}$ at a given time t' and annihilate it again at a later time t (so we have $t > t'$). Conventionally they are written as

$$\Big\langle \mathcal{O}(\boldsymbol{p},t)\mathcal{O}^\dagger(\boldsymbol{p},t')\Big\rangle = \big\langle\Omega\big|\, \mathcal{O}(\boldsymbol{p},t)\mathcal{O}^\dagger(\boldsymbol{p},t')\,\big|\Omega\big\rangle\,, \tag{4.1}$$

and we can extract properties like the particle's energy from their time behaviour. The creation and annihilation operators are also referred to as *interpolating fields* or *interpolating currents*. Ideally, these create the wave function of the particle and are required to have non-vanishing overlap with the particle state

$$\big\langle\Omega\big|\, \mathcal{O}(\boldsymbol{p},t)\,\big|\text{particle}(\boldsymbol{p},t)\big\rangle \neq 0 \quad \text{and} \quad \big\langle\text{particle}(\boldsymbol{p},t)\big|\, \mathcal{O}^\dagger(\boldsymbol{p},t)\,\big|\Omega\big\rangle \neq 0\,. \tag{4.2}$$

Hence they must have the same quantum numbers (spin, flavour, parity) as the particle. The most general (in terms of flavour and Dirac structure) meson interpolating field are quark bilinears given by

$$\eta(\boldsymbol{p},t) = \frac{1}{\sqrt{V_\mathrm{s}}}\sum_{\boldsymbol{x}} e^{-\mathrm{i}\boldsymbol{p}\boldsymbol{x}}\, F_{f,f'}\, \bar\psi^{(f)}_{\alpha,c}(x)\,\Gamma_{\alpha,\alpha'}\,\psi^{(f')}_{\alpha',c}(x) \quad \text{and} \tag{4.3a}$$

$$\eta^\dagger(\boldsymbol{p},t) = \frac{1}{\sqrt{V_\mathrm{s}}}\sum_{\boldsymbol{x}} e^{\mathrm{i}\boldsymbol{p}\boldsymbol{x}}\, F'_{f,f'}\, \bar\psi^{(f)}_{\alpha,c}(x)\,\Gamma'_{\alpha,\alpha'}\,\psi^{(f')}_{\alpha',c}(x)\,, \tag{4.3b}$$

where we have included flavour matrices F, F' and sum over Dirac, flavour, and colour indices. The latter ensures that we have a colour singlet state. The Fourier transform over

all spatial lattice points projects on the momentum $\boldsymbol{p}$ and is the source of the (spatial) volume factor. Finally, the matrices Γ, Γ' are responsible for the correct J^{PC} quantum numbers of the meson.

Restricting ourselves to the pion, we only need flavours u and d. In addition, since we do not change the structure of the particle between source and sink, we have $\Gamma' = \gamma_4\Gamma^\dagger\gamma_4$. Inserting (4.3a) and (4.3b) in (4.1) and using Wick contractions of Sec. 3.2 we then find as correlation function for the π^+ (however neglecting the '+')

$$\begin{aligned} C_{\mathrm{2pt}}(t,t',\boldsymbol{p}) &= \left\langle \eta_\pi(\boldsymbol{p},t)\, \eta_\pi^\dagger(\boldsymbol{p},t') \right\rangle \\ &= \frac{1}{V_\mathrm{s}} \sum_{\boldsymbol{x},\boldsymbol{x}'} e^{-\mathrm{i}\boldsymbol{p}(\boldsymbol{x}-\boldsymbol{x}')} \left\langle \bar\psi^{(d)}_{\alpha,c}(x)\, \Gamma_{\alpha,\alpha'}\, \psi^{(u)}_{\alpha',c}(x) \bar\psi^{(u)}_{\beta,c'}(x')\, \Gamma'_{\beta,\beta'}\, \psi^{(d)}_{\beta',c'}(x') \right\rangle_\mathrm{G} \\ &= -\frac{1}{V_\mathrm{s}} \sum_{\boldsymbol{x},\boldsymbol{x}'} e^{-\mathrm{i}\boldsymbol{p}(\boldsymbol{x}-\boldsymbol{x}')} \left\langle \mathrm{Tr}\left[\mathcal{D}_u^{-1}(x,x')\gamma_4\Gamma^\dagger\gamma_4 \mathcal{D}_d^{-1}(x',x)\Gamma \right] \right\rangle_\mathrm{G} . \end{aligned} \tag{4.4}$$

Here the trace is over Dirac and colour space and $x_4 = t$, $x'_4 = t'$ and we average over all gauge configurations. Note that in the general case, where we can also have flavour diagonal correlators, a second, disconnected contribution appears. We can further simplify this equation by using translational invariance and γ_5-hermiticity of the propagator, $\mathcal{D}(x',x) = \gamma_5\mathcal{D}^\dagger(x,x')\gamma_5$.

$$C_{\mathrm{2pt}}(t,t',\boldsymbol{p}) = -\sum_{\boldsymbol{x}} e^{-\mathrm{i}\boldsymbol{p}\boldsymbol{x}} \left\langle \mathrm{Tr}\left[\mathcal{D}_u^{-1}(\boldsymbol{x},t,\boldsymbol{0},t')\, \gamma_4\Gamma^\dagger\gamma_4\gamma_5 \left(\mathcal{D}_d^{-1}(\boldsymbol{x},t,\boldsymbol{0},t')\right)^\dagger \gamma_5\Gamma \right] \right\rangle_\mathrm{G} , \tag{4.5}$$

with the transpose in Dirac and colour indices. For the lattice simulation, we now only need to invert propagators from $(\boldsymbol{x},t')$ to all other lattice points and not also the other way round, thus saving computer time.

To be able to extract the energy from the correlation function (4.1) we need the transfer matrix formalism and we have to look at its Hilbert space representation. The time evolution of an operator is obtained from $e^{-t\mathcal{H}}$ with the Hamiltonian $\mathcal{H}$ of the theory. Since we have periodic boundary conditions, time evolution of (4.1) results in

$$\left\langle \eta_\pi(\boldsymbol{p},t)\eta_\pi^\dagger(\boldsymbol{p},t') \right\rangle = \left\langle \eta_\pi(\boldsymbol{p},0)\, e^{-(t-t')\mathcal{H}} \eta_\pi^\dagger(\boldsymbol{p},0)\, e^{-(T-(t-t'))\mathcal{H}} \right\rangle , \tag{4.6}$$

when T is the time extent of our lattice. This correlation function corresponds to taking the trace over a complete set of eigenstates. Choosing energy eigenstates $\left|0\right\rangle, \left|1\right\rangle, \left|2\right\rangle, \ldots$ to the Hamiltonian with energies $E_0 \le E_1 \le E_2 \le \ldots$, we obtain

$$\begin{aligned} \sum_i \left\langle i\right| \eta\, e^{-(t-t')\mathcal{H}}\, \eta^\dagger\, e^{-(T-(t-t'))\mathcal{H}} \left|i\right\rangle &= \sum_{i,j} \left\langle i\right| \eta\, e^{-(t-t')\mathcal{H}} \left|j\right\rangle \left\langle j\right| \eta^\dagger\, e^{-(T-(t-t'))\mathcal{H}} \left|i\right\rangle \\ &= \sum_{i,j} e^{-(t-t')E_j}\, e^{-(T-(t-t'))E_i} \left\langle i\right| \eta \left|j\right\rangle \left\langle j\right| \eta^\dagger \left|i\right\rangle , \end{aligned} \tag{4.7}$$

where we have neglected the arguments of the interpolating fields. For large time separations $t' \ll t \ll T$ we find that states with higher energies are exponentially suppressed and the state with lowest energy that has overlap with our interpolators dominates the

sum. Denoting the vacuum with $\big|0\big\rangle$ and the lowest state in energy with $E_\pi(\boldsymbol{p})$ we thus arrive at

$$\begin{aligned}\Big\langle \eta_\pi(\boldsymbol{p},t)\eta_\pi^\dagger(\boldsymbol{p},t')\Big\rangle = {} & e^{-(t-t')E_\pi(\boldsymbol{p})}\left\langle 0\right|\eta_\pi(\boldsymbol{p})\left|\pi(\boldsymbol{p})\right\rangle\left\langle\pi(\boldsymbol{p})\right|\eta_\pi^\dagger(\boldsymbol{p})\left|0\right\rangle \\ & + e^{-(T-(t-t'))E_\pi(\boldsymbol{p})}\left\langle\pi(\boldsymbol{p})\right|\eta_\pi^\dagger(\boldsymbol{p})\left|0\right\rangle\left\langle 0\right|\eta_\pi(\boldsymbol{p})\left|\pi(\boldsymbol{p})\right\rangle + \dots\end{aligned} \tag{4.8}$$

The two contributions in this equation correspond to a pion travelling forward in time from the source at t' to the sink at t, and an anti-pion travelling on the other side of the torus (our lattice) and backward in time (the exponential hence relative to T). The ellipsis refers to the suppressed excited states. Reducing the expression even more we can write

$$\Big\langle \eta_\pi(\boldsymbol{p},t)\eta_\pi^\dagger(\boldsymbol{p},t')\Big\rangle = e^{-E_\pi(\boldsymbol{p})T/2}\left|\left\langle 0\right|\eta_\pi(\boldsymbol{p})\left|\pi(\boldsymbol{p})\right\rangle\right|^2 2\cosh\left[\left(T/2-\left(t-t'\right)\right)E_\pi(\boldsymbol{p})\right]+\dots \tag{4.9}$$

4.1.1 Increasing the Overlap – Smearing of Quark Fields

We stated at the beginning of the section, that the interpolating fields ideally create the wave function of the mesons. However, hadrons are not point-like objects like the quark fields we construct them with. To really include the wave function, we would need interpolators like

$$\eta(\boldsymbol{p},t) = \frac{1}{\sqrt{V_\mathrm{s}}}\sum_{\boldsymbol{x}_1,\boldsymbol{x}_2} e^{-\mathrm{i}\boldsymbol{p}(\boldsymbol{x}_1+\boldsymbol{x}_2)/2}\, F_{f,f'}\,\varphi(x_1,x_2)\,\bar{\psi}^{(f)}_{\alpha,c}(x_1)\,\Gamma_{\alpha,\alpha'}\,\psi^{(f')}_{\alpha',c}(x_2)\,, \tag{4.10}$$

where $\varphi(x_1,x_2)$ now describes the spatial part of the meson wave function.[1] While there is the possibility to displace the quark fields relative to each other (e.g. for baryons see [38]) the more common approach is to use smearing. Using this method, the overlap with physical states is increased by spatially extending the quark fields on the lattice. This is similar to Gaussian blurring in image processing, where one uses a convolution with a Gaussian shape to blur the picture.

We use gauge covariant Jacobi smearing of the quark fields in a plane at $x_4 = t$ [39, 40, 41]

$${}^S\psi(\boldsymbol{x},t) = \sum_{\boldsymbol{y}} {}^S H(\boldsymbol{x},\boldsymbol{y},U,t)\,{}^P\psi(\boldsymbol{y},t), \tag{4.11}$$

where H is the smearing kernel and S is the smearing label (S for smeared or P for point-like). H is diagonal in colour and chosen to be gauge covariant and Hermitian

$${}^S H^\dagger = {}^S H. \tag{4.12}$$

The smeared anti-quark fields are defined as

$${}^S\bar{\psi}(\boldsymbol{x},t) = \sum_{\boldsymbol{y}} {}^P\bar{\psi}(\boldsymbol{y},t)\,{}^S H(\boldsymbol{y},\boldsymbol{x},U,t). \tag{4.13}$$

Our smeared propagator then reads

$${}^{S'S}\mathcal{D}^{-1}(\boldsymbol{y},t,\boldsymbol{x},0) = \sum_{\boldsymbol{x}',\boldsymbol{y}'} {}^{S'}H(\boldsymbol{y},\boldsymbol{y}',U,t)\,\mathcal{D}^{-1}(\boldsymbol{y}',t,\boldsymbol{x}',0)\,{}^S H(\boldsymbol{x}',\boldsymbol{x},U,0). \tag{4.14}$$

[1] Using a δ-function we recover the interpolator in (4.3a).

Note that we can have different smearing for source and sink fields, thus $S' = P$ is possible. One can also use different smearing for quarks inside the pion, giving them a different spatial extent thus having the possibility to mimic nodes in the wave function. However, this would especially be used to determine excited meson states (see e.g. [42]), while we are only interested in the pion ground state where one type of smearing is enough to increase the overlap.

The practical implementation of the smearing is done by applying a truncated Jacobi iterative solution to the Klein-Gordon equation [39]. The kernel ${}^{S}H$ then reads

$$\begin{aligned} {}^{S}H(\boldsymbol{x},\boldsymbol{y},U,t) &= \sum_{j=0}^{N_{\text{smear}}} \kappa^j \big(K(\boldsymbol{x},\boldsymbol{y},t)\big)^j, \\ K(\boldsymbol{x},\boldsymbol{y},t) &= \sum_{\mu=1}^{3} \left[U_\mu(\boldsymbol{x},t)\delta_{\boldsymbol{x}+\mu,\boldsymbol{y}} + U_{-\mu}(\boldsymbol{x},t)\delta_{\boldsymbol{x}-\mu,\boldsymbol{y}}\right]. \end{aligned} \tag{4.15}$$

N_{smear} is the number of iterations and, being increased, increases the size of the smeared object. The second parameter in (4.15), κ, controls the coarseness of the iteration. Both parameters are used to tune the average radius r of the smeared quark fields and depend on the lattice constant a. We define the radius r as

$$r^2 = \frac{\sum_{\boldsymbol{x}} (\boldsymbol{x}-\boldsymbol{y})^2 \, |{}^{S}H(\boldsymbol{x},\boldsymbol{y},U,t)|^2}{|{}^{S}H(\boldsymbol{x},\boldsymbol{y},U,t)|^2}. \tag{4.16}$$

We try to have radii of the order of 0.35 fm which has been found to be a good compromise when aiming for a nucleon charge radius of ~ 0.8 fm. The smearing parameters used in our simulation are given in the appendix.

4.2 Lattice Operators

Since we want to calculate moments of GPDs on the lattice, we need to implement the towers of local operators on the lattice. We introduced the continuum operators in Sec. 2.5 and their relation to moments of the distribution functions in Sec. 2.7. Without worrying about (anti-) symmetrisation and subtraction of traces for the moment, we define the Euclidean counterparts of the operators on the lattice as

$$\mathcal{O}^{\text{E}}_{\mu\mu_1\mu_2\ldots\mu_n} = F_{ff'}\,\bar{\psi}^{(f)}\gamma_\mu \overleftrightarrow{D}_{\mu_1}\overleftrightarrow{D}_{\mu_2}\ldots\overleftrightarrow{D}_{\mu_n}\psi^{(f)}, \tag{4.17a}$$

$$\mathcal{O}^{\text{E,T}}_{\mu\nu\mu_1\mu_2\ldots\mu_n} = F_{ff'}\,\bar{\psi}^{(f)}\sigma_{\mu\nu} \overleftrightarrow{D}_{\mu_1}\overleftrightarrow{D}_{\mu_2}\ldots\overleftrightarrow{D}_{\mu_n}\psi^{(f)}. \tag{4.17b}$$

This makes use of a flavour matrix F to determine the quark flavours of the operator. The lattice covariant derivative is given by

$$\begin{aligned} \vec{D}_\mu\psi(x) &= \frac{1}{2a}\left[U_\mu(x)\psi(x+a\mu) - U_{-\mu}(x)\psi(x-a\mu)\right], \\ \bar{\psi}(x)\overleftarrow{D}_\mu &= \frac{1}{2a}\left[\bar{\psi}(x+a\mu)U_\mu(x) - \bar{\psi}(x-a\mu)U_{-\mu}(x)\right]. \end{aligned} \tag{4.18}$$

Comparing the Euclidean $(1,1,1,1)$ and the Minkowski metric $(1,-1,-1,-1)$, and bearing in mind that we Wick rotated the time component, we can write down matching coefficients between the lattice and the continuum operators. For the covariant derivative we find

$$\mathrm{i}D^0 = -D^{\text{E}}_4\,, \qquad \mathrm{i}D^j = -\mathrm{i}D^{\text{E}}_j\,, \quad \text{with } j = 1,2,3 \tag{4.19}$$

and similarly for the γ-matrices

$$\gamma^0 = \gamma_4^{\mathrm{E}}\,, \qquad \gamma^j = \mathrm{i}\gamma_j^{\mathrm{E}} \quad \text{and for completeness} \quad \gamma_5 = -\gamma_5^{\mathrm{E}}\,. \tag{4.20}$$

This leads to the correspondence of the operators

$$\mathcal{O}^{\mu\mu_1\mu_2\ldots\mu_n} = (-1)^{n_4+n_5+1}(-\mathrm{i})^{n_{123}}\mathcal{O}^{\mathrm{E}}_{\mu\mu_1\mu_2\ldots\mu_n} \tag{4.21a}$$

$$\mathcal{O}^{\mu\nu\mu_1\mu_2\ldots\mu_n}_{\mathrm{T}} = (-1)^{n_4+n_5+1}(-\mathrm{i})^{n_{123}+1}\mathcal{O}^{\mathrm{E,T}}_{\mu\nu\mu_1\mu_2\ldots\mu_n} \tag{4.21b}$$

Up to now we have ignored the fact that we need properly (anti-) symmetrised and traceless operators. This is necessary for leading twist operators as found in Sec. 2.5. The operators were classified due to their transformation properties under Lorentz transformation and charge conjugation. On the lattice, Lorentz symmetry is replaced by symmetry under the hypercubic group $H(4)$ and our lattice operators have to transform irreducibly under $H(4)$. The operators are then constructed to be symmetrised and traceless. We list all operators in App. B and give here an example for combinations of the vector operator with one derivative only that we used (no derivatives is the trivial case)

$$\frac{1}{2}(\mathcal{O}_{11}+\mathcal{O}_{22}-\mathcal{O}_{33}-\mathcal{O}_{44})\,, \quad \frac{1}{\sqrt{2}}(\mathcal{O}_{33}-\mathcal{O}_{44})\,, \quad \frac{1}{\sqrt{2}}(\mathcal{O}_{11}-\mathcal{O}_{22}) \tag{4.22}$$

and

$$\frac{1}{\sqrt{2}}(\mathcal{O}_{\mu\nu}+\mathcal{O}_{\nu\mu})\,, \quad 1 \le \mu \le \nu \le 4\,. \tag{4.23}$$

Note that the operators in Eq. (4.22) and (4.23) belong to different irreducible representations of $H(4)$. So we can expect different lattice artifacts. Nevertheless they have the same continuum limit.

Because the hypercubic group is only a finite group compared to the (continuum) orthogonal group $O(4)$, the restrictions due to this group are less and mixing between the various operators can occur [43, 44]. However, mixing is only an issue for two or more derivatives. Furthermore, it has been found that for the operators we use, mixing should be small and can be neglected. This was found numerically and can be explained by the fact that the renormalised mixing operators vanish in the continuum [44].

The improvement scheme that we applied to the fermion action to obtain a $\mathcal{O}(a)$ improved QCD action, can also be applied to our lattice operators, Eq. (4.17a). In fact, this would be a requirement to calculate matrix elements with $\mathcal{O}(a^2)$ errors of these operators, since improving the action alone would only suffice for the calculation of hadron masses. A general $\mathcal{O}(a)$ improved operator can be written as

$$\mathcal{O}^{\mathrm{imp}} = (1 + am_{\mathrm{q}}b_{\mathcal{O}})\mathcal{O} + \sum_{i=1}^{N} ac_i\mathcal{O}_i\,. \tag{4.24}$$

Here, the first factor includes an improvement term connected to the quark mass and we encounter new improvement coefficients $b_{\mathcal{O}}$, c_i that depend on the coupling constant. Improved operators are furthermore only known for up to one derivative; the explicit form of these operators can be found from e.g. [45] and references therein. However, lacking non-perturbative values for the improvement coefficients we will in general neglect improving the operators because the available coefficients from perturbation theory are known to be unreliable [46, 47]. We will come back to this when we discuss our results and will try and explore the effect of improvement.

4.2.1 Renormalisation of Operators

As for continuum matrix elements, we need to worry about divergent contributions on the lattice as well. The fact that divergencies occur is most easily seen from perturbation theory, where momentum integrals have to be evaluated. As mentioned in the previous chapter, lattice regularisation effectively provides a momentum cut-off thus avoiding infinities. Upon removing the cut-off, i.e. taking the lattice spacing $a \to 0$ (cut-off to infinity), we need to renormalise our operators to obtain finite results for the physical quantities. For a renormalised operator in some scheme $\mathcal{S}$, we can write

$$\mathcal{O}^{\text{ren}}_{\mathcal{S},\mu} = Z^{\mathcal{S}}_{\mathcal{O}}(\mu,\beta)\,\mathcal{O}\,. \tag{4.25}$$

The renormalisation or scaling factor is called $Z^{\mathcal{S}}$ and dependent on the regularisation scheme $\mathcal{S}$ (of the physical matrix elements) and the renormalisation scale μ. It also depends on the coupling constant used in the gauge action.

This can be achieved by lattice perturbation theory [48] as well as non-perturbative calculations. For the latter different approaches exist. The ALPHA-Collaboration uses the Schrödinger functional method to calculate renormalisation constants (for a review see e.g. [49]). We on the other hand make use of a non-perturbative procedure [50] that is along the lines of the perturbation method defined by the MOM scheme and that was proposed by Martinelli et al. [51]. It works in a MOM-like scheme, the so-called RI′-MOM scheme. To give a short outline of this method, we start with the non-amputated quark Greens function with an operator $\mathcal{O}$ inserted with zero momentum

$$G_{\alpha,\alpha'}(\boldsymbol{p}) = \frac{1}{V}\sum_{\boldsymbol{x},\boldsymbol{y},z} e^{-\mathrm{i}\boldsymbol{p}(\boldsymbol{x}-\boldsymbol{y})}\left\langle \psi^{(f)}_{\alpha}(x)\,\mathcal{O}(z)\,\bar{\psi}^{(f)}_{\alpha'}(y)\right\rangle \tag{4.26}$$

and the quark propagator in momentum space, $\mathcal{D}^{-1}_{\alpha,\alpha'}(\boldsymbol{p})$, given by the Fourier transform of (3.18). The vertex or amputated Greens function is then obtained from

$$\Gamma(p) = \mathcal{D}(\boldsymbol{p})G(\boldsymbol{p})\mathcal{D}(\boldsymbol{p})\,. \tag{4.27}$$

With the renormalised vertex function $\Gamma^{\text{ren}} = Z_{\text{q}}^{-1} Z_{\mathcal{O}}^{\text{RI}'\text{-MOM}}\,\Gamma$ and a renormalisation condition imposed as

$$\frac{1}{12}\mathrm{Tr}\left(\Gamma^{\text{ren}}(\boldsymbol{p})\Gamma^{-1}_{\text{Born}}(\boldsymbol{p})\right) = 1 \tag{4.28}$$

we can fix the renormalisation constant $Z_{\mathcal{O}}^{\text{RI}'\text{-MOM}}$ at $p^2 = \mu^2$ where μ is the renormalisation scale. Since the trace is in Dirac and colour space, the factor $1/12$ ensures the correct overall normalisation. The Born term Γ_{Born} in the vertex function is also computed on the lattice. The last ingredient is Z_{q}, the quark field renormalisation constant. This can be obtained from the quark propagator directly,

$$Z_{\text{q}} = \left.\frac{\mathrm{Tr}(-\mathrm{i}\sum_\alpha \gamma_\alpha \sin(ap_\alpha) a\mathcal{D}(\boldsymbol{p}'))}{12\sum_\alpha \sin^2(ap_\alpha)}\right|_{p^2=\mu^2}. \tag{4.29}$$

The scale μ of the renormalisation constants has to satisfy $1/L^2 \ll \Lambda^2_{\text{QCD}} \ll mu^2 \ll 1/a^2$ where L is the extent of the lattice. This condition has to be checked in the calculation, e.g. by identifying a plateau value of Z with respect to the momentum.

A comparison with phenomenological values finally requires the scheme $\mathcal{S}$ to be one of the continuum renormalisation schemes, e.g. $\overline{\text{MS}}$. This, together with a possible change in scale, is achieved by an additional multiplicative factor

$$\mathcal{O}_{\mathcal{S}',\mu'} = Z_{\mathcal{O}}^{\mathcal{S}',\mathcal{S}}(\mu',\mu)\mathcal{O}_{\mathcal{S},\mu}\,, \tag{4.30}$$

which can be calculated perturbatively [50].

4.3 Three-Point Functions

Our goal is to calculate moments of pion GPDs. So the actual matrix elements we are interested in are three-point functions with an additional current between two pion states. Their general form is

$$\left\langle \pi(\boldsymbol{p}')\right| \mathcal{O} \left|\pi(\boldsymbol{p})\right\rangle_{\text{continuum}} \sim \left\langle \eta_\pi(\boldsymbol{p}',t)\, \mathcal{O}(\tau)\, \eta_\pi^\dagger(\boldsymbol{p},t')\right\rangle_{\text{lattice}}\,, \tag{4.31}$$

where we have the pion interpolators as before but now with possibly distinct momenta, and the local operators $\mathcal{O}(\tau)$ arising in the Mellin moments, Sec. 2.5. The operators are inserted at a time τ between pion source and sink at t' and t, respectively. They were discussed in the previous section and we now write them down in a general form as [41]

$$\mathcal{O}(\tau) = \sum_{x,z,z'} e^{\mathrm{i}\boldsymbol{q}\boldsymbol{x}} F_{f,f'}\, \bar{\psi}^{(f)}_{\alpha,c}(z) J^{c,c'}_{\alpha,\alpha'}(x,z,z') \psi^{(f')}_{\alpha',c'}(z')\,. \tag{4.32}$$

The current J represents the Dirac, flavour and derivative structure of the operators (it is diagonal in colour and we sum over colour indices c, c'). The coordinate where the interaction takes place is labelled x with $x_4 = \tau$, while z, z' indicate the discretised derivative. The Fourier transform imposes the momentum transfer caused by the current in form of the 3-momentum $\boldsymbol{q}$. We again make use of translational invariance and put the pion source at $\mathbf{0}$; we also fix $t' = 0$ for simplicity. Inserting the pion interpolators (for a π^+) and this general operator into (4.31) we then get

$$\begin{aligned}\left\langle \eta_\pi(\boldsymbol{p}',t)\, \mathcal{O}(\tau)\, \eta^\dagger\pi(\boldsymbol{p},t')\right\rangle &= \sum_{\boldsymbol{y}} \sum_{\boldsymbol{x},z,z'} e^{-\mathrm{i}\boldsymbol{p}'\boldsymbol{y}}\, e^{\mathrm{i}\boldsymbol{q}\boldsymbol{x}}\, F_{f,f'} \\ &\times \left\langle \bar{\psi}^{(d)}_{\alpha,a}(y)\, \Gamma_{\alpha,\alpha'}\, \psi^{(u)}_{\alpha',a}(y)\, \bar{\psi}^{(f)}_{\beta,b}(z) J^{b,b'}_{\beta,\beta'}(x,z,z') \psi^{(f')}_{\beta',b'}(z')\, \bar{\psi}^{(u)}_{\gamma,c}(0)\, \Gamma'_{\gamma,\gamma'}\, \psi^{(d)}_{\gamma',c}(0)\right\rangle_{\text{G}}\end{aligned} \tag{4.33}$$

with $y_4 = t$ and $x_4 = \tau$. Determining the Wick contractions we find that only diagonal elements of F can contribute and we arrive at

$$\begin{aligned}-\sum_{\boldsymbol{y}} \sum_{\boldsymbol{x},z,z'} e^{-\mathrm{i}\boldsymbol{p}'\boldsymbol{y}}\, e^{\mathrm{i}\boldsymbol{q}\boldsymbol{x}} \Big\langle & F_{11}\, \mathrm{Tr}\left[\mathcal{D}^{-1}(0,y)\, \Gamma\, \mathcal{D}^{-1}(y,z) J(x,z,z') \mathcal{D}^{-1}(z',0)\, \Gamma'\right] \\ & + F_{22}\, \mathrm{Tr}\left[\mathcal{D}^{-1}(z',y)\, \Gamma\, \mathcal{D}^{-1}(y,0)\, \Gamma'\, \mathcal{D}^{-1}(0,z) J(x,z,z')\right] \\ & - (F_{11}+F_{22})\, \mathrm{Tr}\left[\mathcal{D}^{-1}(0,y)\Gamma\mathcal{D}^{-1}(y,0)\Gamma'\right]\, \mathrm{Tr}\left[\mathcal{D}^{-1}(z',z) J(x,z,z')\right]\Big\rangle_{\text{G}}.\end{aligned} \tag{4.34}$$

The last contribution to the three-point function is a fermion-line disconnected graph, as depicted in Fig. 4.1. Since we sum over z, z' this would require all-to-all propagators

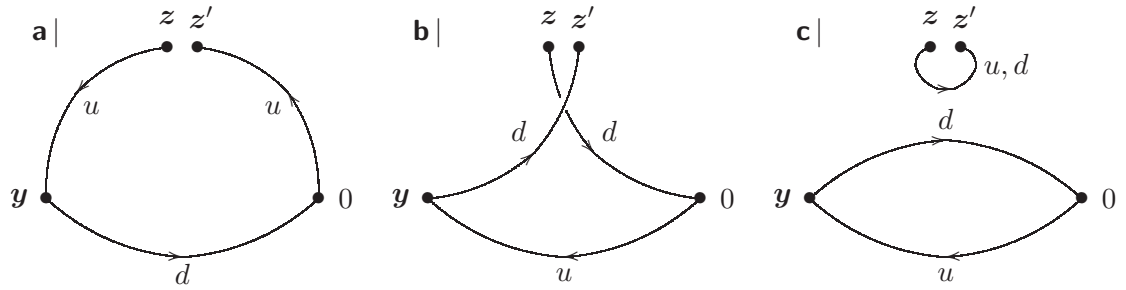

Figure 4.1 | Different contributions to the three-point function Eq. (4.34): **a** | and **b** | The two connected graphs where u and d flavours are probed. **c** | The disconnected contribution.

which is computationally prohibitive (inversions between z (z') and y will be discussed later, Sec. 4.3.1). Note that we could choose $F_{11} + F_{22} = 0$ to remove this part of the Wick contractions, however, before we comment on these disconnected contributions, let us first focus on the ...

Connected Contributions

The two fermion-line connected terms in (4.34) can be related using γ_5-hermiticity for the propagators and [41]

$$\gamma_5\Gamma\gamma_5 = s\Gamma^\dagger\,, \quad \gamma_5\Gamma'\gamma_5 = s'\Gamma'^\dagger\,, \quad \gamma_5 J(x,z,z')\gamma_5 = s_j J(x,z',z)^\dagger\,, \tag{4.35}$$

where J has to be symmetrised in its space-time indices and $s, s', s_j = \pm 1$. The connected part of the three-point function then is

$$-\sum_{\boldsymbol{y}}\sum_{\boldsymbol{x}} e^{-\mathrm{i}\boldsymbol{p}'\boldsymbol{y}}\, e^{\mathrm{i}\boldsymbol{q}\boldsymbol{x}}\,(F_{11}\,M(x,y) + ss's_j\,F_{22}\,M^*(x,y))\,, \tag{4.36}$$

with the abbreviation

$$M(x,y) = \sum_{z,z'}\Big\langle \mathrm{Tr}\left[\mathcal{D}^{-1}(0,y)\,\Gamma\,\mathcal{D}^{-1}(y,z)J(x,z,z')\mathcal{D}^{-1}(z',0)\,\Gamma'\right]\Big\rangle_{\mathrm{G}}\,. \tag{4.37}$$

Note that with $\Gamma' = \gamma_4\Gamma^\dagger\gamma_4$ we have $s = s'$ so we will drop their product. Still following [41] we now use the charge conjugation matrix, defined by

$$C\gamma_\mu C^{-1} = -\gamma_\mu^{\mathrm{T}}\,, \quad C\gamma_5 C^{-1} = \gamma_5^{\mathrm{T}} \tag{4.38}$$

and similar to the above introduce [41]

$$C\mathcal{D}^{-1}(x,y;U)C^{-1} = (\mathcal{D}^{-1})^{\mathrm{T}}(y,z;U^*)\,, \tag{4.39}$$

$$C\Gamma C^{-1} = c\Gamma^{\mathrm{T}}\,, \quad C\Gamma' C^{-1} = c'\Gamma'^{\mathrm{T}} \tag{4.40}$$

$$CJ(x,z,z';U)C^{-1} = c_j J^{\mathrm{T}}(x,z',z;U^*) \tag{4.41}$$

where we explicitly denoted the dependence on the gauge links and the transpose acts on Dirac and colour space. Like before we have $c, c', c_j = \pm 1$ and $c = c'$. With γ_5-hermiticity we then find

$$M^*(x,y) = c_j s_j\,M(x,y)\,. \tag{4.42}$$

Putting everything together, the connected contribution to the three-point function then is

$$-\sum_{\boldsymbol{x},\boldsymbol{y}} e^{-\mathrm{i}\boldsymbol{p}'y+\mathrm{i}\boldsymbol{q}x}\,(F_{11}+c_jF_{22})\,M(x,y)\,. \tag{4.43}$$

Note that $c_j = \pm 1$ imposes constraints on F_{11} and F_{22} in order to have a non-vanishing contribution (see below, Eq. (4.47)).

We now look at the Hilbert space decomposition of the three-point function Eq. (4.31). Here, the transfer matrix distinguishes two cases since we have to obey time ordering:

$$\begin{aligned} C_{3\mathrm{pt}}(t,\tau,\boldsymbol{p}',\boldsymbol{q}) &= \Big\langle \eta_\pi(\boldsymbol{p}',t)\,\mathcal{O}(\tau)\,\eta_\pi^\dagger(\boldsymbol{p},0)\Big\rangle \\ &= \begin{cases} \sum_i \big\langle i\big|\,\eta_\pi(\boldsymbol{p}',0)\,e^{-(t-\tau)\mathcal{H}}\mathcal{O}(0)\,e^{-\tau\mathcal{H}}\,\eta_\pi^\dagger(\boldsymbol{p},0)\,e^{-(T-t)\mathcal{H}}\,\big|i\big\rangle & \text{for } 0\le\tau\le t \\ \sum_i \big\langle i\big|\,\mathcal{O}(0)\,e^{-(\tau-t)\mathcal{H}}\,\eta_\pi(\boldsymbol{p}',0)\,e^{-t\mathcal{H}}\,\eta_\pi^\dagger(\boldsymbol{p},0)\,e^{-(T-\tau)\mathcal{H}}\,\big|i\big\rangle & \text{for } 0\le t\le\tau \end{cases}. \end{aligned} \tag{4.44}$$

Following the steps applied to the two-point functions, Eq. (4.44) can be written as

$$\begin{aligned} C_{3\mathrm{pt}}(t,\tau,\boldsymbol{p}',\boldsymbol{q}) &= \big\langle\pi(\boldsymbol{p}')\big|\,\mathcal{O}(0)\,\big|\pi(\boldsymbol{p})\big\rangle\,\big\langle 0\big|\,\eta_\pi(\boldsymbol{p}')\,\big|\pi(\boldsymbol{p}')\big\rangle\,\big\langle\pi(\boldsymbol{p})\big|\,\eta_\pi^\dagger(\boldsymbol{p})\,\big|0\big\rangle \\ &\quad\times\Big(e^{-(t-\tau)E_\pi(\boldsymbol{p}')-\tau E_\pi(\boldsymbol{p})}+(-1)^{n_4}\,e^{-(\tau-t)E_\pi(\boldsymbol{p}')-(T-\tau)E_\pi(\boldsymbol{p})}\Big)+\ldots\,, \end{aligned} \tag{4.45}$$

where n_4 counts the number of temporal components of the operator in the matrix element. This sign factor stems from the different time-ordering which makes charge conjugation and time-reversal of the matrix element necessary. In our simulation we can however pick one contribution by restricting our signal to either of the two possible time-orderings. For a large enough separation of τ from the sink, the signal from the opposite side can be neglected as it is exponentially suppressed. So for $0\le\tau\le t$ we neglect the signal of the backward propagating pion that would correspond to the time ordering $0\le t\le\tau$ (and vice versa). The ellipsis in Eq. (4.45) refers to contributions from excited states. These are suppressed for $t-\tau\gg 1/(E'_\pi-E_\pi)$ and $\tau\gg 1/(E'_\pi-E_\pi)$ where E_π (E'_π) is the ground (excited) state energy.

Disconnected Contributions

We now return to the disconnected contributions to the three-point function, i.e. the last line in Eq. (4.34)

$$G^{\mathrm{disc}}(U) = -(F_{11}+F_{22})\,\mathrm{Tr}\left[\mathcal{D}^{-1}(0,y)\,\Gamma\,\mathcal{D}^{-1}(y,0)\,\Gamma'\right]\mathrm{Tr}\left[\mathcal{D}^{-1}(z',z)J(x,z,z')\right]\,. \tag{4.46}$$

Here we closely follow an argument given in [52]. It is based on the behaviour of the propagator, our Dirac structure of the pion interpolators, and the operator used in the trace when applying the charge conjugation matrix C. We already used this at the beginning of this section, Eqs. (4.39)–(4.41). Concerning the Dirac structure Γ, Γ' we found $c=c'$. The sign of c_j is found to be

$$c_j = (-1)^{n+1}\,, \tag{4.47}$$

where n is the number of derivatives of the operator. One factor here originates from the charge conjugation matrix acting on the γ_μ (or $\sigma_{\mu\nu}$) and one minus per derivative. Although the charge conjugation matrix does not act on the lattice covariant derivative

directly, using complex conjugated gauge links causes an interchange of the spatial coordinates (also the transpose in Dirac space) and introduces a minus sign.[2]

From Eq. (4.43) we now see that the flavour matrix F must not be traceless for an *odd* number of derivatives. For an *even* number of derivatives we can consider traceless isovector combinations of the current. In this case, Eq. (4.46) would vanish identically, hence preventing disconnected contributions already on the level of Wick contractions. This does, however, not suffice for the electromagnetic vector current, where we need $F_{11} = 2/3$ and $F_{22} = -1/3$. Picking up the argument of [52] again, we find for the disconnected part of the three-point function

$$G^{\text{disc}}(U) = -G^{\text{disc}}(U^*)\,, \tag{4.48}$$

after the application of Eqs. (4.39)–(4.41) to Eq. (4.46). Since the gauge action (3.27) is invariant under $U \to U^*$ these configurations have equal weight. We can thus write

$$\left\langle G^{\text{disc}}(U) \right\rangle_{\text{G}} = \frac{1}{2} \left\langle G^{\text{disc}}(U) + G^{\text{disc}}(U^*) \right\rangle_{\text{G}} \tag{4.49}$$

and thus find that the disconnected graphs vanish when averaged over all ensembles

$$\left\langle G^{\text{disc}}(U) \right\rangle_{\text{G}} = 0\,, \qquad \text{for } \textit{even } n\,. \tag{4.50}$$

Matrix elements with an even number of derivatives thus have no disconnected contributions. Matrix elements with an odd number of derivatives suffer from contributions by fermion-line disconnected graphs. We will neglect these due to the computational expense.

4.3.1 Sequential Source Technique

We just showed that some of the disconnected contributions to the three-point function drop out in the ensemble average. Furthermore, we neglect the remaining disconnected parts because it is computationally too demanding to calculate the necessary all-to-all propagators. However, a similar (connected) quark propagator still appears in the fermion contractions that we put on the lattice. Equation (4.37) contains $\mathcal{D}^{-1}(y,z)$ which would also require inversions from all lattice points to all other lattice points since we sum over y and z. This can be simplified using the sequential source technique (see [52, 53] and references therein). It is based on the fact that the necessary inversions to find the quark propagator by solving $\mathcal{D}v = b$ can be performed not only on a point-like (delta-function) source b, but on any linear combination of quark propagators $\mathcal{D}^{-1}$ as source. With this technique, any n-point function can be calculated by a sequence of at most $n-1$ inversions. The intermediate sources have to be fixed linear combinations of space-time, Dirac and colour indices.

The three-point function we want to calculate is

$$\sum_{\boldsymbol{x},z,z'} e^{+\mathrm{i}\boldsymbol{q}\boldsymbol{x}}\, \mathrm{Tr}\left[\sigma^{\mathrm{T}}(z) J(x,z,z')\, \mathcal{D}^{-1}(z',0)\Gamma'\gamma_5\right], \tag{4.51}$$

$$\text{with } \sigma^{\mathrm{T}}(z) = \sum_{\boldsymbol{y}} e^{-\mathrm{i}\boldsymbol{p}'\boldsymbol{y}}\, (\mathcal{D}^{-1})^{\dagger}(y,0)\, \gamma_5 \Gamma\, \mathcal{D}^{-1}(y,z)\,. \tag{4.52}$$

[2] The operators need to be symmetrised appropriately.

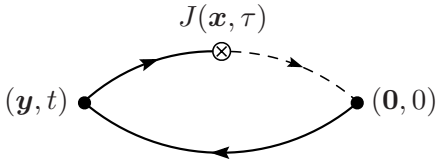

Figure 4.2 | This diagram shows an example of the propagator obtained by the sequential source technique as a solid line. Combined with the operator insertion ($\otimes$) and a standard quark propagator (dotted line) we then obtain the three-point function.

Multiplying the second line from the right with the Dirac matrix $\mathcal{D}(z,x')$ and summing over z leads to

$$\begin{aligned}\sum_z \sigma^{\mathrm{T}}(z)\mathcal{D}(z,x') &= \sum_{z,\boldsymbol{y}} e^{-\mathrm{i}\boldsymbol{p}'\boldsymbol{y}}\ (\mathcal{D}^{-1})^\dagger(y,0)\,\gamma_5\Gamma\,\mathcal{D}^{-1}(y,z)\mathcal{D}(z,x') \\ &= e^{-\mathrm{i}\boldsymbol{p}'\boldsymbol{x}'}\ (\mathcal{D}^{-1})^\dagger(x',0)\,\gamma_5\Gamma\,. \end{aligned} \tag{4.53}$$

Then, taking the Hermitian conjugate and using γ_5-hermiticity of the Dirac matrix, we find suitable source for a second inversion

$$\sum_z M(x',z)\,\gamma_5\,\sigma^*(z) = e^{\mathrm{i}\boldsymbol{p}'\boldsymbol{x}'}\ \gamma_5\Gamma^\dagger\gamma_5\ \mathcal{D}^{-1}(x',0) \tag{4.54}$$

We can thus solve for $\gamma_5\,\sigma^*(z)$ by performing a sequential inversion with a source b given by the r.h.s. of Eq. (4.54). The quark propagator contained in the source is hereby Fourier transformed and acts as a momentum source, hence requiring only one subsequent inversion to obtain the three-point function. The sequential propagator is depicted in Fig. 4.2.

Note that this second inversion has to be repeated every time the quantum numbers on our sink position $(\boldsymbol{y},t)$ (or the very sink itself) change, i.e. for different momenta $\boldsymbol{p}'$. Even though this is a slight disadvantage because we need to vary the momenta, we do benefit because we have not fixed the operator. So we have more freedom in choosing a rather large set of operators and transferred momenta $\boldsymbol{q}$, both suiting our study. This can be contrasted with another possible sequential source,'going through the operator' instead of the sink. This choice would then fix the operator, its Dirac and colour structure, and its momentum but on the other hand leave the quantum numbers of the sink free to choose.

4.4 Extracting Moments of GPDs – Building Ratios

We have just explained the three-point functions and how we are going to include them in our simulation. What we have neglected up to now is the different normalisation of the pion states on the lattice and in the continuum,

$$\begin{aligned}\big\langle\pi(\boldsymbol{p})|\pi(\boldsymbol{p}')\big\rangle_{\mathrm{lat}} &= \delta_{\boldsymbol{p},\boldsymbol{p}'}\,, \\ \big\langle\pi(\boldsymbol{p})|\pi(\boldsymbol{p}')\big\rangle_{\mathrm{cont}} &= 2E_\pi(\boldsymbol{p})(2\pi)^3\delta(\boldsymbol{p}-\boldsymbol{p}')\,. \end{aligned} \tag{4.55}$$

The effect is that we have to multiply the two- and three-point functions with an additional, relativistic factor for physical matrix elements:

$$C_{\mathrm{2pt}}(t,t',\boldsymbol{p}) \to \frac{C_{\mathrm{2pt}}(t,t',\boldsymbol{p})}{2E_\pi(\boldsymbol{p})}\,, \tag{4.56}$$

$$C_{\mathrm{3pt}}(t,\tau,\boldsymbol{p}',\boldsymbol{p}) \to \frac{C_{\mathrm{3pt}}(t,\tau,\boldsymbol{p}',\boldsymbol{p})}{4E_\pi(\boldsymbol{p})E_\pi(\boldsymbol{p}')}\,. \tag{4.57}$$

From the formulation in Hilbert space, Eq. (4.45), we read off the time behaviour and the overlap factors of the pion interpolators and the pion states. Of course we can now try and fit the exponential decay to the three-point function, in addition extracting the overlap from the pion two-point correlators, Eq. (4.9) and finally isolate the matrix element $\langle\pi(\boldsymbol{p}')|\,\mathcal{O}\,|\pi(\boldsymbol{p})\rangle$. Yet it has proved to be more reliable to build ratios of the lattice three- and two-point functions to eliminate as many of these factors as possible. Using the raw lattice data one can hope that fluctuations between the different configurations cancel each other, enhancing the signal. Since on the one hand we aim for a large set of momentum transfers $\boldsymbol{q}$ for our off-forward matrix elements while on the other hand we want to limit the number of sink momenta $\boldsymbol{p}'$ (these would require an additional second inversion each), we will in general have $|\boldsymbol{p}| \neq |\boldsymbol{p}'|$. We thus adopt a ratio that was already used in a similar investigation for nucleons as initial and final hadronic states [54]. This ratio has the form

$$R(\tau) = \frac{C_{\mathrm{3pt}}(\tau,\boldsymbol{p}',\boldsymbol{p})}{C_{\mathrm{2pt}}(t,\boldsymbol{p}')}\,\left[\frac{C_{\mathrm{2pt}}(t-\tau,\boldsymbol{p})\,C_{\mathrm{2pt}}(\tau,\boldsymbol{p}')\,C_{\mathrm{2pt}}(t,\boldsymbol{p}')}{C_{\mathrm{2pt}}(t-\tau,\boldsymbol{p}')\,C_{\mathrm{2pt}}(\tau,\boldsymbol{p})\,C_{\mathrm{2pt}}(t,\boldsymbol{p})}\right]^{\frac{1}{2}}\,. \tag{4.58}$$

In the case where $|\boldsymbol{p}| = |\boldsymbol{p}'|$ the square root can be dropped and the ratio (4.58) simplifies to the commonly used ratio with just one two-point function. For the ratio we have put the source at 0 and dropped the corresponding argument t' from the two-point functions. The operator insertion remains at τ and the time slice of the sink is labelled t. Furthermore, we will in the remainder fix the sink position of the two- and three-point functions at $t = T/2$, in the middle of the lattice. Doing this we obtain a symmetric signal with respect to forward and backward propagating pions (modulo the possible sign factor $(-1)^{n_4}$, c.f. Eq. (4.45)).

Inserting into the ratio the two- and three-point functions, Eqs. (4.9) and (4.45), one can show that most of the exponentials containing the time dependence and all of the overlap factors such as $\langle 0|\,\eta_\pi(\boldsymbol{p}')\,|\pi(\boldsymbol{p}')\rangle$ vanish. We arrive at

$$R(\tau) = \frac{\langle\pi(\boldsymbol{p}')|\,\mathcal{O}\,|\pi(\boldsymbol{p})\rangle}{4\sqrt{E_\pi(\boldsymbol{p}')E_\pi(\boldsymbol{p})}}\,\left[\frac{(1+e^{-2\tau E_\pi(\boldsymbol{p})})(1+e^{-2(T-2\tau)E_\pi(\boldsymbol{p}')})}{(1+e^{-2\tau E_\pi(\boldsymbol{p}')})(1+e^{-2(T-2\tau)E_\pi(\boldsymbol{p})})}\right]^{\frac{1}{2}}\,. \tag{4.59}$$

The time dependence is still not very obvious. This is because we cannot neglect the full time dependence of the two-point function (we have to include both exponentials, the forward and the backward propagating pion), unlike for the three-point function where we could limit ourselves to the signal on either side of the sink. This is also in contrast to the nucleon case where it is possible to project onto a state with definite parity, also simplifying the time-behaviour of the two-point function to a single exponential, see e.g. [55]. So we define $\delta \equiv \tau - T/4$ and expand the ratio and its exponentials in Eq. (4.58) around $\delta = 0$. This leads to

$$R(\tau) = C(\boldsymbol{p},\boldsymbol{p}')\left[1 + 2\delta\,c_\delta(\boldsymbol{p},\boldsymbol{p}') + 2\delta^2\,c_\delta^2(\boldsymbol{p},\boldsymbol{p}') + \mathcal{O}(\delta^3)\right]\,, \tag{4.60}$$

where

$$c_\delta(\boldsymbol{p},\boldsymbol{p}') = \frac{E_\pi(\boldsymbol{p}')}{1+e^{E_\pi(\boldsymbol{p})\,T/2}} - \frac{E_\pi(\boldsymbol{p})}{1+e^{E_\pi(\boldsymbol{p}')\,T/2}}\,,$$
$$C(\boldsymbol{p},\boldsymbol{p}') = \frac{\left\langle \pi(\boldsymbol{p}')\right|\mathcal{O}\left|\pi(\boldsymbol{p})\right\rangle}{4\sqrt{E_\pi(\boldsymbol{p}')E_\pi(\boldsymbol{p})}}\,. \tag{4.61}$$

Eq. (4.60) shows that we expect a plateau within the ratio only for $|\boldsymbol{p}| = |\boldsymbol{p}'|$. All other cases exhibit a *pseudo*-plateau. That is, we obtain an approximately antisymmetric signal around the time slice $T/4$, the central points of the l.h.s. of the ratio with respect to the sink. Note again that the nucleon case is somewhat simpler and exhibits a plateau for all momenta straight away. The leading symmetric term in (4.60) is small for our pion masses and lattice momenta; for lattice spacing a we have $c_\delta^2 \sim 10^{-4}a^{-2}$ and $\delta^2/a^2 \lesssim \mathcal{O}(10)$ for our setup. When we then average $R(\tau)$ in a symmetric interval around $T/4$, also the antisymmetric piece proportional to c_δ in (4.60) drops out and we can extract the expectation value of the operator. The same is true for the r.h.s. of our signal. The central point of the pseudo-plateau here is $3T/4$. Since the signal is independent of the time ordering (up to the sign factor) we use both pseudo-plateaus to indirectly increase the statistics. Hence we average over two intervals around the central points of both sides. Example plots of this ratio with its (pseudo-)plateau will be shown with the results in Chapter 6.

The factors of the pion energy $E_\pi(\boldsymbol{p})$ that appear in the relativistic normalisation in Eq. (4.61) are obtained from the continuum dispersion relation and the lattice pion masses. There are several reasons for this: first of all the fitting procedure is not complicated by having to fit pion energies directly, which becomes more and more difficult due to the increase in noise with higher momenta. In addition, we find that the continuum dispersion relation holds well for our lattices, so we do not need a discretised version thereof. In the end, we also match our lattice ratios to continuum form factors and their kinematic prefactors, Eqs. (2.23a) and (2.23b), where we can associate the normalisation with. This could give rise to more profound discretisation errors without remedy so far. However, there are also no indications for an additional source of error.

A potential problem with the ratio (4.58) remains: it contains pion two-point functions evaluated at the sink. Due to the exponential decay of the pion two-point function, Eq. (4.8), the signal at the sink can be poor for non-vanishing momenta. For finite statistics the two-point function can then take negative values, which prevents one from evaluating the square root. We try to overcome this difficulty by shifting the two-point functions $C_{2\mathrm{pt}}(t,\boldsymbol{p})$ that enter with $t = T/2$. Using the identity

$$C_{2\mathrm{pt}}(T/2,\boldsymbol{p}) = \frac{C_{2\mathrm{pt}}(T/2-t_{\mathrm{shift}},\boldsymbol{p})}{\cosh(E_\pi(\boldsymbol{p})\,T/2)} \tag{4.62}$$

we will shift by $t_{\mathrm{shift}} = 6$, which significantly reduces the number of negative two-point functions. Nevertheless there will still occur momentum transfers $\boldsymbol{q}$ for which the argument of the square root in the ratio (4.58) is negative. Those values are discarded when we evaluate the expectation value of the operator.

Finally, the values for the matrix elements are then extracted from the data making use of all possible operator and momentum combinations. This means we are neither limited to the case where $|\boldsymbol{p}| = |\boldsymbol{p}'|$ and a simpler ratio would suffice as mentioned above. Nor do

we have to use a specific component of, say the vector operator, which would then simplify the parametrisation. We perform a matching of the operator expectation value and the corresponding parametrisation in generalised form factors (c.f. Sec. 2.6.2), i.e. the ratio $R(\tau)$ is computed for all possible momenta and space-time indices and then compared to the GFFs, [55]. In general, this leads to an over-determined set of equations that is solved for the GFFs, making the extraction of the expectation values more reliable.

4.5 A Note on Scales

So far we have avoided another technical detail of lattice calculations: setting the scale of physical quantities. As mentioned in the last chapter, the lattice spacing a is not a parameter of lattice QCD, it has to be determined from the simulation. The only parameters are the quark masses (determined by κ) and the gauge coupling (determined by β). In a dynamical simulation, the lattice spacing depends on both these parameters.

We need the lattice spacing because most quantities measured on the lattice are in lattice units and we need to convert them to physical values. For example, the physical spatial volume (which is important when discussing finite size effects) is $a^3 V_\mathrm{s}$ and hadron energies are extracted as am_H.

To set the scale, one resorts to observables that can be measured very accurately on the lattice. This can for example be the ρ-meson mass (for quenched calculations) or, as in our case, the static potential between quark and anti-quark. The ratio of the lattice observable to the physical value then yields the lattice spacing a in fm. The static potential in the continuum can phenomenologically be written as

$$V(r) = C - A/r + \sigma r\,, \tag{4.63}$$

where the r is the separation between the two quarks, and C, A and σ (the string tension) are parameters. The reference scale then is the Sommer parameter r_0 defined in terms of the force $F(r)$ between the quarks [56]

$$r_0^2 F(r_0) = 1.65\,. \tag{4.64}$$

The QCDSF/UKQCD collaborations calculated the values r_0/a for each of the lattices, which we use to convert to physical values. The problematic part of setting the scale with the Sommer parameter r_0 is that there is no precise phenomenological value, since it is connected to measurable quantities only via potential models. A common, however debated choice is to use $r_0 = 0.5$ fm. In this work, we chose the value 0.467 fm obtained from comparing the nucleon mass at different pion masses and lattice volumes to analytic predictions from chiral perturbation theory [57].[3] Comparable values for the Sommer parameter were also found in [58]. Recent investigations with additional input from the pion decay constant indicate that even smaller values are possible [59].

[3] Chiral perturbation theory is an effective field theory with pions as degrees of freedom. The perturbative expansion is then done in terms of the pion's energy. So it is - to some extent - possible to vary the pion mass and match the calculated quantities to lattice data.

5 Pion Two-Point Functions

This chapter begins the discussion of our results by a brief look at the pion two-point function. The lattice observable and its continuum form was introduced in Section 4.1. This is necessary to obtain the lattice pion mass and also to eliminate pion energies and overlap factors within the ratio for the three-point function, as explained in Section 4.4. We give the two pion interpolating fields used in this work and explain how the energy of the pion can be extracted. We then look at the dispersion relation which already provides hints about the quality of the pion currents.

Since the pion mass is a mandatory observable for almost any lattice simulation – after all one is interested in an extrapolation in m_π – it is routinely determined within the QCDSF/UKQCD collaboration. We quote these values in the appendix and give here mainly details important for this work. We will however neither discuss the effect of smearing nor in great length the results for the different lattices. This chapter is rather meant as a first example of the application of lattice techniques.

5.1 Interpolating Fields

In the previous chapter we explained the lattice techniques in general. The pion interpolating fields η_π and $\eta_\pi^\dagger$, Eq. (4.3a/b), used for the two-point functions in Eq. (4.1) were introduced but the explicit Dirac structure was not given. We decided to use more than one pion field because the different overlap with the desired pion (ground) state should result in a slightly different quality of the final signal. So all our calculations were done with two commonly used pion fields: the pseudo-scalar current and the fourth component of the axial vector current. For a given momentum $\boldsymbol{p}$ they read[1]

$$\eta_\pi(t,\boldsymbol{p}) = \frac{1}{\sqrt{V_\mathrm{s}}} \sum_{\boldsymbol{x}} e^{-\mathrm{i}\boldsymbol{p}\boldsymbol{x}}\ \bar{d}(x)\,\Gamma\,u(x)\,, \qquad \Gamma = \gamma_5 \text{ or } \gamma_4\gamma_5 \tag{4.3a}$$

with $u(x)$, $d(x)$ the up- and down-quark fields and $x_4 = t$. The creation operator is chosen accordingly. Both interpolating fields have the desired quantum numbers of the physical pion ($I^G(J^{PC}) = 1^-(0^{-+})$). In general we apply smearing as discussed in Section 4.1.1 to increase the overlap with the pion ground state.

5.2 Lattice Pion Mass

Extracting the mass of the pion states that have overlap with the vacuum is straightforward. The decomposition of the correlation function into states with definite energy,

$$\left\langle \eta_\pi(\boldsymbol{p},t)\eta_\pi^\dagger(\boldsymbol{p},t')\right\rangle = e^{-E_\pi(\boldsymbol{p})T/2}\left|\left\langle 0\right|\eta_\pi(\boldsymbol{p})\left|\pi(\boldsymbol{p})\right\rangle\right|^2 2\cosh\left[\left(T/2-\left(t-t'\right)\right)E_\pi(\boldsymbol{p})\right]+\ldots \tag{4.9}$$

[1] We again use a π^+ here.

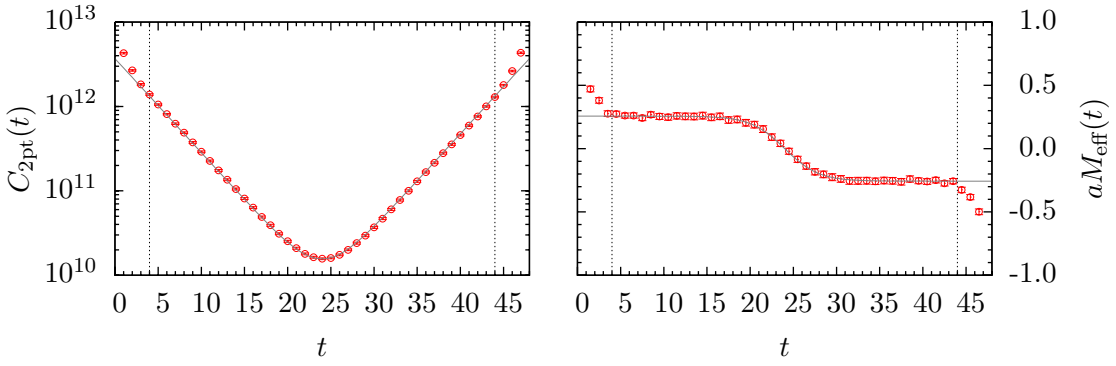

Figure 5.1 | The l.h.s. shows the raw lattice signal for the axial-vector pion current for lattice #6 (c.f. Table A.1); on the r.h.s. is the corresponding effective mass. Both are for vanishing momentum $\boldsymbol{p} = 0$. The solid lines indicate the fit to the two-point function within the indicated fit range.

displays what time behaviour to expect from the lattice signal and provides a fit ansatz. Note that we put our source at $t' = 0$. The fit parameters are the energy $E_\pi(\boldsymbol{p})$ of the pion state and the overlap of this state with the vacuum $\left|\left\langle 0\right|\eta_\pi(\boldsymbol{p})\left|\pi(\boldsymbol{p})\right\rangle\right|^2$. The fitting is done using a correlated χ^2 minimisation; errors are obtained with the bootstrap method.

For zero momentum, the energy is identical with the lattice pion mass. The ellipsis in Eq. (4.9) indicates the neglected excited states. Due to their higher mass, the corresponding exponentials die out more quickly. Hence a properly chosen fit range that does not start too close to the source of the two-point function only picks up the ground state. This can be checked and a rough idea of the fit range can be determined by considering effective mass plots. The effective mass M_{eff} is given by

$$M_{\mathrm{eff}}(t+1/2) = \log\left|\frac{C_{2\mathrm{pt}}(t+1)}{C_{2\mathrm{pt}}(t)}\right|. \tag{5.1}$$

If only a single state is present the effective mass should have a plateau if either of the exponentials dominate, i.e. the signal of the forward propagating pion for $t < T/2$ or the backward propagating pion for $t > T/2$. Around the $T/2$ the decay of both signals from either side is strongest and hard to distinguish from noise. This is also the region where the dominating signal changes and a cross-over from one plateau to the other appears. Deviations from a plateau close to the source on the other hand indicate excited states. As an example the data obtained from the lattice and the corresponding effective mass plot is shown for one lattice in Fig. 5.1. For this lattice the excited states are clearly absent for $4 \lesssim t \lesssim 44$. It is obvious from this figure and the functional form of Eq. (4.8) that the energy can approximately be read off from $M_{\mathrm{eff}}(t)$ for suitable time slices. Although having less parameters, a constant fit to the plateau is disfavoured over the ansatz in Eq. (4.8). The latter can be done for a symmetric fit range also including the time slices between the two plateaus and hence use much more data points. Such fits are indicated in Fig. 5.1 within the used fit range. The fit range is chosen to be as large as possible while having a stable fit upon changing the fit range. The pion masses for our lattices are given in Table A.1.

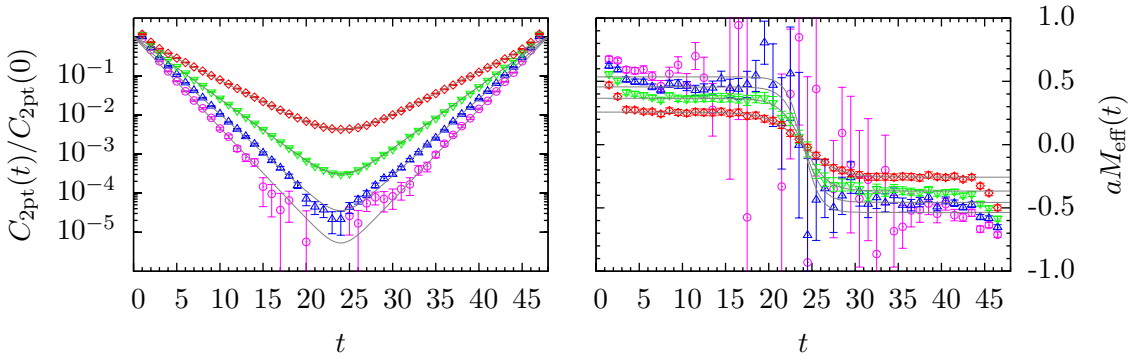

Figure 5.2 | Effective mass plots for different momenta along with fits to the lattice data for one lattice #6. We used the axial-vector pion source for these plots. The momenta are (top to bottom on the l.h.s.): $(0,0,0)$, $(0,0,1)$, $(0,1,1)$, and $(1,1,1)$

5.3 Dispersion Relation for the Pion

While the previous section focused on the pion mass m_π by looking at two-point functions with zero momentum, we will now take a look at the pion energies $E_\pi(\boldsymbol{p} \neq 0)$. This is done to justify the use of the continuum dispersion relation,

$$E_\pi^2 = m_\pi^2 + \boldsymbol{p}^2\,, \tag{5.2}$$

to calculate the energies for the relativistic pre-factor in Eq. (4.61). Instead of the continuum dispersion relation, the pion energies could also follow a lattice dispersion relation. The latter should reflect discretisation errors and is obtained from a bosonic action. For this, a discretised derivative with nearest neighbour interaction is used and the energy of the particles is calculated. One possible form then is (see e.g. [60])

$$\sinh^2\left(\frac{aE_\pi}{2}\right) = \sinh^2\left(\frac{am_\pi}{2}\right) + \sum_{i=1}^{3}\sin^2\left(\frac{ap_i}{2}\right), \tag{5.3}$$

where we have included the lattice spacing a explicitly. Note that the lattice dispersion relation has the correct continuum limit for $a \longrightarrow 0$ and that both versions, Eqs. (5.2) and (5.3), are equal in the limit of vanishing momenta. Correspondingly the difference between the two is big for large momenta only.

The pion energy, $E_\pi(\boldsymbol{p} \neq 0)$, is extracted from the lattice data performing fits to the cosh-ansatz as explained above. We have a number of momenta accessible and average over momenta that have the same magnitude but different directions. In units of $2\pi/L$ we have

$$\begin{aligned}\boldsymbol{p} = &(0,0,0),(1,0,0),(1,1,0),(1,1,1),\\ &(2,0,0),(2,1,1),(2,2,1),\cdots\end{aligned}$$

while the ellipsis stands for all possible permutations w.r.t. the components. Results of such fits are shown within effective mass plots in Fig. 5.2. This plot illustrates the increasing noise in the middle of the lattice and also illustrates that fitting to the effective mass would not lead to good results anymore. However, as a consequence of the worsened

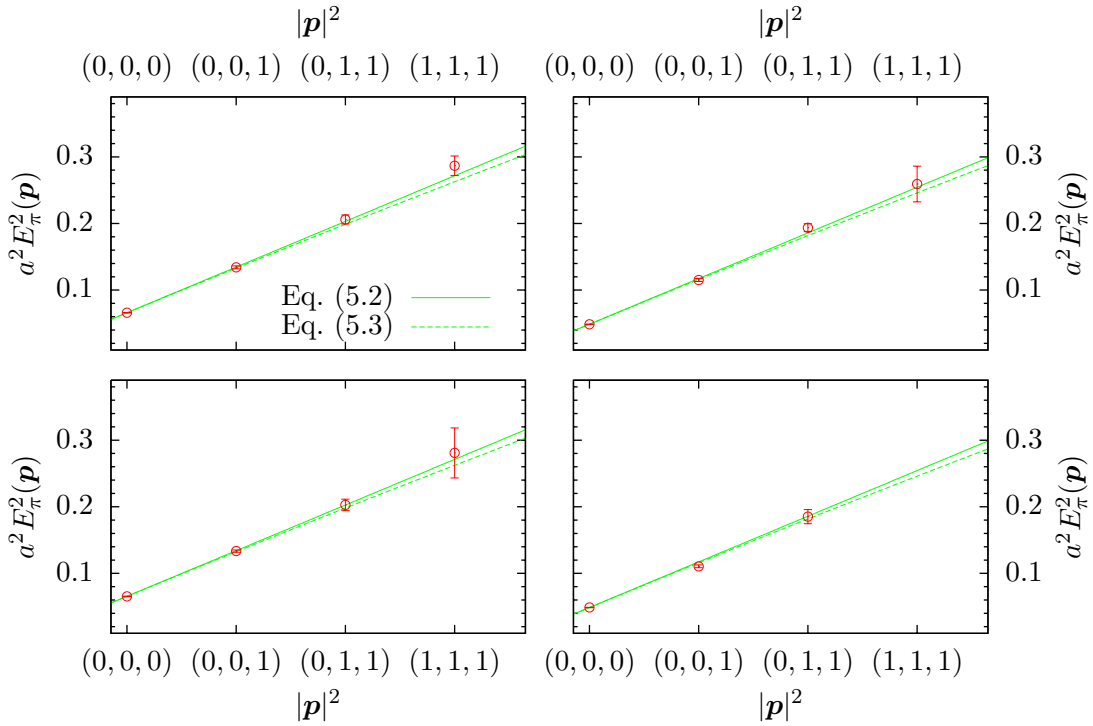

Figure 5.3 | Pion energies squared $E_\pi^2(\boldsymbol{p})$ for two lattices [#6 (l.h.s.) #17 (r.h.s., smaller a)] with the two dispersion relations, Eqs. (5.2) and (5.3). Shown are results for both of our pion interpolating fields (*top*: axial current, *bottom*: pseudo-scalar current). The momenta are indicated by one of their possible permutations.

signal we were not able to extract a stable signal for the highest momenta. Here the signal literally drowns in noise. We want to stress that these fits were only performed to test the dispersion relation. Neither our simulation nor the analysis was particularly focused in obtaining these energies. While we do need the two-point functions for our ratios of three-point functions, we do not need to fit them. To some extent, the noise of the two-point functions for $\boldsymbol{p} \neq 0$ should average out in our ratios.

To check for a continuum like behaviour, the square of the energy for a sample of lattices is plotted against the momentum squared $|\boldsymbol{p}|^2$ in Fig. 5.3. Included are both dispersion relations and both pion interpolating fields. The lattices are chosen to have varying lattice spacing a since a bigger discrepancy between the dispersion relations could be expected for larger lattice spacing. Still, we see no indication that a lattice dispersion relation is better fulfilled than the continuum one. This can be explained by our lattice action. We do not use a naïve discretisation, but instead the Clover improved version discussed in Section 3.5. Since the action is especially selected, to get rid of $\mathcal{O}(a)$ terms, the continuum is restored much quicker, which also affects the dispersion relation. We conclude from Fig. 5.3 that the continuum dispersion relation can be used for estimating the energies for the relativistic pre-factor of Eq. (4.61). This is certainly true within the statistical significance of the data. The conclusion might change when much higher momenta are desired, c.f. [61].

Another observation during tests of the dispersion relation is a difference in the quality of the signal of the pseudo-scalar and the axial pion source. Looking at the raw lattice

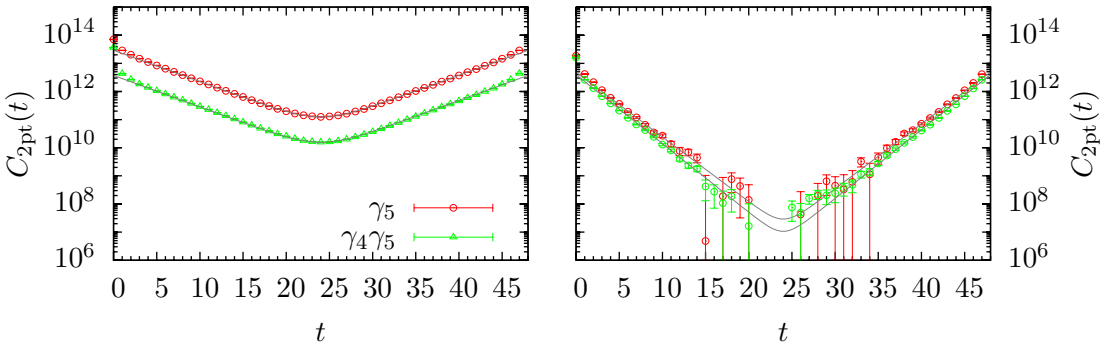

Figure 5.4 | The l.h.s. shows lattice #6 for $\boldsymbol{p} = (0, 0, 0)$ where the pseudo-scalar interpolator has larger overlap. The r.h.s. is for $\boldsymbol{p} = (1, 1, 1)$ with comparable overlap and changed signal quality.

two-point function, the pseudo-scalar has a better signal and significantly larger overlap for vanishing momentum. As the momentum $\boldsymbol{p}$ is increased, the axial current seems to provide the better signal, see Fig. 5.4. This tendency is reflected in the ability to better extract the pion energies for larger momenta. This is in line with [61] where the authors draw similar conclusions for the overlap of the pion currents with the vacuum and their errors. The better signal for the axial-vector pion current will find its continuation in the results from the three-point functions.

6 Pion Form Factor

We now turn to the results from our three-point functions. One observable here is the pion form factor, given by

$$\left\langle \pi(\boldsymbol{p}') \right| V_\mu \left| \pi(\boldsymbol{p}) \right\rangle = (p'_\mu + p_\mu)\, F_\pi(Q^2)\,. \qquad [1.7]$$

In the context of this work, the form factor F_π is equivalent to the lowest moment of the vector GPD H^π, Eq. (2.5a). It was introduced in Sections 1.2 and 2.6, and describes the distribution of the electric charge of the pion which has already been the subject of several lattice studies. We improve upon those in several points. First of all, like the pioneering work by Martinelli *et al.* and Draper *et al.* [52, 62] most of the previous results [63, 64, 65, 66, 67] have been obtained in the quenched approximation. State-of-the art simulations employ dynamical fermions [61, 68, 69]. Compared to those, our simulation is done with more lattices and hence has a much larger range of parameters. This enables us to investigate the necessary limits to compare to the physical value.

We use the local vector current $V_\mu = \frac{2}{3}\bar{u}\gamma_\mu u - \frac{1}{3}\bar{d}\gamma_\mu d$ for the lattice calculation, corresponding to $\mathcal{O}_\mu$ in Eq. (4.17a) with an appropriate flavour matrix. From Eq. (4.43) we know that one flavour is enough to obtain the matrix element. So in practice $\bar{u}\gamma_\mu u$ was used as inserted current.

The form factor is very well established by the experiments at DESY, CERN and JLab [70, 71, 72]. We will compare our results to the experimental data at the end of this chapter. Before we are able to do that, we have to discuss its dependence on the momentum transfer and investigate lattice artifacts. The final step then is the pertinent extrapolation in the lattice pion mass. While most of the following discussion will be for a parameter describing the momentum dependence of the form factor, we will also relate that to the pion charge radius, $\langle r^2 \rangle$, and provide results for that as well.

Parts of the material presented in this chapter are published in [73].

6.1 Plateaus from Lattice Data

In a similar fashion as for the two-point functions in the previous chapter, we again need some kind of plateau within the lattice data we can fit to. The fitting procedure is simplified by calculating a ratio of three- and two-point functions as discussed in Section 4.4. We recall the ratio here

$$R(\tau) = \frac{C_{3\mathrm{pt}}(\tau, \boldsymbol{p}', \boldsymbol{p})}{C_{2\mathrm{pt}}(t, \boldsymbol{p}')} \left[\frac{C_{2\mathrm{pt}}(t-\tau, \boldsymbol{p})\, C_{2\mathrm{pt}}(\tau, \boldsymbol{p}')\, C_{2\mathrm{pt}}(t, \boldsymbol{p}')}{C_{2\mathrm{pt}}(t-\tau, \boldsymbol{p}')\, C_{2\mathrm{pt}}(\tau, \boldsymbol{p})\, C_{2\mathrm{pt}}(t, \boldsymbol{p})} \right]^{\frac{1}{2}}. \qquad [4.58]$$

with its approximate relation

$$R(\tau) = \frac{\left\langle \pi(\boldsymbol{p}') \right| V_\mu \left| \pi(\boldsymbol{p}) \right\rangle}{4\sqrt{E_\pi(\boldsymbol{p}') E_\pi(\boldsymbol{p})}} \left[1 + 2(\tau - T/4) \left(\frac{E_\pi(\boldsymbol{p}')}{1 + e^{E_\pi(\boldsymbol{p})\, T/2}} - \frac{E_\pi(\boldsymbol{p})}{1 + e^{E_\pi(\boldsymbol{p}')\, T/2}} \right) + \dots \right], \qquad [4.60]+[4.61]$$

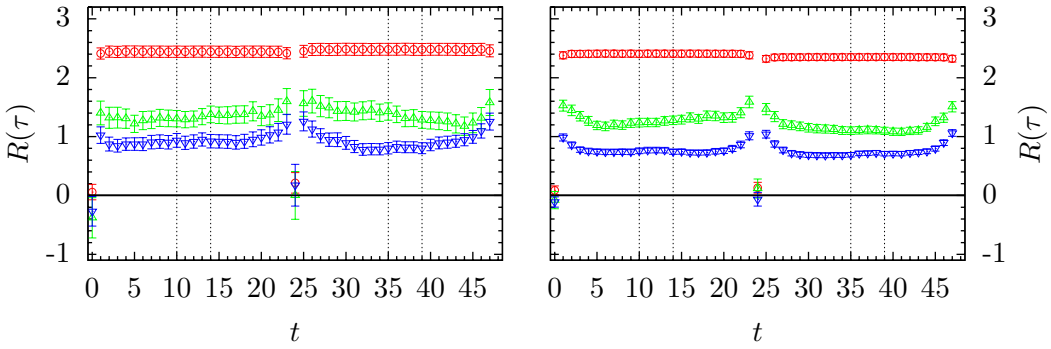

Figure 6.1 | Plateaus from lattice data in the special case of $|\boldsymbol{p}| = |\boldsymbol{p}'|$. The l.h.s. (r.h.s.) is representative for light (heavy) pions [lattices #6 and #16]. From top to bottom for momentum transfer $|\boldsymbol{q}| = 0, \sqrt{2}, 2$. The region where we extract our signal is indicated by the dashed lines. In between our signal is approximately constant in time. Thus we can ignore excited states.

that shows the pseudo-plateau used for our fits. Our simulation is done fixing the momentum transfer $\boldsymbol{q}$ and the final momentum $\boldsymbol{p}'$, as shown in Sec. 4.3. We chose our lattice momenta specifically for our set-up: since the second inversion of the sequential source technique (see Sec. 4.3.1) has to be done for every new set of quantum numbers at the sink, the number of values for the final state momentum is limited to three. The momentum transfer however does not require a big computational effort and we thus have a total of 17 different momenta $\boldsymbol{q}$. In units of $2\pi/L$ we have

$$\begin{aligned} \boldsymbol{p}' &= (0,0,0), (0,1,0), (0,0,1), \\ \boldsymbol{q} &= (0,0,0), (-1,0,0), (-1,-1,0), (-1,-1,-1), \\ &\quad (-2,0,0), (-2,-1,-1), (-2,-2,-1), \cdots \end{aligned} \tag{6.1}$$

where the ellipsis again stands for all possible permutations w.r.t. the components. Out of the 51 possible combinations, 17 survive which have a distinct momentum transfer $Q^2 = (p' - p)^2$. In general, (4.58) will not be constant in time. This is not related to contributions from excited states as explained in Section 4.4. Excited states are omitted in our equations because we assume that $t - \tau \gg 1/(E'_\pi - E_\pi)$ and $\tau \gg 1/(E'_\pi - E_\pi)$. To avoid confusion and demonstrate that we are indeed not plagued by excited states, let us start with the special case where the norm of the incoming and outgoing momentum is identical, so where we have $|\boldsymbol{p}| = |\boldsymbol{p}'|$. In this case, the energies appearing in Eq. (4.58) are identical as well and the time dependence of the ratio disappears. If we have ground state pions only, we can then expect to find a plateau in our lattice data. This is shown for some lattices in Fig. 6.1. The plots are for the fourth component of the vector current, two pion masses and three momentum combinations (starting with the case where $\boldsymbol{p} = \boldsymbol{p}'$ at the top). There are no deviations from a plateau in the indicated region we use to extract the three-point function (c.f. Sec. 4.4). The signal is constant in time (certainly for lower momenta and within the statistical errors) and we can safely ignore excited states. Note that we have a fixed fit range as indicated and do not increase the range individually (for $\boldsymbol{p} = \boldsymbol{p}'$ for example).

Let us now turn to the more general case where the norm of the momenta $\boldsymbol{p}$ and $\boldsymbol{p}'$ can

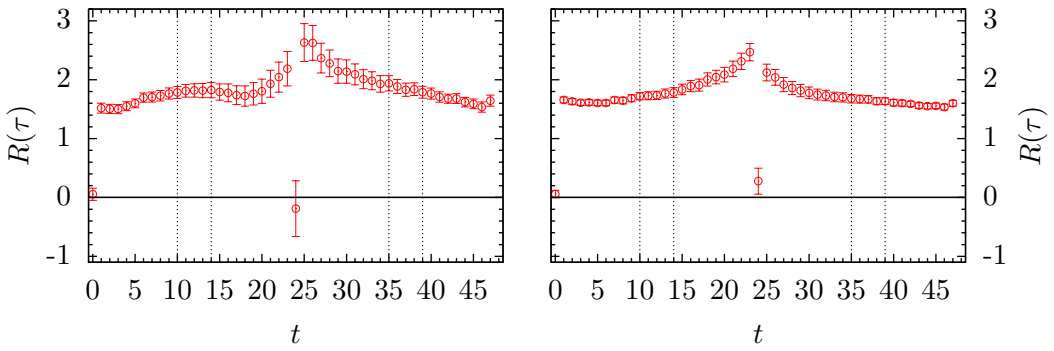

Figure 6.2 | This figure shows examples of the expected pseudo-plateaus, c.f. Sec. 4.4. The l.h.s. is for lattice #6 with $Q^2 = 0.31\,\mathrm{GeV}^2$, the r.h.s. is for lattice #16 and $Q^2 = 0.43\,\mathrm{GeV}^2$.Indicated is again the range of time slices we use to extract our data.

be different. We already mentioned that we do not obtain a plateau from Eq. (4.60) in the more general case. Instead, what we find are the pseudo-plateaus introduced and explained in Sec. 4.4. Some examples are shown in Fig. 6.2, where the r.h.s. part of the signal is multiplied with a minus sign if required, Eq. (4.45). The two adjacent time slices on either side of $t = T/4$ for the l.h.s. and $t = 3T/4$ for the r.h.s. are then averaged to obtain the values used for the three-point function in Eq. (1.7). This region is again indicated by the vertical lines in the figure. We increase the quality of the signal by combining both sides to one value. This is equivalent to increasing the statistics of our data. We use the Jackknife procedure to obtain errors during our fits to the form factor.

6.2 Momentum Dependence

In order to properly extract the pion form factor, F_π, we want to measure it for a large range of momenta Q^2. Since we will have at most 17 data points as mentioned in the previous section, we need a function to interpolate between these points and describe $F_\pi(Q^2)$. The finite size of our lattice with its periodic boundary condition limits the possible momenta to a discretised set with a *fixed minimum value*, Eq. (3.35). Good knowledge of the momentum dependence is hence especially important for the pion charge radius since it is obtained from $F_\pi(Q^2)$ for $Q^2 \longrightarrow 0$.

6.2.1 Monopole Ansatz

The form factor data of e.g. the nucleon is generally described by fitting to an n-pole ansatz where n is a small integer. For the pion and its experimental data it is found that a monopole form

$$F_\pi(Q^2) = \frac{F_\pi(0)}{1 + Q^2/M^2} \tag{6.2}$$

with a monopole mass M describes the data best. Historically this was explained with a model called vector meson dominance (VMD), see e.g. [74]. In this model an additional cascade of exchange particles occurs between photon and pion where the dominating particle would be the ρ vector meson. This however corresponds to an effective theory and

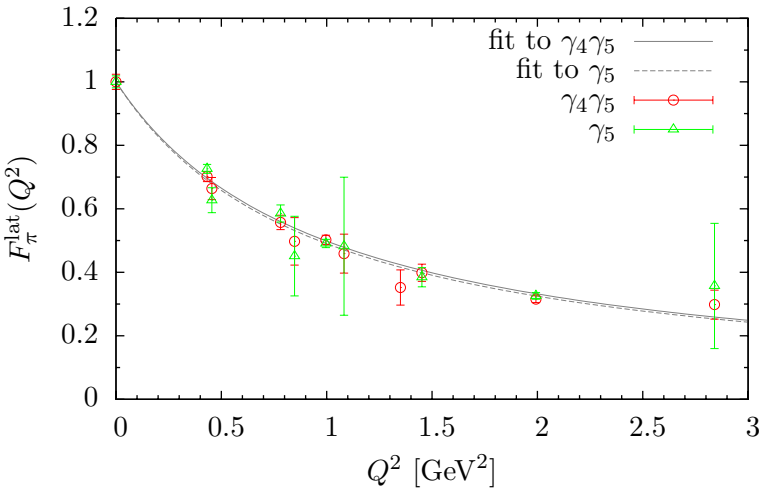

Figure 6.3 | Here we show the data for both pion interpolating fields with fits according to (6.2) for lattice #16. Note the better signal for the axial-vector source. The fit parameters are given in Tab. 6.1.

not full QCD. Using the ansatz (6.2) to fit the experimental data [70, 71, 72] with a Q^2 up to 2.54 GeV^2 we find $M = 0.714(4)$ GeV with a χ^2/d.o.f. $= 1.27$. Comparing this to a fit of the data with $Q^2 \leq 0.253$ GeV^2 from only [70] giving $M = 0.719(5)$ GeV with χ^2/d.o.f. $= 1.13$, we conclude that the monopole form can be used to describe the data for a very large (at least up to 2.5 GeV^2) range of momentum transfer and not only for small momenta as suggested by the effective theory.

Before we can apply the fitting ansatz to our lattice data, we need to renormalise our bare results to obtain a physical value, $F_\pi^{\mathrm{ren}} = Z_V F_\pi^{\mathrm{bare}}$. This was already mentioned in Sec. 4.2.1. Since we know the exact value of $F_\pi(0) = 1$ from gauge invariance, we can use that as input and write

$$F_\pi^{\mathrm{lat,ren}}(Q^2) = \frac{F_\pi^{\mathrm{lat,bare}}(Q^2)}{F_\pi^{\mathrm{lat,bare}}(0)}\,, \tag{6.3}$$

so that $F_\pi^{\mathrm{lat,ren}}(0) = F_\pi^{\mathrm{phys}}(0) = 1$. We have introduced a number of superscripts here to distinguish the various quantities. In the following, we will mainly use 'lat' and 'phys' to refer to lattice observables or their corresponding values at the physical point. To fit our now renormalised lattice data, we will use

$$F_\pi^{\mathrm{lat}}(Q^2) = \frac{1}{1 + Q^2/M_{\mathrm{lat}}^2}\,, \tag{6.2}$$

with lattice monopole mass M_{lat} as fit parameter. The results for all our lattices and both pion interpolating fields (see Sec. 5.1) are given in Table 6.1. In general, the matrix elements for pions using the axial-vector source with $\Gamma = \gamma_4\gamma_5$ display a slightly cleaner signal with more data points in Q^2, i.e. less contamination due to negative two-point functions. An example for this and the monopole fit is given in Fig. 6.3. As shown in Table 6.1, fitting the monopole form (6.2) to the form factor for both pion interpolators we find that the χ^2/d.o.f. differs on average by about a factor of two, ranging from 0.18 – 1.72 (0.18 – 4.37) for the interpolator with $\gamma_4\gamma_5$ (γ_5). The fitted monopole masses for the $\Gamma = \gamma_5$

Table 6.1 | Monopole masses M_{lat} obtained from fits to (6.2) for each of our lattices. Values for the pseudo-scalar source and the fourth component of the axial-vector are given separately. Errors are statistical only.

#	m_π [GeV]	$M_{\text{lat}}^{\text{ps}}$ [GeV]	χ^2/d.o.f.	$M_{\text{lat}}^{\text{av}}$ [GeV]	χ^2/d.o.f.
1	1.007(2)	1.118(21)	0.183	1.105(22)	0.183
2	0.833(3)	1.031(22)	0.943	0.997(21)	0.419
3	0.619(3)	0.974(29)	2.172	0.880(24)	0.507
4	0.987(2)	1.133(22)	0.565	1.080(20)	0.281
5	0.829(3)	1.032(20)	1.723	0.975(18)	0.651
6	0.597(1)	0.899(24)	0.563	0.870(22)	0.831
7	0.447(1)	0.974(36)	0.633	0.747(18)	1.600
8	1.011(3)	1.108(27)	0.834	1.066(25)	0.414
9	1.173(2)	1.189(22)	0.620	1.157(20)	0.503
10	0.929(2)	1.069(17)	1.361	1.051(15)	0.892
11	0.769(2)	0.985(13)	1.426	0.971(14)	0.676
12	0.592(2)	0.895(16)	1.279	0.854(15)	0.861
13	0.402(2)	0.872(44)	4.369	0.783(29)	1.596
14	0.336(2)	0.866(65)	0.278	0.708(43)	1.230
15	1.037(1)	1.113(11)	1.293	1.099(11)	1.718
16	0.842(2)	0.996(14)	1.198	0.981(14)	0.526
17	0.626(2)	0.869(20)	2.091	0.847(17)	0.654
18	0.444(3)	0.888(43)	1.171	0.690(18)	0.817

pions lie above the ones for $\Gamma = \gamma_4\gamma_5$ but are consistent. We made a similar observation for the quality of the signal for the two-point functions in Sec. 5.3 which may explain the difference in quality of the form factors extracted from the two pion currents. Because of the better signal, we will mainly discuss results for the pions created with $\Gamma = \gamma_4\gamma_5$ in the remainder of this work.

6.2.2 Effective Monopole Mass

Because the rest of the analysis relies on the fit ansatz in Eq. (6.2), we have to make sure that it provides a good description of our data for all values of the momentum transfer Q^2. One possibility here is to assume that the monopole form is a valid functional form. Then the leading behaviour of $1/F_\pi$ is linear which can be checked [66]. We instead evaluate an effective monopole mass for every value of Q^2 by solving Eq. (6.2) for M_{lat}

$$M_{\text{eff}}(Q^2) = Q\left[\frac{1}{F_\pi^{\text{lat}}(Q^2)} - 1\right]^{-1/2}. \tag{6.4}$$

Please note that while called the same, M_{eff} is now very much different from the effective masses for the two-point functions used in Ch. 5. We show such effective masses for some of our lattices in Fig. 6.4. Here one can see that the effective monopole masses stay constant within errors over a large range of Q^2 and agree with the monopole masses given in Table 6.1. This already indicates that the monopole is a good description for our data. The validity of the fit over the whole Q^2 range will further be tested in Sec. 6.5.

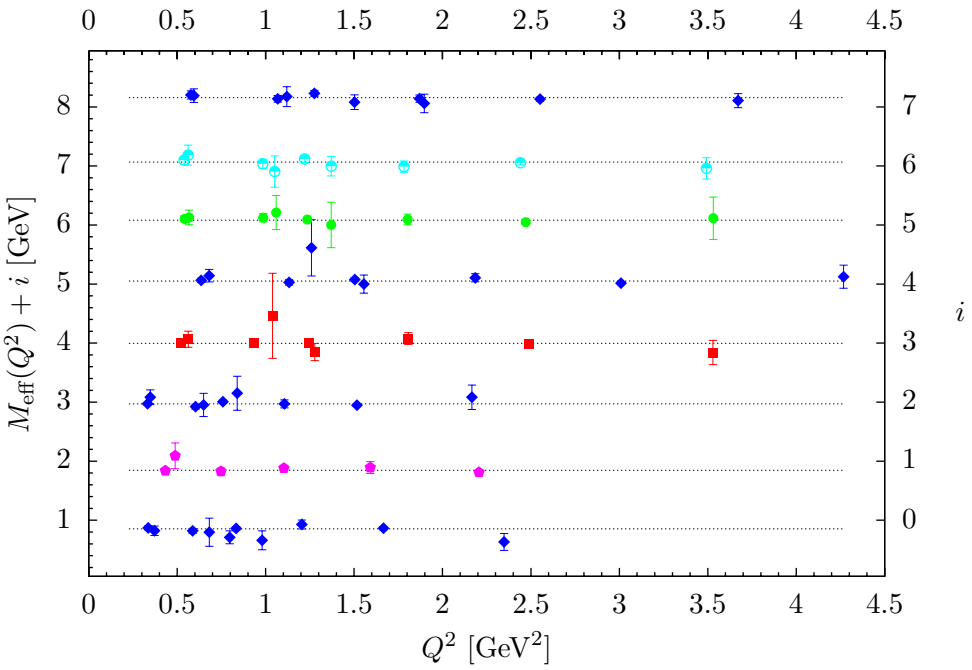

Figure 6.4 | Effective monopole masses $M_{\text{eff}}(Q^2)$ defined in (6.4), together with the corresponding monopole masses from Table 6.1 (dotted lines) for a sample of our lattices from small to large pion masses (lattices number 9, 8, 4, 10, 2, 11, 17, and 12 from top to bottom). For better visibility we omitted two points with very large errors in the plot, but included them in the fit.

6.3 Operator Improvement

The improvement scheme that was used to reduce the discretisation errors of the fermion action (Sec. 3.5) can also be applied to the vector operator V_μ used for our matrix element (1.7). The $\mathcal{O}(a)$ improved local vector current has the form (ignoring $\mathcal{O}(a^2)$ effects) [75]

$$\begin{aligned} V_\mu^{\text{imp}}(x) &= \bar{u}(x)\gamma_\mu u(x) + c_V\, a\partial_\nu T_{\mu\nu}(x)\,, \\ T_{\mu\nu}(x) &= \mathrm{i}\,\bar{u}(x)\sigma_{\mu\nu}u(x)\,. \end{aligned} \tag{6.5}$$

The improvement would also add an additional multiplicative term to the renormalisation constant Z_V (proportional to the quark mass), c.f. Eq. (4.24). However, since we normalise our raw lattice data, Eq. (6.3), we can neglect that and only need one improvement coefficient c_V. Instead of directly putting the improved current (6.5) on the lattice we make use of our data acquired for the moments of the tensor GPD $H_{\mathrm{T}\,\pi}$, Eq. (2.5b). For that, we write (6.5) in form of two matrix elements

$$\langle\pi|\, V_\mu^{\text{imp}}\,|\pi\rangle = \langle\pi|\, V_\mu\,|\pi\rangle + c_V\,\langle\pi|\, a\partial_\nu T_{\mu\nu}\,|\pi\rangle\,. \tag{6.6}$$

The only complication now is that we do not have the tensor matrix elements for all lattice sites. Due to the momentum projection in (4.33), we have summed over the spatial components. The lattice derivative, however, is formulated in form of the difference of

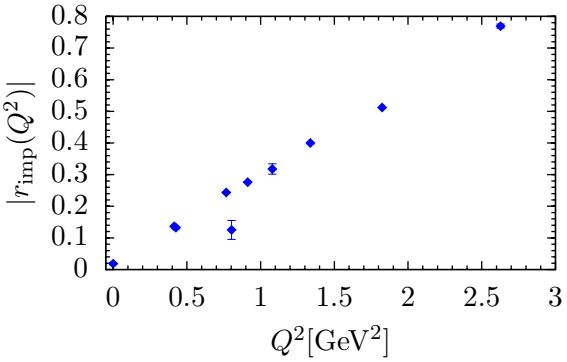

Figure 6.5 | The ratio $r_{\mathrm{imp}}(Q^2)$ defined in Eq. (6.10), evaluated for our coarsest lattice ($\beta = 5.20$, $\kappa = 0.1342$). To obtain the effect of $\mathcal{O}(a)$ improving the current, this ratio needs to be multiplied with c_V.

neighbouring sites

$$a\partial_\nu T_{\mu\nu}(x) = \frac{1}{2}\sum_{\nu=1}^{4}\left[T_{\mu\nu}(x+\hat{\nu}) - T_{\mu\nu}(x-\hat{\nu})\right] . \tag{6.7}$$

The time component is still trivially calculated. Taking the Fourier transform of the spatial components, this can be rewritten to

$$\sum_{\boldsymbol{x}} e^{\mathrm{i}\boldsymbol{q}\boldsymbol{x}} a\partial_i T_{\mu i}(x) = -\mathrm{i}\sin(q_i) T_{\mu i}(0)\, e^{\mathrm{i}\boldsymbol{q}\boldsymbol{x}}. \tag{6.8}$$

We then arrive at a combination of matrix elements in momentum space that are readily at our hand

$$\begin{aligned}\left\langle \pi(\boldsymbol{p}')\right| a\partial_\nu T_{\mu\nu}(t) \left|\pi(\boldsymbol{p})\right\rangle =& \frac{1}{2}\Big[\left\langle \pi(\boldsymbol{p}')\right| T_{\mu 4}(t+1) \left|\pi(\boldsymbol{p})\right\rangle - \left\langle \pi(\boldsymbol{p}')\right| T_{\mu 4}(t-1) \left|\pi(\boldsymbol{p})\right\rangle\Big] \\ & - \mathrm{i}\sum_{i=1}^{3}\sin(q_i)\, \left\langle \pi(\boldsymbol{p}')\right| T_{\mu i}(t) \left|\pi(\boldsymbol{p})\right\rangle .\end{aligned} \tag{6.9}$$

To estimate the size of the tensor term, we look at the ratio of the two separate parts

$$r_{\mathrm{imp}}(Q^2) = \frac{\left\langle \pi(p')\right| a\partial_\nu T_{\mu\nu} \left|\pi(p)\right\rangle}{\left\langle \pi(p')\right| \bar{u}\gamma_\mu u \left|\pi(p)\right\rangle} . \tag{6.10}$$

Note that the improvement coefficient c_V did not enter yet. In Fig. 6.5 we plot the ratio $r_{\mathrm{imp}}(Q^2)$ for our coarsest lattice which should experience the biggest change from improving the vector current. For the relative change w.r.t. the unimproved local vector current, we have to multiply $r_{\mathrm{imp}}(Q^2)$ with c_V. However, the only non-perturbative calculations of this improvement coefficient to date are for quenched fermions [46]. This means we have to resort to perturbative results which are known to produce values which are not reliable, see e.g. [47]. A tadpole improved relation for c_V is [75, 76]

$$c_V = -0.01225(1) \times \frac{4}{3}\frac{g^2}{u_0^4} , \tag{6.11}$$

Table 6.2 | The tentative shift of the monopole mass for some of our lattice. This is using an arbitrary, rather large and constant value for c_V, as discussed in the text.

#	β	a [fm]	M_{lat}[GeV]	$M_{\text{lat}}^{\text{imp}}$[GeV]	change
1	5.20	0.11	1.105(21)	1.206(26)	9%
2	5.20	0.10	0.997(20)	1.100(25)	10%
3	5.20	0.09	0.880(23)	0.961(27)	9%
4	5.25	0.10	1.080(19)	1.183(24)	9%
5	5.25	0.09	0.975(17)	1.058(21)	9%
6	5.25	0.08	0.870(22)	0.932(25)	7%
9	5.29	0.10	1.157(20)	1.265(24)	9%
10	5.29	0.09	1.051(15)	1.144(17)	9%
11	5.29	0.08	0.971(13)	1.024(16)	5%
12	5.29	0.08	0.854(15)	0.914(17)	7%
13	5.29	0.08	0.783(29)	0.831(32)	6%
15	5.40	0.08	1.099(11)	1.169(14)	6%
16	5.40	0.07	0.981(14)	1.052(15)	7%
17	5.40	0.07	0.847(17)	0.902(18)	7%

where u_0 is proportional to the averaged Wilson plaquette term: $u_0 = \left\langle \frac{1}{3} \mathrm{Tr}\, U_{\text{plaq}} \right\rangle^{1/4}$. From Eq. (6.11) we compute $c_V \approx -0.027$ for $\beta = 5.20$. Together with Fig. 6.5 we estimate a shift of $\sim 3\%$ for the largest Q^2 value. Compared to our statistical errors this is certainly negligible, especially for our finer lattices. Since the value for c_V is likely to be underestimated we also check the form factor F_π using the improved current and fixed $c_V = -0.3$. This neglects the dependence of c_V on β and is more than ten times larger than the tadpole improved value for our coarsest lattice. Still, this overestimated shift of the extracted monopole mass was moderate with 5 to 10%. The results of this test are given in Table 6.2. With our statistical errors on F_π in mind and the fact that a reliable value for the improvement coefficient c_V is not known for our lattices, we decide to neglect the improvement term in Eq. (6.5). We instead stick to the unimproved local vector current for our analysis.

6.4 Extrapolation to the Physical Point

Having established an ansatz for the momentum dependence of our data in Sec. 6.2 we can investigate the dependence on the lattice pion mass, generally called chiral extrapolation. Chiral extrapolations are commonly done in the square of the pion mass. We tried different, rather simple extrapolations which we will discuss here. A separate section at the end of this chapter is devoted to more sophisticated attempts using chiral perturbation theory.

We give the functional forms we tried in Tab. 6.3. Fit 1 might be motivated by VMD and the fact that the rho meson mass is linearly extrapolated versus the square of the pion mass. Fit 2 is another empirically motivated form, while Fit 3 is an attempt of a linear extrapolation of the pion charge radius (see Eq. (1.9) or Sec. 6.7). The best χ^2 value is found for Fit 2, where M_{lat}^2 depends linearly on m_π^2. An extrapolation with this ansatz together with its error band is shown in Fig. 6.6. We will base the extrapolations

Table 6.3 | Different forms used to extrapolate the monopole mass to the physical value of m_π. Both with and without the lightest pion masses.

#	extrapolation ansatz	χ^2/d.o.f.	c_1	M_{phys} [GeV]
	without the lightest pions			
1	$M_{\text{lat}} = c_0 + c_1 m^2_{\pi,\text{lat}}$	1.40	$0.320(16)\,\text{GeV}^{-1}$	0.762(13)
2	$M^2_{\text{lat}} = c_0 + c_1 m^2_{\pi,\text{lat}}$	1.01	0.648(31)	0.726(16)
3	$1/M^2_{\text{lat}} = c_0 + c_1 m^2_{\pi,\text{lat}}$	3.30	$-0.567(32)\,\text{GeV}^{-4}$	0.835(9)
	including the lightest pions			
4	$M_{\text{lat}} = c_0 + c_1 m^2_{\pi,\text{lat}}$	4.01	$0.371(13)\,\text{GeV}^{-1}$	0.717(10)
5	$M^2_{\text{lat}} = c_0 + c_1 m^2_{\pi,\text{lat}}$	2.87	0.734(24)	0.674(12)
6	$1/M^2_{\text{lat}} = c_0 + c_1 m^2_{\pi,\text{lat}}$	7.29	$-0.652(30)\,\text{GeV}^{-4}$	0.811(7)

in the remainder of this chapter on this ansatz. For the final result, however, we include an estimated systematic error of $\Delta M_{\text{extra}} = 36\,\text{MeV}$ from the difference of Fits 1 and 2 (Fit 3 gives a significantly worse description of the data).

A note on our lightest pion masses

During the analysis of the complete set of lattices we encountered finite size effects, mainly for our four lightest pion masses, see Sec. 6.6.1. Similar observations were made for different observables measured on these lattices, for example the decay constant f_π. Already the lattice pion mass is affected, with an occurring lower bound depending on the lattice volume [78]. Because of these problems, we exclude these lattices for the moment and give their results in this section for completeness only. We will later try to convince the reader that these points are consistent with our conclusions and even support them.

6.5 Combined Fits and Tests of the Monopole Form

A global fit to all (but our four lightest) lattices, combining the ansatz for the momentum dependence and the extrapolation in the lattice pion mass can reduce the total number of parameters we have to fit. At the same time, the number of data points for the fit increases since it becomes two-dimensional. The combined fit has the same monopole form as Eq. (6.2) with one additional parameter for the m_π behaviour

$$\begin{aligned} F_\pi(Q^2, m_\pi^2) &= \frac{1}{1 + Q^2/M^2(m_\pi^2)}\,, \\ M^2(m_\pi^2) &= c_0 + c_1 m_\pi^2\,. \end{aligned} \tag{6.12}$$

The two fit parameters c_0 and c_1 describe the relation between the monopole mass and the pion mass, thus we immediately obtain the form factor $F_\pi^{\text{phys}}(Q^2) = F_\pi\,(Q^2, m^2_{\pi,\text{phys}})$ in the physical limit. The fitted parameters are $c_0 = 0.516(23)\,\text{GeV}^2$ and $c_1 = 0.647(32)$ with χ^2/d.o.f. $= 0.63$. This gives $M_{\text{phys}} = M(m^2_{\pi,\text{phys}}) = 0.727(17)\,\text{GeV}$, in good agreement with the result obtained from Fit 2 in Sec. 6.4. Figure 6.7 shows the combined fit with its

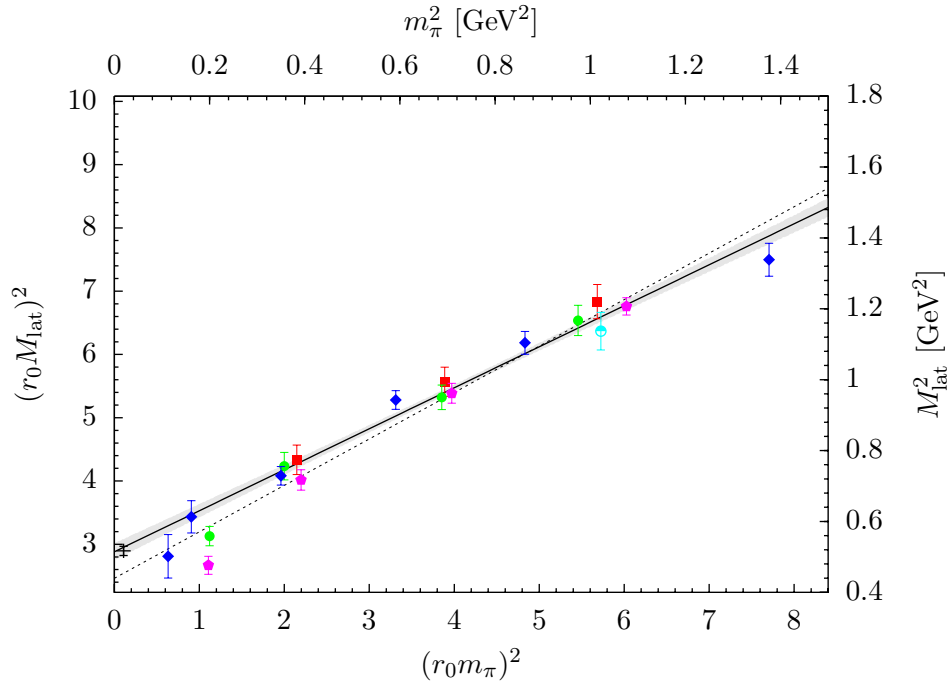

Figure 6.6 | Extrapolations of the squared monopole mass against the squared pion mass. The solid line with error band is a linear extrapolation as obtained from Fit 2 in Tab. 6.3 (excluding the 4 lightest pion masses) the dashed line corresponds to Fit 5. The cross marks the monopole mass corresponding to the PDG value [77] of the pion charge radius. The different symbols refer to our β-values: squares (5.20), circles (5.25), semi-filled circle (5.26), diamonds (5.29), and hexagons (5.40).

extrapolated curve. For this plot, our data at the lattice pion masses are shifted to the physical pion mass and plotted on-top of the extrapolation. We do this by subtracting from the individual lattice points, $F_\pi^{\rm lat}(Q^2)$, a value $\left(F_\pi(Q^2, m_{\pi,\rm lat}^2) - F_\pi(Q^2, m_{\pi,\rm phys}^2)\right)$ calculated with the fit parameters of Eq. (6.12) at the respective pion masses. The errors are left unchanged. The same fit for the pions with $\Gamma = \gamma_5$ gives $M_{\rm phys} = 0.777(17)\,\text{GeV}$, with a bigger χ^2/d.o.f. of 1.01.

Although Fig. 6.7 already displays that our fitting function, Eq. (6.12), is a good way to describe our data, we will now further test the monopole ansatz. One obvious way to do that is to try a general power-law and not constrain the fit to a monopole, i.e. use a function

$$F_\pi(Q^2, m_\pi^2) = \left(1 + \frac{Q^2}{p M^2(m_\pi^2)}\right)^{-p}, \qquad M^2(m_\pi^2) = c_0 + c_1 m_\pi^2\,, \tag{6.13}$$

with again an additional parameter p. A combined fit to our data sets results in $p = 1.182(59)$, now with a mass $M_{\rm phys} = 0.759(19)\,\text{GeV}$ and a χ^2/d.o.f. $= 0.541$. The exponent being close to one indicates that the monopole form is a good description. Taking the difference between this and the result of the fit to (6.12), we can assign a systematic error of $\Delta M_{\rm fit} = 32\,\text{MeV}$ on $M_{\rm phys}$ due to the ansatz for fitting the momentum dependence

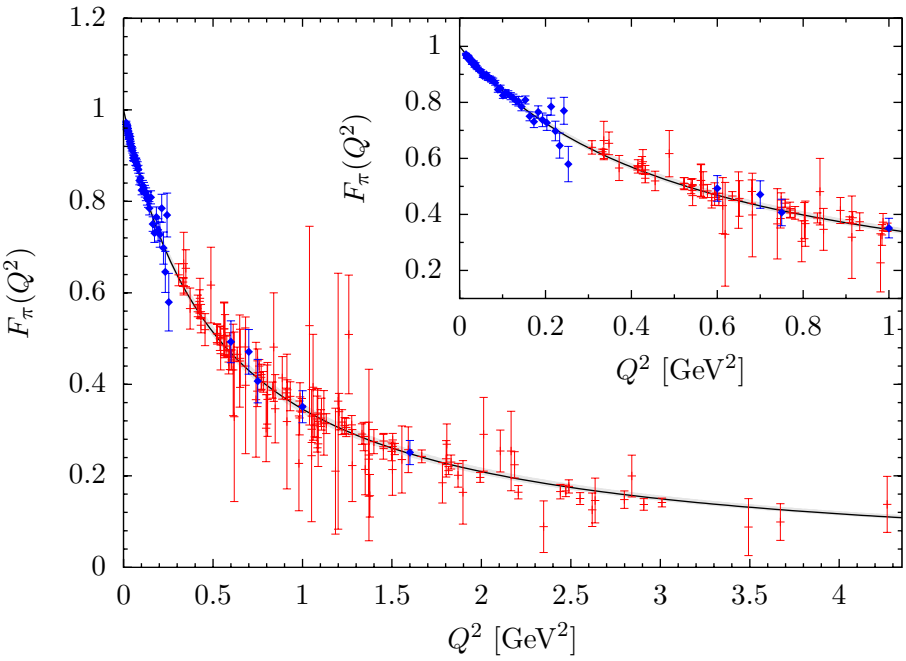

Figure 6.7 | Combined fit to all our lattices with its result at the physical pion mass. The lattice data is shifted as explained in the text. We have omitted data points for this plot with an error larger than 80% for better visibility. The points are however included in the fit.

(6.2). The validity of the fit over the whole Q^2 range is further tested by combined fits to Eq. (6.12) in a limited fitting range $Q^2 \leq Q^2_{\text{max}}$ or $Q^2_{\text{min}} \leq Q^2$. This is shown in Fig. 6.8, where we successively limit the fit to smaller (larger) momenta. Note that the increasing errors to the left or the right are due to the decrease in the number of fitted data points. Within these errors, the change in the monopole mass is consistent with statistical fluctuations. From this figure, the plot of the effective monopole masses, Fig. 6.4, and the combined fit of the general power-law, we can conclude that the monopole ansatz is a faithful description and works well in the entire region for which we have lattice data, from $Q^2 = 0$ to about $4\,\text{GeV}^2$.

6.6 Lattice Artifacts

Apart from taking the limit to the physical pion mass, there are two more limits remaining. One is the infinite volume limit concerning the box size of our lattice. The other is the continuum limit taking the lattice spacing a to zero. Those limits, although not less important, cannot always be taken since they require a large set of simulation parameters. Looking at the computational cost to remedy the two limits, one finds that they are naturally connected. Reducing the lattice spacing and therefore the discretisation errors increases the computational effort because at the same time it requires a larger number of lattice points to keep the physical volume. Increasing the volume can be done with a coarser lattice or again more computational effort for a larger number of lattice sites. The current study is one of the first attempting the investigation of lattice artifacts for the

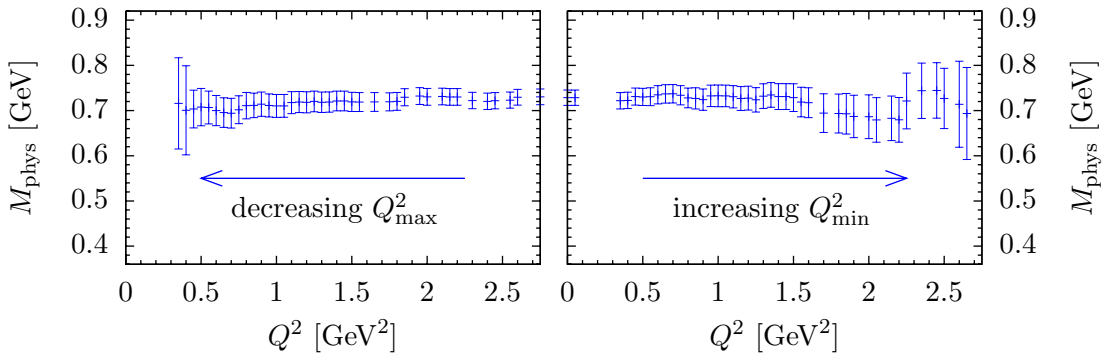

Figure 6.8 | Combined fits to (6.12) with reduced fitting ranges in Q^2. For the left plot Q^2_{max} is decreased, while Q^2_{min} is increased for the right plot. We use bins of 50 MeV^2 and show only points where the number of data points in the fit of F_π changed.

pion form factor for a dynamical simulation. However, due to the difficulties related to these limits we are only able to give estimates of the expected effects.

6.6.1 Finite Volume Effects

Since lattice simulations are confined to a space-time hypercube of $V_s \times T$ points with lattice spacing a, it is natural to investigate finite size effects. The typical spatial lattice volume is of the order of (2 fm)^3. To study the volume dependence of our results, we make use of two sets of configurations that have the same parameters β, κ for the lattice action but different volumes (see Table 6.4). We plot the monopole masses obtained for these lattices from Eq. (6.2) as a function of the lattice size $L = \sqrt[3]{V_s}$ in Fig. 6.9.a. The corresponding results are given in Tab. 6.4. We use the pion mass m_π and lattice spacing a determined for the lattice with the largest volume also for the smaller ones. From this figure, one could try to roughly read off a lattice size which should not suffer from finite size effects. This will clearly depend on the pion mass. Heavier pions should be affected less severely. Fig. 6.9.b gives an overview of our lattices in the m_π–L plane. Comparing Figs. 6.9.a and b, we can already estimate that most of our lattices should not suffer from strong finite size effects. Their lattice pion mass is either rather high or the physical size large enough. To obtain a somewhat better understanding of the volume dependence one may have recourse to chiral perturbation theory. The volume dependence of the pion charge radius has been investigated to one-loop order in various approaches of chiral perturbation theory [79, 80, 81]. In the continuum limit, the result of the lattice regularised calculation in [81] amounts to a finite size correction (in terms of the charge radius) of

$$\langle r^2 \rangle_L - \langle r^2 \rangle_\infty = \frac{3}{8\pi^2 f_\pi^2} \sum_{\boldsymbol{n} \neq \boldsymbol{0}} K_0(L m_\pi |\boldsymbol{n}|)\,, \tag{6.14}$$

where the sum runs over all three-vectors $\boldsymbol{n} \neq \boldsymbol{0}$ with integer components and $f_\pi \approx 92$ MeV is the pion decay constant. Note that the finite size correction of the charge radius is not proportional to m_π^2, unlike for other quantities such as the pion decay constant or the nucleon axial coupling. The leading contribution in Eq. (6.14) for large values of $m_\pi L$ is proportional to $K_0(m_\pi L) \sim \sqrt{\pi/(2m_\pi L)}\, e^{-m_\pi L}$. Unfortunately we cannot expect the

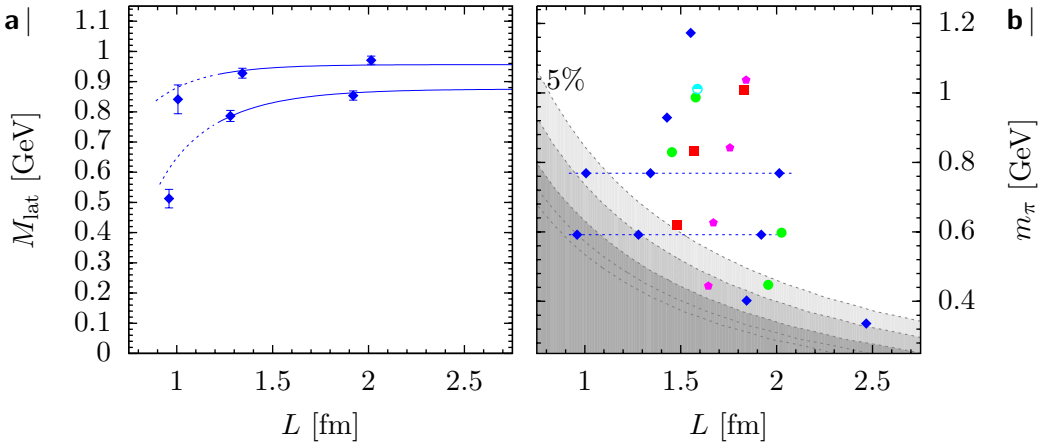

Figure 6.9 | **a** | Monopole mass vs. lattice size in our finite volume data sets with $\beta = 5.29$ and $\kappa = 0.1355$ (upper points) or $\kappa = 0.1359$ (lower points). The curves correspond to a fit to Eq. (6.15) as discussed in the text. **b** | Overview of pion masses and lattice sizes for our complete data set. The dashed horizontal lines mark our finite size runs. The dashed and shaded contours correspond to an estimated finite size shift (relative to the value in infinite volume) of 5%, 10%, 20%, 30%, and 40%, respectively.

results from chiral perturbation theory to be applicable at the pion masses and lattice volumes used for our finite size runs. For that, a dedicated run with pions of $m_\pi \lesssim 500\,\text{MeV}$ would be very desirable. The result (6.14) is also affected by this constraint. We take it, however, as a guide for the functional form of the volume dependence. We thus change the monopole mass in Eq. (6.12) to

$$M^2(m_\pi, L) = c_0 + c_1 m_\pi^2 + c_2\, e^{-m_\pi L}\,. \tag{6.15}$$

Taking the Bessel function $K_0(m_\pi L)$ instead of $e^{-m_\pi L}$ does not change our results significantly.

We then perform a combined fit to the data of all lattices in Table A.1 except for the lightest pion masses (lattice numbers 7, 13, 14, and 18) including in addition the $16^3 \times 32$ lattices of the finite volume runs (numbers 11a and 12a). We exclude the light pion masses,

Table 6.4 | Overview of our finite size runs. Note that we use the pion mass and lattice spacing of the largest lattice also for the smaller ones. They are given in Table A.1 and not repeated here. $M_{\rm lat}$ is as obtained from the monopole fit, $\Delta M_{\rm lat}$ is the estimated correction from the fit to Eq. (6.15)

β	κ	#	$N^3 \times T$	L [fm]	$m_\pi L$	$M_{\rm lat}$[GeV]	$\Delta M_{\rm lat}$[MeV]
5.29	0.13550	11	$24^3 \times 48$	2.0	7.8	0.967(15)	1.4
		11a	$16^3 \times 32$	1.3	5.2	0.932(17)	19.7
		11b	$12^3 \times 32$	1.0	3.9	0.839(51)	73.9
5.29	0.13590	12	$24^3 \times 48$	1.9	5.7	0.852(16)	12.6
		12a	$16^3 \times 32$	1.3	3.8	0.792(20)	90.2
		12b	$12^3 \times 32$	1.0	2.9	0.496(29)	262.7

since we cannot expect our ansatz for the volume dependence to be valid in this region. Our approximation required large values for $m_\pi L$ which is not fulfilled for the lightest masses. In addition, the biggest lever arm for the fit originates from our two finite size runs. These are performed at much higher pion masses of $m_\pi = 592\,\mathrm{MeV}$ and $m_\pi = 769\,\mathrm{MeV}$ (the horizontal dashed lines in Fig. 6.9.b). We thus do not expect our estimate to be reliable at much lighter pion masses. The result of the combined fit is represented by the solid lines in Fig. 6.9.a. The fitted parameters are $c_0 = 0.553(29)\,\mathrm{GeV}^2$, $c_1 = 0.612(35)$ and $c_2 = -6.97(1.71)\,\mathrm{GeV}^2$ at $\chi^2/\mathrm{d.o.f.} = 0.62$ which gives $M_{\mathrm{phys}} = 0.751(19)\,\mathrm{GeV}$ for the infinite volume limit of the monopole mass at the physical point. Compared with the value $0.727(17)\,\mathrm{GeV}$ obtained in the fit of Eq. (6.12) without volume dependence, this represents a moderate overall finite-size effect almost within the statistical errors. The fitted parameters do not change significantly if we only fit the $16^3 \times 32$ and $24^3 \times 48$ data sets of the finite volume runs, i.e. the data corresponding to the four rightmost points in Fig. 6.9.a (lattices number 11, 11a, 12, and 12a). We have not included the $12^3 \times 32$ lattices in the fit of Eq. (6.15) since we cannot expect our simple ansatz to hold down to lattice sizes of 1 fm (a similar argument as for the light pion masses). Qualitatively, our fit is not too bad even in this region, as shown by the dotted lines in Fig. 6.9.a. The estimated finite volume shift for each of our lattices, as calculated with the fitted parameters, is given in Tab. C.1. Figure 6.9.b also contains a contour corresponding to values of m_π and L which are expected to have a finite size shift $(M_\infty - M_L)/M_\infty$ of at least 5%. The lattices suffering from volume effects can thus be read off the figure. We note that this more or less only affects our lightest pion masses; the reason for excluding these data points from our discussion up to now. In order to use the information from these light pion masses, the estimated finite volume effect will be corrected for from now on. We will not stress these results too much, since our ansatz in Eq. (6.15) together with the fitted parameters is a crude estimate only. In addition, we also neglect the errors on the fit parameters, using only the central value of the shift. However, there is a first indication that this estimated shift is correct: a closer look at the shifted monopole masses of lattices #7 and #18 shows that these are now on top of each other, as visible in Fig. 6.12 or from Table C.1. This is encouraging since they have a different physical volume at almost identical pion mass.

As a final remark, we want to note that the finite volume, together with the discrete space-time symmetries of the lattice also introduce an additional contribution to the form factor. The matrix element is then no longer parametrised by F_π alone [80]. Whether this requires extra attention has to be checked.

6.6.2 Discretisation Errors

The scale dependence is the last limit we have to consider. Since we found in Sec. 6.3 that the $\mathcal{O}(a)$ effects for the vector current should be small, and since our lattice action is $\mathcal{O}(a)$ improved, the discretisation errors can be of $\mathcal{O}(a^2)$.

We investigate the scaling behaviour by extrapolating our values for the monopole mass to the physical pion mass separately for each β, as shown in Fig. 6.10. For that we again assume a linear relation between the squared monopole and pion masses. The extrapolated values are then studied as a function of the squared lattice spacing a, Fig. 6.11. Hereby, the lattice spacing is taken from r_0/a extrapolated to the chiral but not to the continuum limit. The respective values are given in Tab. A.2. They have been obtained as explained in [82]. The three rightmost data points in the plot of Fig. 6.11 strongly suggest that no

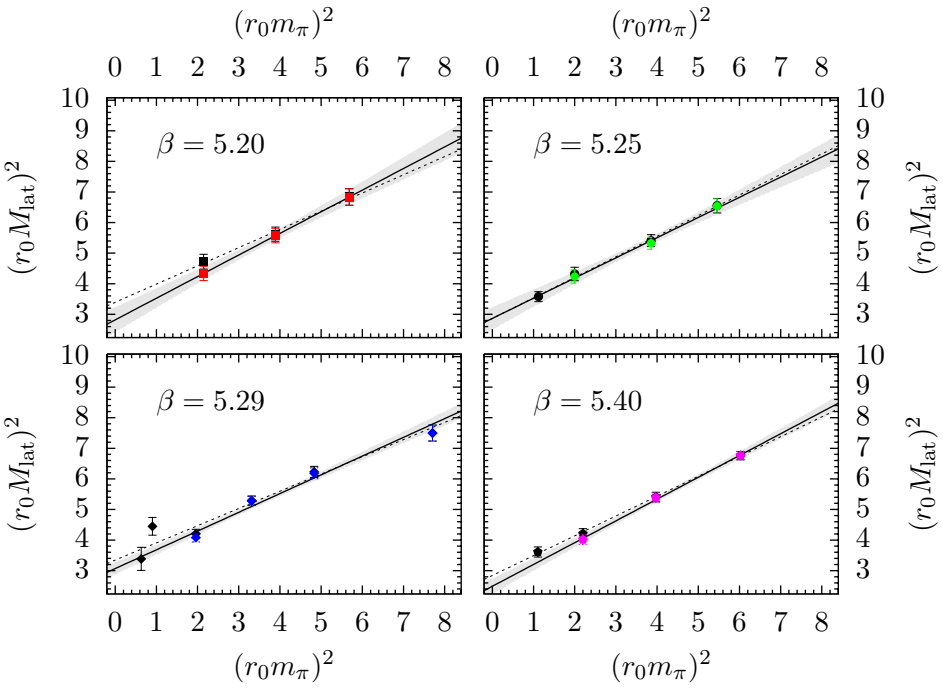

Figure 6.10 | Extrapolation of the monopole mass $M_{\rm lat}$ to the physical point, separately for each value of β. The black symbols together with the black dashed line includes also the lightest pion masses with the estimated finite size shift.

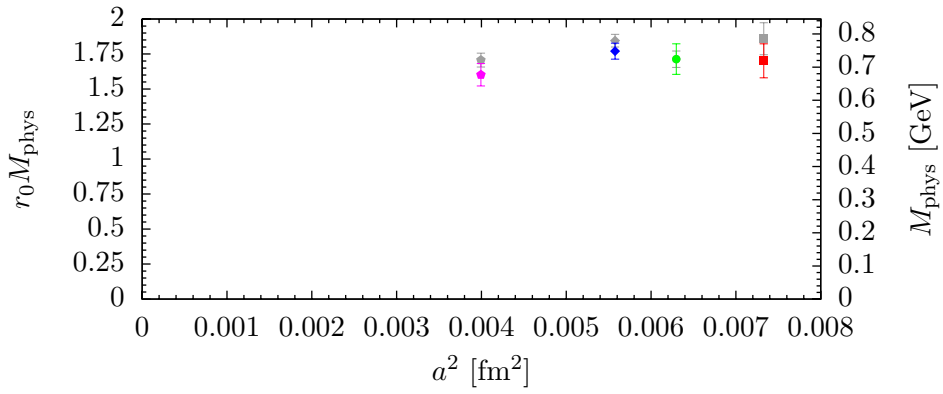

Figure 6.11 | Extrapolated values $M_{\rm phys}$ from Fig. 6.10 against the square of the lattice spacing. The points in light grey are obtained with our estimated finite volume correction.

discretisation errors are present within statistical errors. It requires additional simulation points to see if the leftmost data point represents a downwards trend or is just an out-lier.

Because we expect finite size effects for some of our lattices, we repeated the above mentioned procedure including our estimated volume correction. This correction is an upwards shift of the monopole masses by $c_2\, e^{-m_\pi L}$, where c_2 was taken from the global fit described in the previous section. The results are indicated in light grey in Fig. 6.11 and show an increase of M_{phys} mainly for $\beta = 5.20$ and 5.40 but is again consistent with no a dependence.

Given the lever arm in a^2 and the size of our statistical and finite size errors, we refrain from including an explicit a dependence of the monopole mass in our global fit to Eq. (6.12).

6.7 Comparison with Chiral Perturbation Theory

We come back to the extrapolation in the lattice pion mass now, picking up the discussion of Sec. 6.4. First, let us fit the monopole masses once again as we did for Fit 2 in Table 6.3, this time including the light pion masses with our estimated finite size correction (we neglect the uncertainty in this shift). The resulting monopole mass is $M_{\text{phys}} = 0.744(12)\,\text{GeV}$ with fit parameters $c_0 = 0.541(18)\,\text{GeV}^2$ and $c_1 = 0.632(27)$ displayed in Fig. 6.12. Based on the *assumption* that we can quantify the finite volume corrections, the light masses are thus consistent with our previous Fit 2 and still consistent with such a linear extrapolation.

Building up on this, a more sophisticated and at the same time more complicated approach to determine the m_π-behaviour of lattice data is the application of chiral perturbation theory (χPT). This is an effective field theory with pion fields as degrees of freedom, describing the low energy behaviour of QCD. It can provide us with the dependence on the pion mass starting from the chiral limit $m_\pi = 0$. This is opposite to lattice simulations, which usually start at rather large, unphysical pion masses and then get lower and lower during the simulation programme. This already provides a first hint that these two non-perturbative methods sometimes have to struggle to have sufficient overlap in their masses (see e.g. [83]). It is also unclear, what the range of applicability of χPT is. This can depend on the order of the chiral Lagrangian used and the observable in question. We thus use χPT only to extend our fits from Tab. 6.3 and mainly compare our data to χPT rather then perform stringent fits. The ultimate goal, fitting lattice data to χPT and extracting the emerging low energy constants (LECs) from that, still remains.

Different LECs appear in each order of the Lagrangians, with their number increasing order by order. Starting with the pion decay constant f_π at leading order, the next-to-leading order Lagrangian already has a total of ten LECs. They define the effective theory and have to be determined from theory or experiment since there is no a priori knowledge about them. Once known, the LECs are universal, i.e. they appear in the Lagrangian and do not depend on any specific physical process. However, different processes demand different combinations of LECs. The limited number of physical processes and their accuracy thus limits the number and reliability of known LECs.

So far, our discussion of the pion form factor was in terms of the monopole mass M. The calculations of χPT however, are directly for $F_\pi(Q^2)$ or the charge radius, which is connected to that via

$$\left\langle r^2 \right\rangle = -\left.\frac{\mathrm{d}F_\pi(Q^2)}{\mathrm{d}Q^2}\right|_{Q^2=0} \approx \frac{6}{M^2}\,. \qquad [1.9]$$

The authors of [84] have calculated the vector form factor of the pion to two loops in χPT. This represents a full $\mathcal{O}(p^6)$ next-to-next-to-leading order calculation. The contributions to this order are: Two-loop diagrams with vertices from the lowest order $\mathcal{O}(p^2)$ Lagrangian $\mathcal{L}_2$, one-loop diagrams with vertices from $\mathcal{L}_2$ and an additional vertex from $\mathcal{L}_4$, tree level diagrams with vertices from $\mathcal{L}_2$ and either two vertices from $\mathcal{L}_4$ or one from $\mathcal{L}_6$, the $\mathcal{O}(p^6)$ Lagrangian. Their result for the charge radius $\langle r^2 \rangle$ reads

$$\begin{aligned}\langle r^2 \rangle =& \frac{1}{f_\pi^2}\left(-6l_6^r - L - \frac{1}{N}\right) + \frac{m_\pi^2}{f_\pi^4}\Bigg[-3k_1 + \frac{3}{2}k_2 - \frac{1}{2}k_4 + 3k_6 - 12l_4^r l_6^r \\ &+ \frac{1}{N}\left(-2l_4^r + \frac{31}{6}L + \frac{13}{192} - \frac{181}{48N}\right) + 6r_{V1}^r\Bigg], \end{aligned} \tag{6.16}$$

where we have used the notation of [84]

$$N = 16\pi^2\,, \quad L = \frac{1}{N}\log\frac{m_\pi^2}{\mu^2}\,, \quad k_i = (4l_i^r - \gamma_i L)L\,. \tag{6.17}$$

Here, m_π is the pion mass used in χPT (so our lattice pion mass), f_π the pion decay constant. After $\overline{\text{MS}}$ subtraction, the coupling constants l_i from $\mathcal{L}_4$ are denoted by l_i^r [84]. They depend on the renormalisation scale μ and are related to their scale invariant counterparts $\bar{l}_i$ by

$$l_i^r = \frac{\gamma_i}{2N}(\bar{l}_i + NL)\,, \tag{6.18}$$

with the γ_i given by

$$\gamma_1 = \frac{1}{3}\,, \quad \gamma_2 = \frac{2}{3}\,, \quad \gamma_4 = 2\,, \quad \gamma_6 = -\frac{1}{3}\,. \tag{6.19}$$

We see in Eq. (6.16) that from the possible LECs appearing in $\mathcal{L}_4$ and $\mathcal{L}_6$, 'only' five survive. This can be reduced a little further, by inserting the one-loop result for f_π

$$f_\pi/f = 1 + \frac{m_\pi^2}{f_\pi^2}\,(l_4^r - L) \tag{6.20}$$

at the first order of Eq. (6.16). Here f is the pion decay constant in the chiral limit. Combining Eqs. (6.16) – (6.20) and using the renormalisation scale $\mu = m_\rho = 0.77\,\text{GeV}$, we obtain

$$\langle r^2 \rangle = \frac{c_1}{f^2}\left(\bar{l}_6 - 1 - L'\right) + \frac{m_\pi^2}{f^4}\left[c_2\tilde{r}_{V1} + c_3 + c_4 L' + (\bar{l}_2 - \bar{l}_1)(c_5 L' + c_6)\right]\,. \tag{6.21}$$

or, after using for the ratio $f_\pi/f = 1.069$ (again from [84]) and adding the value for $f_\pi = 93.2\,\text{MeV}$,

$$\langle r^2 \rangle = c_1'\left(\bar{l}_6 - 1 - L'\right)\text{GeV}^{-2} + m_\pi^2\left[c_2'\tilde{r}_{V1} + c_3' + c_4' L' + (\bar{l}_2 - \bar{l}_1)(c_5' L' + c_6')\right]\text{GeV}^{-4}\,. \tag{6.22}$$

The c_i and c_i' are pure numbers and are given in the appendix (see Table C.2), and $L' = \log(m_\pi^2/m_{\pi,\text{phys}}^2)$. Now only the LECs $\bar{l}_6$, $\bar{l}_2 - \bar{l}_1$ and $\tilde{r}_{V1}$ are left as parameters. We

want to note that the c_i' are all of the same order of magnitude, so none of the LECs is particularly suppressed. The constraints from phenomenological studies are [84, 85]:

$$\bar{l}_6 = 16.0 \pm 2\,, \quad \bar{l}_2 - \bar{l}_1 = 4.52 \pm 3.28\,. \tag{6.23}$$

The remaining LEC $\tilde{r}_{V1}$ is the least known and the authors estimate

$$\tilde{r}_{V1} \approx -6.234 \tag{6.24}$$

and assign a hundred percent error.

Another lattice study uses comparable ansatz to fit their data of the pion form factor [68]

$$\langle r^2 \rangle = c_0 \mathrm{GeV}^{-2} + c_1 m_\pi^2 \mathrm{GeV}^{-4} - \frac{1}{(4\pi f_\pi)^2} \left(L' + \log \frac{m_{\pi,\mathrm{phys}}^2}{\mu^2} \right), \tag{6.25}$$

with only two parameters c_0 and c_1. If we try to relate this equation to the above, we find that the number in front of L' is about a factor of five larger than in Eq. (6.22). With the given value of $\bar{l}_6$, the parameter c_0 should be approximately one. Furthermore, the fact that there are no factors of $m_\pi^2 L'$ amounts to $\bar{l}_2 - \bar{l}_1$ of roughly -1.6, which is not quite compatible with the phenomenological result. Using this and the above value for $\tilde{r}_{V1}$, the remaining parameter $c_1 \approx -3.5$ where the main contribution is due to $\tilde{r}_{V1}$.

After this introduction, we begin with fitting Eq. (6.25) to our lattice data. Here one ambiguity remains: the range of pion masses up to which the chiral equation is applicable is not known. We thus vary the range to check the effect of the pion mass on the fit, using three ranges given by the conglomerations of our lattice pion masses. The results are given in Table 6.5. The different fits are also plotted in Fig. 6.12. We observe that the fit range does not have a dramatic effect on the outcome of the fit when looking at the physical monopole mass. More remarkably even, within the fit range there is hardly a difference between the 'chiral' fit and the linear extrapolation and the fit range is nicely reflected by the behaviour of the curve. We prefer the fit up to $m_\pi^2 \sim 0.8\,\mathrm{GeV}^2$ between the two extremes of including too heavy pions and not having enough data points. As mentioned above, apart from the experience with other quantities there is no hint on the range where χPT is applicable. In addition to that, the four lightest data points are not reliable since the finite size effect is only estimated (and no uncertainty for that included). So including the intermediate pion masses certainly increases the attempted fit in that respect. On the other hand, a check that the fit does not rely on these data points is shown for Fit 4 in Table 6.5.

Table 6.5 | Fits to Eq. (6.25) with different ranges in the pion mass. We also provide the resulting monopole mass and pion charge radius.

#	range	c_0	c_1	χ^2/d.o.f.	M_{phys} [GeV]	$\langle r^2 \rangle$
1	0 – $1.2\,\mathrm{GeV}^2$	8.30(17)	-2.82(20)	1.85	0.747(6)	0.418(6)
2	0 – $0.8\,\mathrm{GeV}^2$	8.67(26)	-3.53(45)	2.02	0.735(8)	0.432(10)
3	0 – $0.5\,\mathrm{GeV}^2$	8.53(52)	-2.9(1.6)	2.79	0.740(16)	0.427(19)
4	$0.3\,\mathrm{GeV}^2$ – $0.8\,\mathrm{GeV}^2$	8.66(37)	-3.51(62)	1.20	0.736(12)	0.432(14)

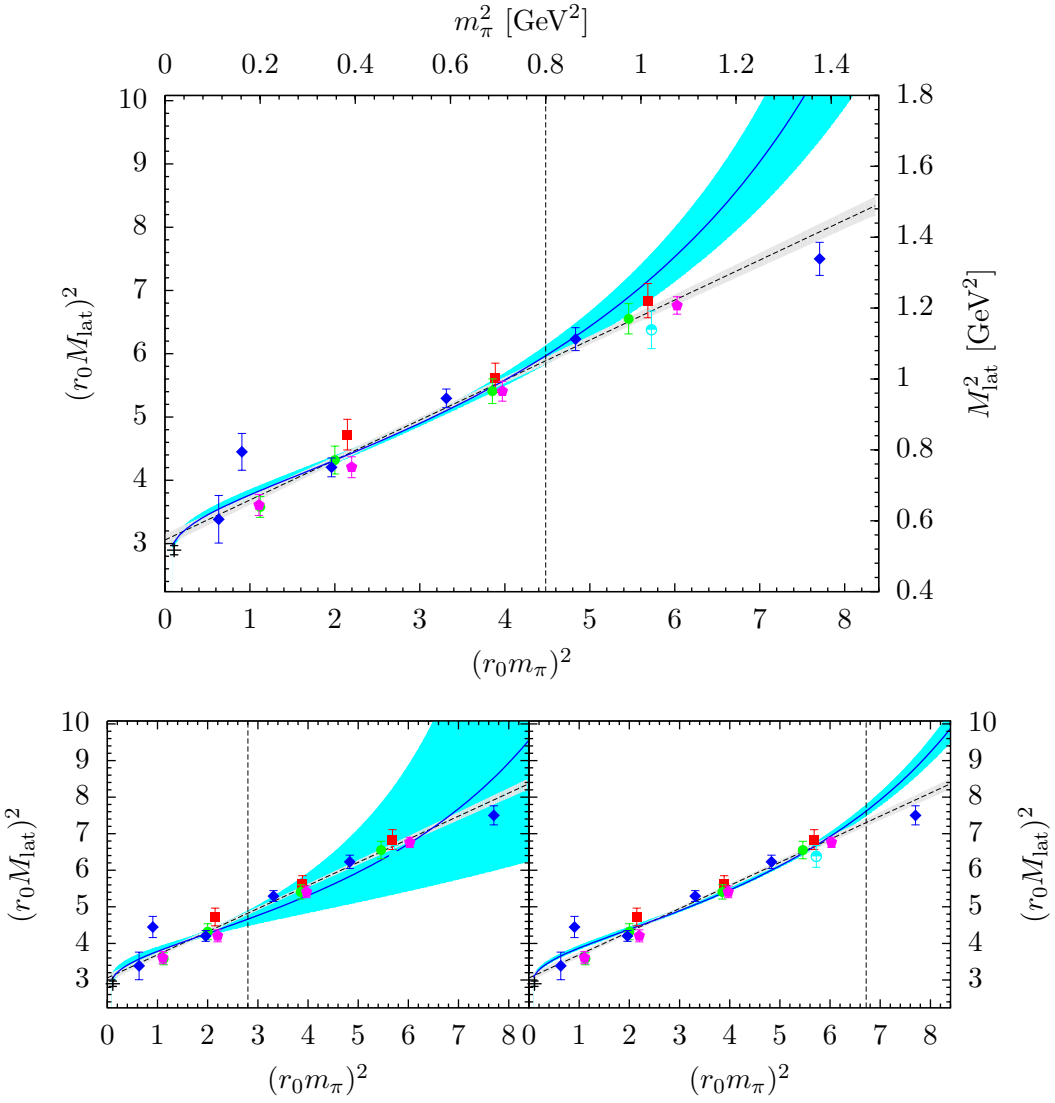

Figure 6.12 | Different attempts of a chiral extrapolation, this time including our lightest pion masses with their estimated finite size shift. The dashed black line is again a linear fit, as in Fig. 6.6. The solid blue line is a fit to Eq. (6.25) with the m_π fit range as indicated by the vertical dashed line. Note that the experimental point (black cross) is not included in the fit.

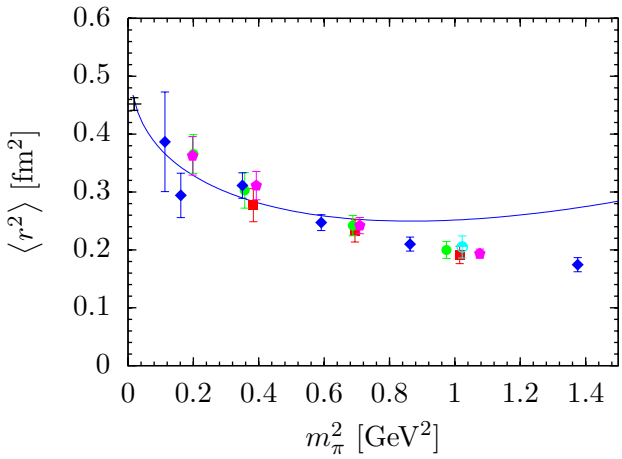

Figure 6.13 | This plot reveals the potential of finite volume corrected data and χPT. The solid blue line is the expected charge radius from Eq. (6.22) with LECs chosen within the phenomenological values, Eq. (6.26)

Next we consider the full two-loop result, Eq. (6.16), and start by a comparison to our data, based on the possible values of the LECs. The choice

$$\bar{l}_6 = 15.5\,, \quad \bar{l}_2 - \bar{l}_1 = 1.2\,, \quad \tilde{r}_{V1} = -2.2\,, \tag{6.26}$$

reveals the potential of χPT when lattice data is compared to it as shown in Fig. 6.13. The two-loop result comes close to our lattice data points for lower to intermediate pion masses. We use this as an indication for a possible fit range and as an encouragement to attempt a fit. The coupling constants obtained from the fits are given in Table 6.6. They compare remarkably good to their phenomenological values. For our favourite range of $m_\pi^2 < 0.8\,\mathrm{GeV}^2$, two of the LECs agree within errors. In general, $\bar{l}_6$ appears to be less problematic, since it defines the offset. Slope and curvature are harder to resemble. We found that the fit is also very dependent on the more or less unknown $\tilde{r}_{V1}$. This can also be attributed to the fact that the c_i' are all of the same order. We finally plot the results in Fig. 6.14. To make the non-linearity slightly more obvious, we now plot the charge radius instead of the square of the monopole mass. It should diverge for $m_\pi \to \infty$. For comparison, the 'best' fit (# 2) to Eq. (6.25) is also included in one of the figures. As we see, the fit for the shortest range in m_π^2 has the wrong curvature. This is most likely to the single out-lier. Although the other two fits look promising, we do not claim to extract

Table 6.6 | Fits to the full two-loop result, Eq. (6.22).

#	range	$\bar{l}_6$	$\bar{l}_2 - \bar{l}_1$	$\tilde{r}_{V1}$	χ^2/d.o.f.	$\langle r^2 \rangle$
1	$0 - 1.2\,\mathrm{GeV}^2$	15.5(7)	-0.3(7)	-2.3(3)	1.67	0.463(19)
2	$0 - 0.8\,\mathrm{GeV}^2$	14.7(1.3)	-1.6(1.9)	-1.9(5)	2.25	0.441(34)
3	$0 - 0.5\,\mathrm{GeV}^2$	7.4(5.2)	-18.1(12.3)	-0.6(1.0)	3.00	0.27(12)
phenom.		16.0(2.0)	4.52(3.28)	-6.234		0.452(11)

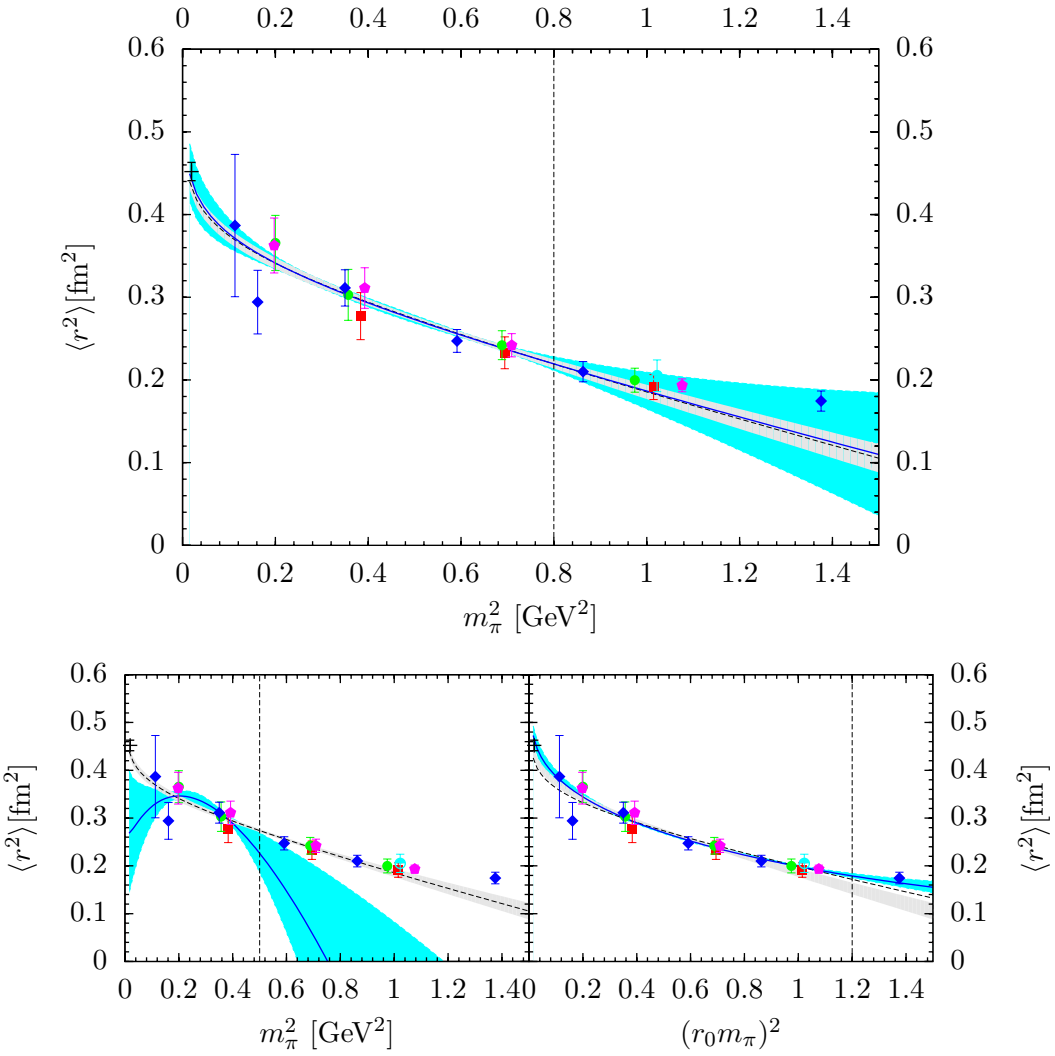

Figure 6.14 | Fits to the full two-loop χPT result for the charge radius, Eq. (6.22), shown as solid blue line. The vertical line again indicates the fit range, and we have included the data points for light pion masses with the estimated finite size shift. The dashed black line is the previous Fit 2 from Table 6.5. As before, the experimental point is not included in the fits.

the coupling constants of the chiral Lagrangian. The uncertainty in our data and the fit range is too high.

6.8 Conclusion

Using the monopole ansatz, Eq. (6.2), to describe the momentum dependence of the form factor, we linearly extrapolated the squared monopole mass against the square of the pion mass. This was focused on pion masses greater than 450 MeV because we can only

estimate the otherwise appearing finite size effects. We found that discretisation errors are small or absent, with a negligible effect from an improved vector current. Including estimates of systematic uncertainties, our final number for the monopole mass is $M = 0.727 \pm 0.017\,(\text{stat}) \pm 0.048\,(\text{syst}) + 0.024\,(\text{vol})\,\text{GeV}$, which translates to a charge radius of $\langle r^2 \rangle = 0.442 \pm 0.021\,(\text{stat}) \pm 0.058\,(\text{syst}) - 0.029\,(\text{vol})\ \text{fm}^2$. The first error is purely statistical, followed by a systematic uncertainty due to the ansatz for the fitting function and the extrapolation to physical pion masses (for which we added in quadrature the errors ΔM_{ext} and ΔM_{fit}). The last error reflects a possible shift because of finite volume effects.

In a next step, we included our lightest pion masses and shifted the central values for the corresponding monopole masses by the estimated finite size shift. Assuming the volume effect was correctly quantified, this leads to a consistent overall behaviour of our data points, supporting our results. However, for a thorough finite size analysis more simulation points and better analytic control is certainly required. The extrapolation based on χPT lead to $M = 0.728 \pm 0.028\,(\text{stat}) \pm 0.007\,(\text{syst})$ or $\langle r^2 \rangle = 0.441 \pm 0.034\,(\text{stat}) \pm 0.009\,(\text{syst})\ \text{fm}^2$. The systematic error being due to the two different extrapolations for our favourite range of pion masses only .

Contrasting our results with the experimental value of $M = 0.719(9)\,\text{GeV}$ and $\langle r^2 \rangle = 0.452(11)\ \text{fm}^2$, we find very good agreement. Other lattice results are given in Table 6.7.

Table 6.7 | An overview of lattice results for the pion charge radius along with the experimental value. We only quote results that are extrapolated to the physical point. The quoted lattice errors are purely statistical.

$\langle r^2 \rangle$ [fm^2]	type of result	Reference
0.452(11)	experimental value	PDG 2004 [77]
0.442(21)	Clover improved Wilson fermions, $N_f = 2$	this work
0.396(10)	Clover improved Wilson fermions, $N_f = 2$	JLQCD [68]
0.37(2)	Wilson fermions, quenched	[64]
0.37(5)	Domain Wall fermions, $N_f = 2 + 1$	[69]
0.351(8)		
0.310(46)	hybrid ASQTAD/DWF, $N_f = 2 + 1, 3$	LHPC [61]

7 Higher Moments of the Pion Structure

The pion form factor, discussed in the previous chapter, is the lowest Mellin moment as introduced in Section 2.7. Since we have computed operators with up to three lattice derivatives in our simulation, we can access the lowest four moments of the GPDs, following up the work started with [41]. These moments provide additional information about the structure of the particle, as explained in the introduction. We again consider the vector GPD of the pion here.

Computing matrix elements of operators with derivatives becomes notoriously difficult with the number of operators increasing. The signal extracted from the lattice then is more noisy, a disadvantage that is intensified when momenta are added. Hence our discussion begins with moments of forward matrix elements. Our discussion will follow the techniques applied in the previous chapter. The final result will be compared to the quenched study in [41], as well as phenomenological distribution functions obtained from experiments [86, 8].

The unprecedented study of higher moments of non-forward matrix elements is more involved and still limited to the second moment only. We discuss the available data and link to the phenomenological information contained in it.

7.1 Forward Moments

We have explained in Section 2.5 that the lattice is suited to calculate moments of GPDs. They are obtained by integrating the distribution functions (weighted with x^n) over the momentum fraction x carried by the (anti-)quarks. We recall the forward limit, in which the GPDs simplify to quark distribution functions

$$H_\pi^q \overset{\Delta\to 0}{=} \Theta(x)q(x) - \Theta(-x)\bar{q}(-x)\,, \tag{7.1}$$

where $q(x)$ is the PDF for quarks with flavour q. Taking moments thereof, we arrive at

$$\int_0^1 \mathrm{d}x\, x^n \left[q(x) - (-1)^n\, \bar{q}(x)\right]\,, \quad \text{for } n = 0, 1, 2, \ldots\,. \tag{7.2}$$

We see that we have flavour (non-) singlet moments for odd (even) n. They are related to the valence (n-even) and total (n-odd) quark distributions inside the pion. The first moment ($n = 0$) is counting the number of (valence) quarks minus anti-quarks of one flavour inside the pion. The second moment also has a straightforward interpretation: it corresponds to the momentum carried by the quarks of the probed flavour. Linking to the generalised form factors, the moments of the quark distributions are given by

$$\langle x^n \rangle = A_{n+1,0}(0) \tag{7.3}$$

where we have used Eq. (2.25a). Our calculation on the lattice makes use of the operators in Eq. (4.17a) with up to three derivatives. Evaluating these operators between pion states

of equal incoming and outgoing momenta we find

$$\left\langle \pi(\boldsymbol{p}) \right| \mathcal{O}_{\{\mu\mu_1\ldots\mu_n\}} \left| \pi(\boldsymbol{p}) \right\rangle = 2(\boldsymbol{p}_\mu \boldsymbol{p}_{\mu_1} \ldots \boldsymbol{p}_{\mu_n} - \text{traces})\, A_{n+1,0}(0)\,, \tag{7.4}$$

corresponding to the parametrisation in Eq. (2.22a). The explicit form of the operators is given in Appendix B. In order to stay consistent with [41], we keep the previous notation and denote them by $\mathcal{O}_{v2a}$, $\mathcal{O}_{v2b}$, $\mathcal{O}_{v3}$ and $\mathcal{O}_{v4}$ and limit ourself to one flavour.

Although the lowest four moments are not enough to reconstruct the quark distribution function by an inverse Mellin transformation, they still contain viable information. Based on existing parametrisations of the pion PDFs, one can try to arrive at a (model dependant) prediction from lattice QCD. However, [87] shows that this is difficult and has to rely on various assumptions. Difficulties here arise from unknown contributions of sea quarks and ambiguous extrapolations to the physical point. Furthermore, the parametrisations have at least three parameters already for the valence distributions (SMRS, [86]) which is hard to constrain with four moments (one being trivial) relating to total and valence quarks. Lattice data could however be used to add additional information to the PDF fits of experimental results, especially since there is usually less data in the low-x region. These phenomenological fits also suffer from the fact that experiments measure a convolution of pion and nucleon distribution functions. At the current stage we will only compare the lattice moments of quark distribution functions to moments obtained from phenomenological PDFs. Yet, this does not impair that we have a first principles, model free calculation of $\langle x \rangle$ for the pion.

7.1.1 Raw Lattice Data

Although we are looking at the forward case $\boldsymbol{q} = 0$ here, all operators considered require one unit of momentum for $\boldsymbol{p}$ due to the space-time components of the operators. The only exception is $\mathcal{O}_{v2b}$, which also has a signal for all spatial components of the momentum equal to zero. Parametrising the operator between pion states, this is easily read off Eq. (2.23a). We thus average over $\boldsymbol{p} = (1,0,0)$ and $\boldsymbol{p} = (0,1,0)$ when non-zero momentum is necessary, and extract $\boldsymbol{p} = (0,0,0)$ separately. We show the ratio $R(\tau)$ from Eq. (4.58) for one lattice and all operators in Fig. 7.1. For $\langle x \rangle$, where we have three possible operator/momentum combinations to choose from, the one with zero momentum naturally has the cleanest signal with the lowest error bars (top right panel). We determine the fit ranges individually for each data set and operator. The fits are then performed fully correlated, with errors obtained using the bootstrap method. Furthermore, we only use the axial-vector source to create and annihilate the pions. The lattice ratio is then matched to the continuum form including the kinematic pre-factors, Eqs. (4.59), (2.23a) and (2.26).

In order to convert the lattice ratios to physical matrix elements, we have to bear in mind the matching between the Euclidean and Minkowski formulation of the operators, Eq. (4.21a). We also need to apply an appropriate renormalisation. As explained in Section 4.2.1, the renormalisation procedure requires two steps: first, multiply with a renormalisation group invariant (RGI) renormalisation factor $Z_{\mathcal{O}}^{\text{RGI}}$ to convert the matrix elements into renormalised ones. Second, multiply with a factor $Z_{\mathcal{O}}^{\mathcal{S}',\,\mathcal{S}}(\mu',\mu)$ to change to the desired renormalisation scheme (in our case $\overline{\text{MS}}$). We give the results for all lattices and operators, already renormalised in the appendix in Table C.3 with the necessary renormalisation factors in Table C.4.

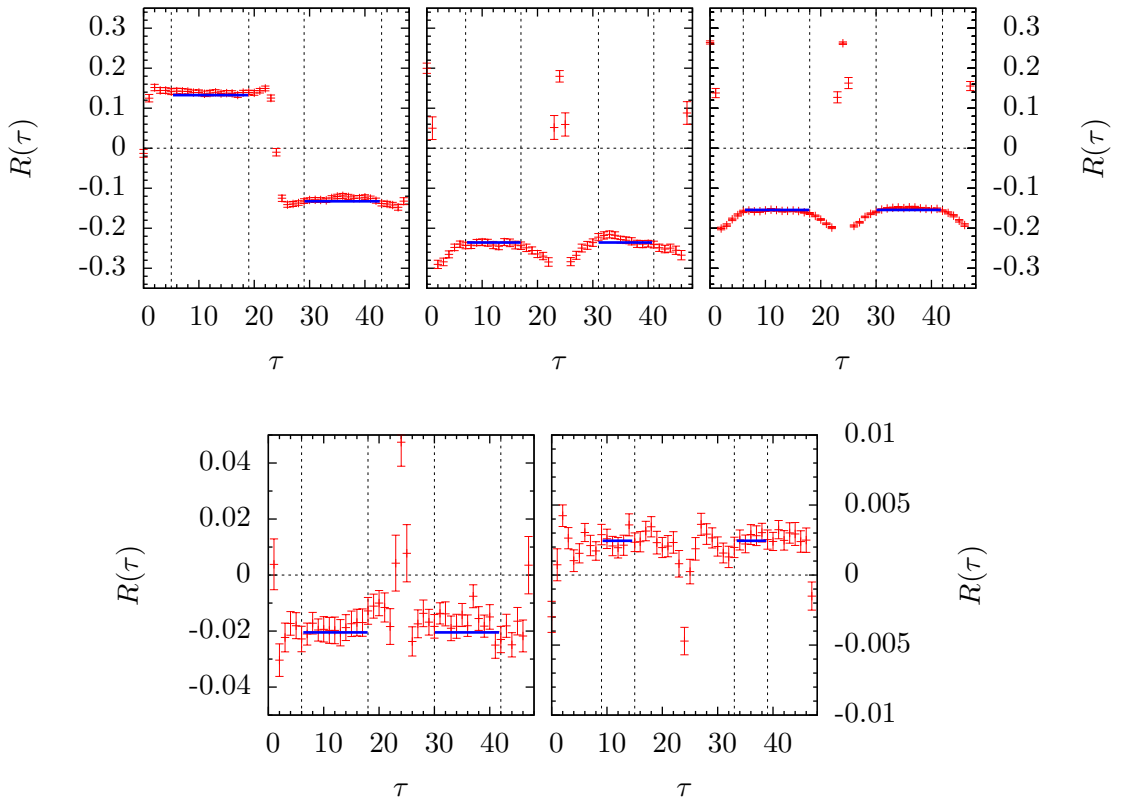

Figure 7.1 | The ratio of operators $\mathcal{O}_{v2a}$, $\mathcal{O}_{v2b}$ (with $\boldsymbol{p} \neq 0$ and $\boldsymbol{p} = 0$), $\mathcal{O}_{v3}$ and $\mathcal{O}_{v4}$ for lattice #16 (left to right, top to bottom). The vertical lines indicate the fit range we use. The obtained fit is shown by the solid blue line.

7.1.2 Operator improvement

Following the discussion of moments of nucleon structure functions in [44], we attempt to $\mathcal{O}(a)$ improve the operators $\mathcal{O}_{\mu\nu}$ which appear for $\langle x \rangle$. The additional terms to improve the current in this case are

$$\begin{aligned}\mathcal{O}^{\text{imp}}_{\mu\nu} =& (1 + am_{\text{q}}c_0)\mathcal{O}_{\mu\nu} + \sum_{i=1}^{3} ac_i \mathcal{O}^i_{\mu\nu} && [4.24]\\ =& (1 + am_{\text{q}}c_0)\bar{\psi}\,\gamma_\mu \overleftrightarrow{D}_\nu\,\psi \\ &+ ac_1 \left[\mathrm{i}\sum_\lambda \bar{\psi}\,\sigma_{\mu\lambda}\overleftrightarrow{D}_{[\nu}\overleftrightarrow{D}_{\lambda]}\,\psi\right] + ac_2\left[-\bar{\psi}\,\overleftrightarrow{D}_{\{\mu}\overleftrightarrow{D}_{\nu\}}\,\psi\right] && (7.5)\\ &+ ac_3\left[\mathrm{i}\sum_\lambda \partial_\lambda\left(\bar{\psi}\,\sigma_{\mu\lambda}\overleftrightarrow{D}_\nu\,\psi\right)\right].\end{aligned}$$

The operator in the last line, for $i = 3$, only contributes to non-forward matrix elements and we can hence drop it. We can further reduce the number of improvement terms for

on-shell matrix elements, where by using the equation of motion we can write c_0 and c_1 as a linear functions of c_2. As for the vector current in the previous chapter, there is no non-perturbative calculation of the improvement coefficients. So we have to resort to first order (tadpole improved) perturbation theory to obtain a relation between the improvement coefficients

$$c_0 = 1 - c_2 + \frac{4}{3}\frac{g_0^2/u_0^4}{16\pi^2}\left(\left\{\begin{array}{c} 17.20377 \\ 16.34500 \end{array}\right\} - \left\{\begin{array}{c} 8.69045 \\ 12.24534 \end{array}\right\} c_2\right) + \mathcal{O}(g_0^4)\,, \tag{7.6}$$

$$c_1 = c_2 + \mathcal{O}(g_0^2)\,, \tag{7.7}$$

where the upper (lower) numbers refer to $\mathcal{O}_{v2b}$ ($\mathcal{O}_{v2a}$) [45]. As in the nucleon case, we choose $c_2 = 0$. Experience tells us that the contributing operator for $i = 1$ is small. We checked that this is indeed the case for two lattices (numbers 12 and 16), where we found a signal from the ratio that is about an order of magnitude smaller than the value for $i = 0$. Our (perturbative) improvement is thus achieved by simply multiplying the original operator with $(1 + am_{\mathrm{q}}c_0)$. The effect of which ranges from below one to at most twelve percent for the individual lattices. The result in the chiral limit should not be affected because of the quark mass dependence of the correction.

Improving the operators for the higher moments is more complicated. The number of irrelevant operators increases, also with an additional covariant derivative. We will therefore not attempt to improve the operators for $\langle x^2 \rangle$ and $\langle x^3 \rangle$. This will only have an effect on the continuum extrapolation if the matrix elements of the irrelevant operators are not small, resulting in an extrapolation in a rather than a^2.

7.1.3 Volume Dependence

Before we continue with the extrapolation in the pion mass, let us take a short look at possible finite size effects. Anticipating the almost linear behaviour of $\langle x^n \rangle$ against the pion mass squared, we make an attempt of fitting a finite size behaviour analogous to the monopole masses in Eq. (6.15), i.e. we use

$$\langle x \rangle (m_\pi, L) = c_0 + c_1 m_\pi^2 + c_2 e^{-m_\pi L} \tag{7.8}$$

to check the volume dependence of our results. A similar ansatz was used in a finite size study of the ZeRo-Collaboration [88], where the authors find an effect on $\langle x \rangle$ for $m_\pi L \leq 5.5$ and pion masses around 300 MeV. This would affect lattices we already know to have finite size effects in case of the pion form factor, as well as other pionic observables like for example the decay constant f_π [59]. Another study of forward twist-two matrix elements of the nucleon in partially quenched heavy baryon chiral perturbation theory also predicts sizable corrections for the lattice data, if the box volume is too small [89]. With this expectation of finite size effects, we use our dedicated finite volume runs (lattices 11, 11a, 12, 12a) and two sets of lattices with roughly the same pion mass but different physical volume (lattices 2, 5, 16 at ≈ 830 MeV and 3, 17 at ≈ 620 MeV) as input for a fit to Eq. (7.8). The fit ansatz describes our data sets quite well, as shown in Fig. 7.2. We see from Table 7.1 that the biggest effect is observed for $\langle x \rangle$ based on the operator $\mathcal{O}_{v2b}$ with zero momentum. This matrix element has the best signal with the lowest statistical errors. This seems to be a plausible explanation why we see a clear finite size effect for this matrix element only. The higher moments even seem compatible with no volume effects,

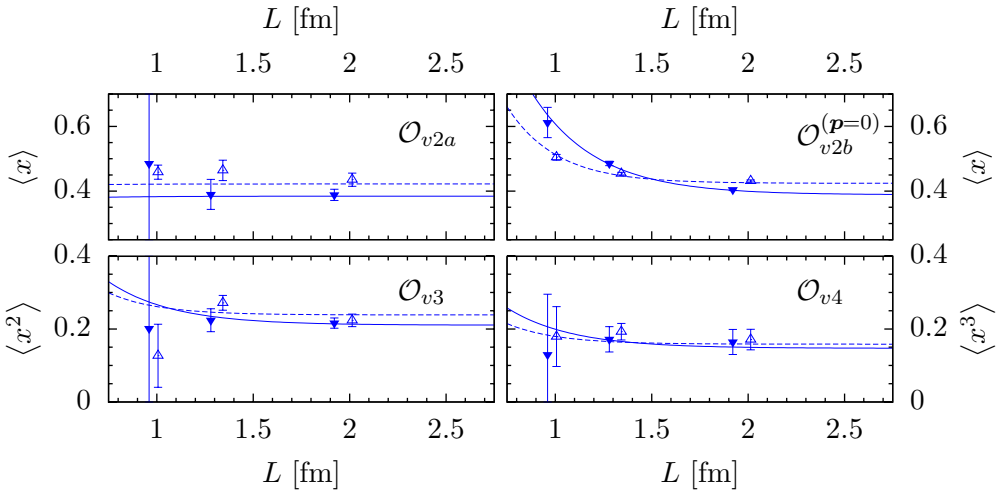

Figure 7.2 | Our attempts of fits to the finite size effects of $\langle x^n \rangle^{\mathrm{RGI}}$ are indicated by the lines. The lattices shown are: 11, 11a, 11b (open triangles pointing up, dashed line) and 12, 12a, 12b (triangles pointing down, solid line).

as suggested by the fitted parameters and Fig. 7.2. Although our data (also for the pion form factor) and the literature suggest corrections due to the finite box size, we do not have a reliable estimate to quantify the shift for the lattices that are concerned most, i.e. the four lightest pion masses. The reason for this is two-fold: first of all, our lattice results are not accurate enough, and the statistical uncertainties of the fitted parameters is certainly too big.[1] The data points for $m_\pi^2 \approx 0.2\,\mathrm{GeV}^2$ (lattices number 7 and 18) even agree within their errors although at different volumes (c.f. Fig. 7.3). Second, the chosen ansatz Eq. (7.8) can only be seen as a test for finite size effects. Even though an exponential $e^{-m_\pi L}$ with a polynomial in $1/L$ is a general behaviour for volume effects [80], our fits are made in a different regime of pion masses, where the effect is small.

Consequently, we do not include volume effects in the remainder. However, bearing in mind that our lightest pion masses are likely to suffer from these effects, we do not use the concerned data points for further fits. We will only show these in our plots for comparison.

[1] This was different for the pion form factor, where the effect is more pronounced and seems under better control. We stress again, that we still used it as an estimate only, and did not rely on the calculated shifts.

Table 7.1 | Finite size fits as described in the text. Fitting the dedicated finite volume lattices alone (11, 11a, 12, 12a) yields compatible results. Note that the matrix elements have been renormalised to RGI values but have not been taken to $\overline{\mathrm{MS}}$ for the fits.

	c_0	c_1 [GeV^{-2}]	c_2	χ^2/d.o.f.
$\mathcal{O}_{v2a}$	0.330(40)	0.156(62)	0.0(2.5)	1.14
$\mathcal{O}_{v2b}^{(\boldsymbol{p}=0)}$	0.337(6)	0.147(10)	4.40(37)	2.46
$\mathcal{O}_{v3}$	0.170(31)	0.116(47)	1.1(1.7)	0.65
$\mathcal{O}_{v4}$	0.131(61)	0.047(90)	1.1(2.3)	1.27

7.1.4 Extrapolations in Pion Mass

The extrapolation to the physical pion mass is again a crucial point of the analysis. Using predictions from one-loop chiral perturbation theory, taken from [90, 91], we know that the even and odd moments of the quark distributions should extrapolate differently. For the forward moments of the pion quark distributions, we expect[2]

$$\langle x^n \rangle (m_\pi^2) = \begin{cases} c_0^{(n)} \left(1 - \frac{m_\pi^2}{(4\pi f_\pi)^2} \log \frac{m_\pi^2}{\mu^2}\right) + c_1^{(n)} m_\pi^2 & \text{for even } n, \\ c_0^{(n)} + c_1^{(n)} m_\pi^2 & \text{for odd } n, \end{cases} \tag{7.9}$$

with corrections of $\mathcal{O}(m_\pi^4)$ and the $c_i^{(n)}$ corresponding to LECs. The two cases also have a different physical interpretation. Odd moments relate to the total (valence + sea) distribution of quarks and anti-quarks in the pion. It is also for the odd moments, where our lattice calculation omits possibly occurring disconnected contributions, see Section 4.3. So despite the simpler extrapolation to the physical pion mass, we nevertheless have an uncertainty due to the disconnected fermion lines. Even moments on the other hand describe the distribution of valence quarks since the contribution from sea quarks and anti-quarks cancel when taking the difference, Eq. (7.2). Looking at the lattice data (Fig. 7.3), we see no indication for the presence of chiral logarithms. This observation is somewhat blurred, because we are likely to be confronted with finite size effects for our lightest pion masses. Judging from Fig. 7.2 and the theoretical predictions, the finite volume shift should lower $\langle x^n \rangle$ for our small pion masses. Since we cannot quantify this shift, the four lightest pion masses are excluded from any fits (lattices 7, 13, 14, 18). Consequently, our lattice data is well fit by a linear function in m_π^2 for the remaining region. We hence use only one ansatz for the even and odd moments to extrapolate to the physical pion mass,

$$\langle x^n \rangle (m_\pi^2) = c_0^{(n)} + c_1^{(n)} m_\pi^2 \,, \tag{7.10}$$

with the caveat that we do not include chiral logs. Fits of this linear behaviour in m_π^2 are shown in Fig. 7.3 for all of our operator combinations. The fitted parameters are given in Table 7.2. We note that the three values for $\langle x \rangle$ agree nicely within errors. As already mentioned above, $\mathcal{O}_{v2b}(\boldsymbol{p} = 0)$ has the cleanest signal.

[2] Note our different counting for $\langle x \rangle$ and $A_{n,i}$, see Eq. (7.3), so even and odd cases are switched with respect to the reference.

Table 7.2 | The fit parameters to the extrapolation of the lattice moments, Eq. (7.10), for RGI matrix elements. The last row is the value of $\langle x^n \rangle$ at the physical pion mass in the $\overline{\text{MS}}$ scheme at $\mu = 2\,\text{GeV}$ (with statistical errors from the fit, as well as systematic uncertainties for the renormalisation).

	$\mathcal{O}_{v2a}$	$\mathcal{O}_{v2b}^{(\boldsymbol{p}=0)}$	$\mathcal{O}_{v2b}^{(\boldsymbol{p}\neq 0)}$	$\mathcal{O}_{v3}$	$\mathcal{O}_{v4}$
$c_0^{(n)}$	0.363(16)	0.377(2)	0.375(4)	0.218(11)	0.146(18)
$c_1^{(n)}$ [GeV^{-2}]	0.089(18)	0.094(2)	0.094(4)	0.029(11)	0.015(18)
χ^2/d.o.f.	0.72	14.72	4.96	0.68	0.61
$\langle x^n \rangle_{\text{phys}}^{\overline{\text{MS}}}$	0.261(11)(10)	0.271(2)(10)	0.270(3)(10)	0.128(6)(5)	0.074(9)(4)

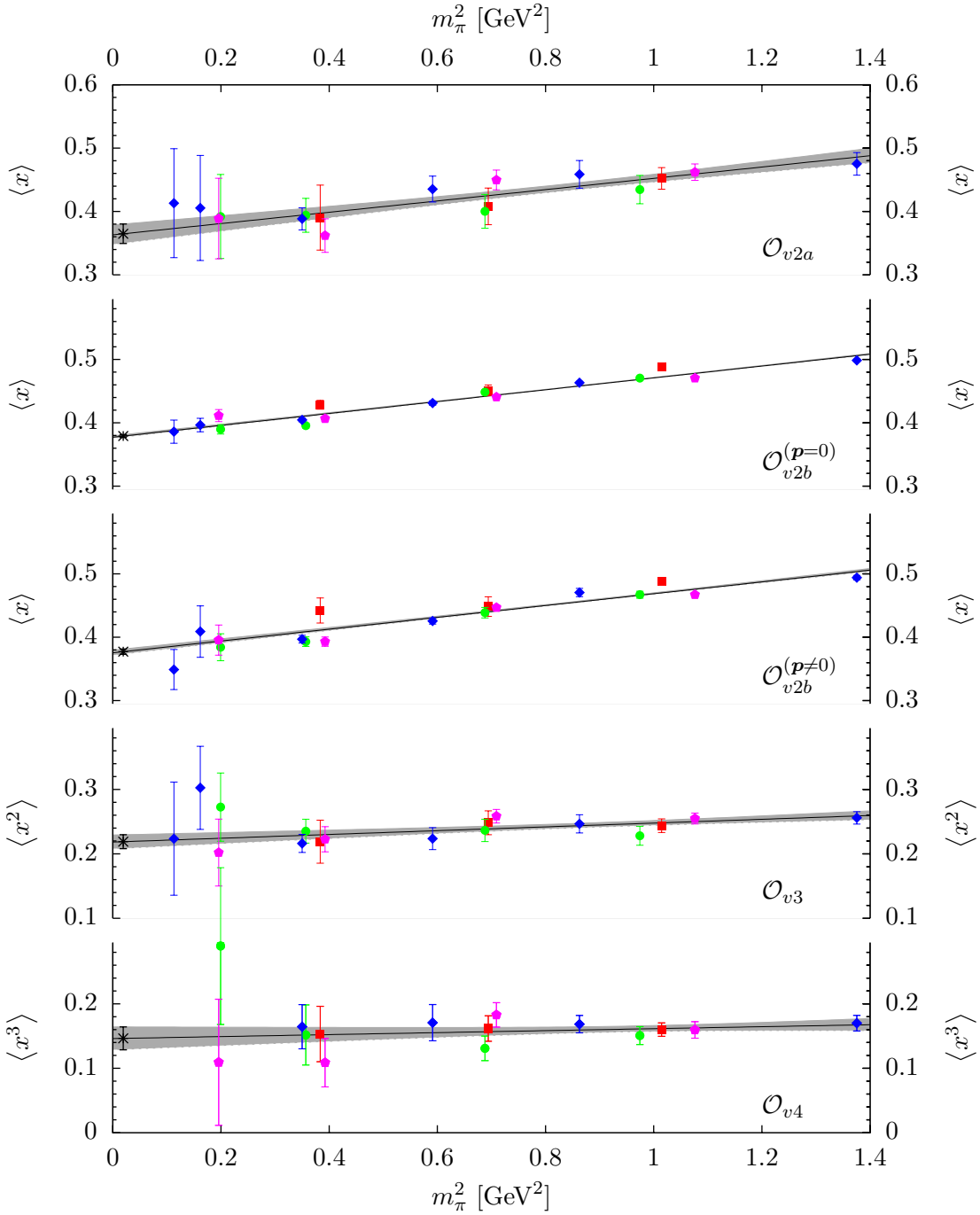

Figure 7.3 | This figure shows our results for $\langle x^n \rangle^{\mathrm{RGI}}$ for $n = 1, 2, 3$ with the three possible operator/momentum combinations for the second moment at the *top*. The solid lines with error bands correspond to our extrapolation to the physical pion mass (indicated by a cross). The lowest pion masses are not included in the fit. Chiral perturbation theory predicts a logarithmic behaviour for the even moments, which is absent in our data. Note, however, that unknown finite size effects could have an effect.

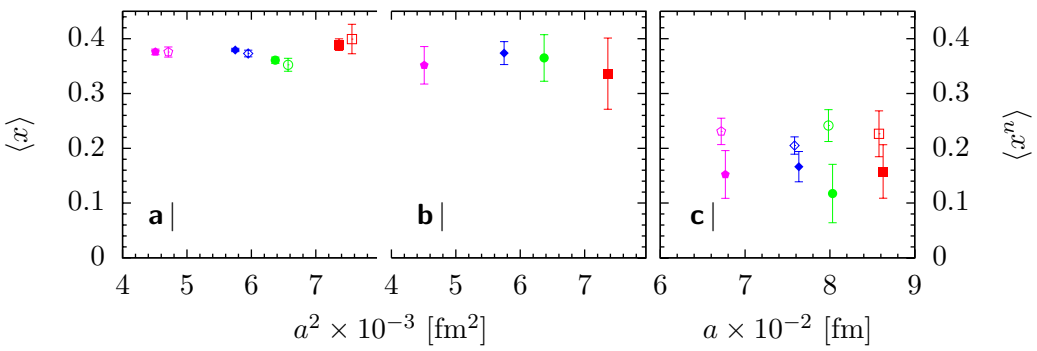

Figure 7.4 | These figures shows our results for $\langle x^n \rangle^{\mathrm{RGI}}$ in the chiral limit, but for the different β values and their corresponding lattice spacing. Overall, we observe no clear dependence on the lattice spacing. **a** | is for $\mathcal{O}_{v2b}\,(\boldsymbol{p}=0)$ (*closed* symbols) and $\mathcal{O}_{v2b}\,(\boldsymbol{p}\neq 0)$ (*open* symbols, with offset), both agree very nicely as before. **b** | $\mathcal{O}_{v2a}\,(\boldsymbol{p}\neq 0)$. **c** | $\mathcal{O}_{v3}$ (*open* symbols) and $\mathcal{O}_{v4}$ (*closed* symbols, with offset), note the different abscissa.

7.1.5 Scaling Violations

Similar as for the pion form factor, we will now test our results for discretisation errors originating in the finite lattice spacing. In case of the second moment $\langle x \rangle$, we also have an additional check. We use operators that transform under different irreducible representations of the hypercubic group. So while their continuum results should be identical, we can expect dissimilar lattice artefacts. Let us start by first considering $\mathcal{O}_{v2b}$ for both, vanishing and non-vanishing momenta. Figure 7.4.a shows the extrapolated values for our four β values, taken at $m_\pi = 0$ for simplicity. We have again used the values r_0/a in the chiral limit, Table A.2. Since we have tried to (perturbatively) improve the underlying operators, we plot $\langle x \rangle$ against a^2 assuming $\mathcal{O}(a^2)$ errors. The plot seems to suggest a downward trend for the continuum limit. Fitting a quadratic behaviour in a instead finds a increase for $\langle x \rangle$ in both cases for the operator $\mathcal{O}_{v2b}$ (c.f. Table C.5). However, the error in the fitted slope with respect to a^2 is at least 200% in the fits, so the data points provide no clear handle on the extrapolation. The corresponding results for the operator $\mathcal{O}_{v2a}$ are shown in Fig. 7.4.b. Here, the larger errors make the investigation of scaling effects even more difficult. A linear fit with respect to a^2 now finds a decrease towards the continuum limit where the extrapolated value has an error of $\approx 30\%$. While this could be interpreted as a qualitatively different behaviour for the operators $\mathcal{O}_{v2a}$ and $\mathcal{O}_{v2b}$, the errors on the fitted slopes are too large and a conjecture is not justified.

Since the errors for the moments $\langle x^2 \rangle$ and $\langle x^3 \rangle$ are of similar size as for results from $\mathcal{O}_{v2a}$, the investigation of scaling effects shows similar inconclusive behaviour. The data points are shown in Fig. 7.4.c. Because we did not include any improvement we treat those as having $\mathcal{O}(a)$ errors. The pion mass-extrapolated values for all operators and β values are given in Table C.5, the fits to a constant or linear dependence on a^2 (and a) can be found in Table C.6.

Since the statistical errors for the individual $\langle x^n \rangle$ do not allow for a clear conclusion, our final numbers for the moments of the quark distributions will assume a flat extrapolation to the continuum limit. We thus stick to the global fit of the chiral extrapolation in Eq. (7.10). The results from these global fits agree with the constants fitted to the β dependent values

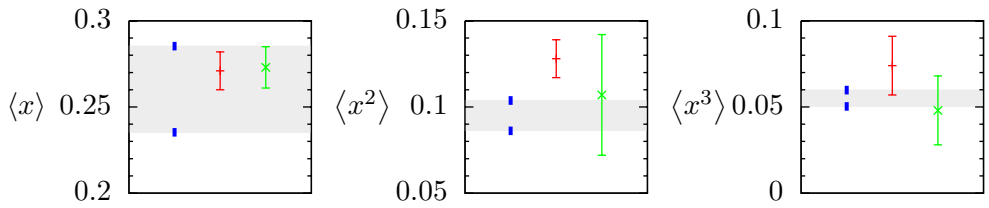

Figure 7.5 | Comparison of $\langle x^n \rangle$ in $\overline{\text{MS}}$ of the present results (*middle* points, $\mu = 2\,\text{GeV}$), quenched results from [41] (*right* points, $\mu \approx 2.4\,\text{GeV}$) and phenomenological values from PDFs (*left* points and band). The latter are obtained from [86] (*upper* value, $\mu = 2\,\text{GeV}$) and [8] (*lower* value, $\mu = 2\,\text{GeV}$).

given in Table C.6. The difference to the central values from the alternative linear fits will be included as systematic error of the continuum limit.

7.1.6 Discussion of the Results

Collecting the above results for the moments of the quark distributions, we have

$$\langle x \rangle = 0.271(2)(4)(10)\,, \quad \langle x^2 \rangle = 0.128(6)(7)(5)\,, \quad \langle x^3 \rangle = 0.074(9)(14)(4)\,,$$

in the $\overline{\text{MS}}$ scheme for $\mu = 2\,\text{GeV}$. The first error being statistical, followed by systematic uncertainties from the continuum limit and renormalisation. Not included is an uncertainty due to volume effects which is certainly necessary for a sound prediction from first principles. Leaving aside finite size corrections, drawing conclusions from the lattice data is still not straightforward. The odd moments, which have an unambiguous extrapolation to the physical pion mass, omit contributions from disconnected fermion lines. They relate to the total quark distribution that is difficult to measure in experiments. Neglecting that, we find from $\langle x \rangle$ that the light quarks inside the pion carry roughly 54% of its momentum. The remaining 46% have to be attributed to the other quark generations and the gluons. The even moments, on the other hand, have a simple interpretation in form of the valence distributions. However, the correct chiral extrapolation cannot be achieved yet.

Let us compare our results to the ones from the quenched calculation in [41]. Those were obtained at a slightly different scale, and with perturbatively renormalised values. As we see from Fig. 7.5, there is good agreement between the two sets of results. We were able to improve on the errors (bearing in mind that we plotted statistical and systematic errors, added in quadrature), while there is no indication for quenching effects.

A comparison to phenomenological values is more difficult. There exist different parametrisation of PDFs, certainly leaving some room for uncertainties. The biggest insecurity for the PDFs obtained from experiments is the contribution from sea quarks, which cannot be measured directly. Looking again at Fig. 7.5, we find that the agreement is quite reasonable (we have included total and valence distributions accordingly). More reliable and additional lattice data points for our lowest pion masses will improve the situation. The chiral extrapolation should finally decrease the results slightly, better control over finite size effects contributing its part. To which extent the disconnected contributions plague our results is not clear, since the second moment, that is free of this problem, does not stick out. We refrain from fitting the parameters of the PDFs to our data, because we can only extract one valence distribution without further assumptions.

7.2 The Second Off-forward Moment

We now turn to the discussion of the second moment of the vector GPD in the non-forward case. We recall its form

$$\int \mathrm{d}x\, x H_\pi^q(x,\xi,t) = A_{2,0}(\Delta^2) + (-2\xi)^2\, A_{2,2}(\Delta^2)\,, \qquad [2.25a]$$

with the matrix element we calculate on the lattice given by

$$\left\langle \pi(\boldsymbol{p}')\right| \bar{\psi}(0)\, \gamma_{\{\mu} \mathrm{i}\overleftrightarrow{D}_{\nu\}}\, \psi(0) \left|\pi(\boldsymbol{p})\right\rangle = 2P_{\{\mu}P_{\nu\}} A_{2,0}(\Delta^2) + 2\Delta_{\{\mu}\Delta_{\nu\}} A_{2,2}(\Delta^2)\,. \qquad (7.11)$$

This parametrisation is matched against the lattice ratio $R(\tau)$, Eqs. (4.59) and (4.60). This is done in a completely analogous way as for the pion form factor. The only difference is the slightly more complicated parametrisation on the continuum side and the additional derivative for our lattice results. We use our large set of momenta for $\boldsymbol{p}$ and $\boldsymbol{q}$, c.f. Eq. (6.1). The additional momenta with components in every direction make it possible to also use more operator combinations in contrast to the forward case. These operators are included in App. B. In consequence of the large basis of operators and momenta, we again arrive at an over-constrained fit to the two generalised form factors $A_{2,0}$ and $A_{2,2}$. Our statistical errors rely on a Jackkife analysis of our configurations.

7.2.1 Momentum dependence

The non-forward matrix elements require a fit to the momentum dependence with respect to Δ^2. The basic form will be the p-pole that was already discussed in Sec. 6.5. It has been found for the nucleon that the different moments follow p-pole fits with different exponents p. To check for a preference in data, we thus start by fitting

$$A_{2,i}(\Delta^2) = A_{2,i}(0) \left(1 - \frac{\Delta^2}{p_i\, M_{i,\mathrm{lat}}^2}\right)^{-p_i}, \quad \text{for } i = 0, 2 \qquad (7.12)$$

to the extracted data points individually for each of our lattices. Here a pole mass M_i and the exponent p_i occur. The value for $A_{2,0}(0)$ should then match our results from the forward matrix elements $\langle x\rangle$ in the previous section. The results to the fits are given in Table C.7, with one example shown in Fig. 7.6. In contrast to Sec. 6.5, the fit is not combining all lattices. Hence the individual p_i scatter quite a bit and have larger error bars. We nevertheless observe a tendency for $p_0 \lesssim 1$ on average and will assume a monopole as for the form factor in the following. Corresponding fits with $p_0 = 1$ are also included in Table C.7 and show that the obtained χ^2/d.o.f. does not favour a free pole over the monopole. The error bars of our data are to large to really narrow the choice of an exponent p_0. The situation for p_2 is somewhat different because our values for $A_{2,2}(\Delta^2)$ are considerably closer to zero, even compatible with zero within the statistical significance of the data. The absence of a forward value $A_{2,2}(0)$ (which only exists as a limit $\Delta^2 \to 0$ in the continuum case) worsens the situation. The fits favour very small pole masses M_2 and small values for p_2. Restricting ourselves to integral numbers for the exponent and thus again using a monopole form is however not excluded by looking at the χ^2. The actual fitted parameters provide a good description of the data, see Fig. 7.6.

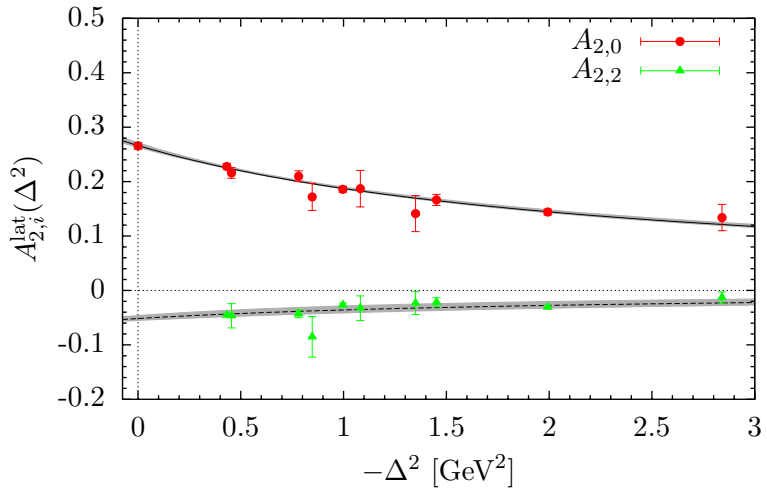

Figure 7.6 | An example for $A_{2,i}(\Delta^2)$ for lattice #16 including fits to a monopole form. Note the different sign and the absence of a forward value for $i = 2$.

While we use a monopole ansatz for our discussion in following, a different behaviour might be considered in view of generalised transversity distributions [25]. The requirement of non-divergent, well behaved distributions narrows the choice for the pole form as in motivating lower bounds on $p_0 > 1$ and $p_2 > 2$. We note that the lattice data is not sensitive against the exponent p. A dipole yields a similar description. The change in χ^2 is very small and the norm $A_{2,i}(0)$ does not change significantly (if the values change, the shift is clearly within the one-σ error).

We plot the extracted monopole masses and the renormalised (RGI) values for $A_{2,i}(0)$ in Fig. 7.7. We again observe an almost linear behaviour in m_π^2. Due to the improvement applied to operators for $\langle x \rangle$ in the previous section, $A_{2,0}(0)$ has to agree only in the chiral limit, so we postpone a comparison until later. Instead, we can test if our results are consistent with the so-called soft pion theorem, known for example from chiral perturbation theory, [90]. It is given by

$$A_{2,0}(0) = -4A_{2,2}(0) + \mathcal{O}(m_\pi^2)\,. \tag{7.13}$$

To see whether this relation holds, we plot both results $A_{2,i}(0)$ again in Fig. 7.8 and find rather good agreement within our statistical errors. Note, however, that this is just a test and relies on the assumption that lattice artifacts have a similar effect on both forward values so that they can be neglected.

7.2.2 Effects of the Finite Volume

As for our previous observables, we continue with the investigation of finite size effects. We do this independently for the forward limit (the norm of the fitting ansatz) and the monopole mass. Since our values for $A_{2,i}(0)$ show a similar, inconclusive picture that we found in Sec. 7.1.3, we will not further discuss them here. We resort to our empirical ansatz, Eq. (6.15), for the monopole masses M_i, and include this in a combined fit to our lattices. The monopole masses for our dedicated finite size runs are shown in Figs. 7.9 and 7.10. The fits of the finite volume ansatz to $M_{0,\text{lat}}$ are done for the finite volume runs and lattices

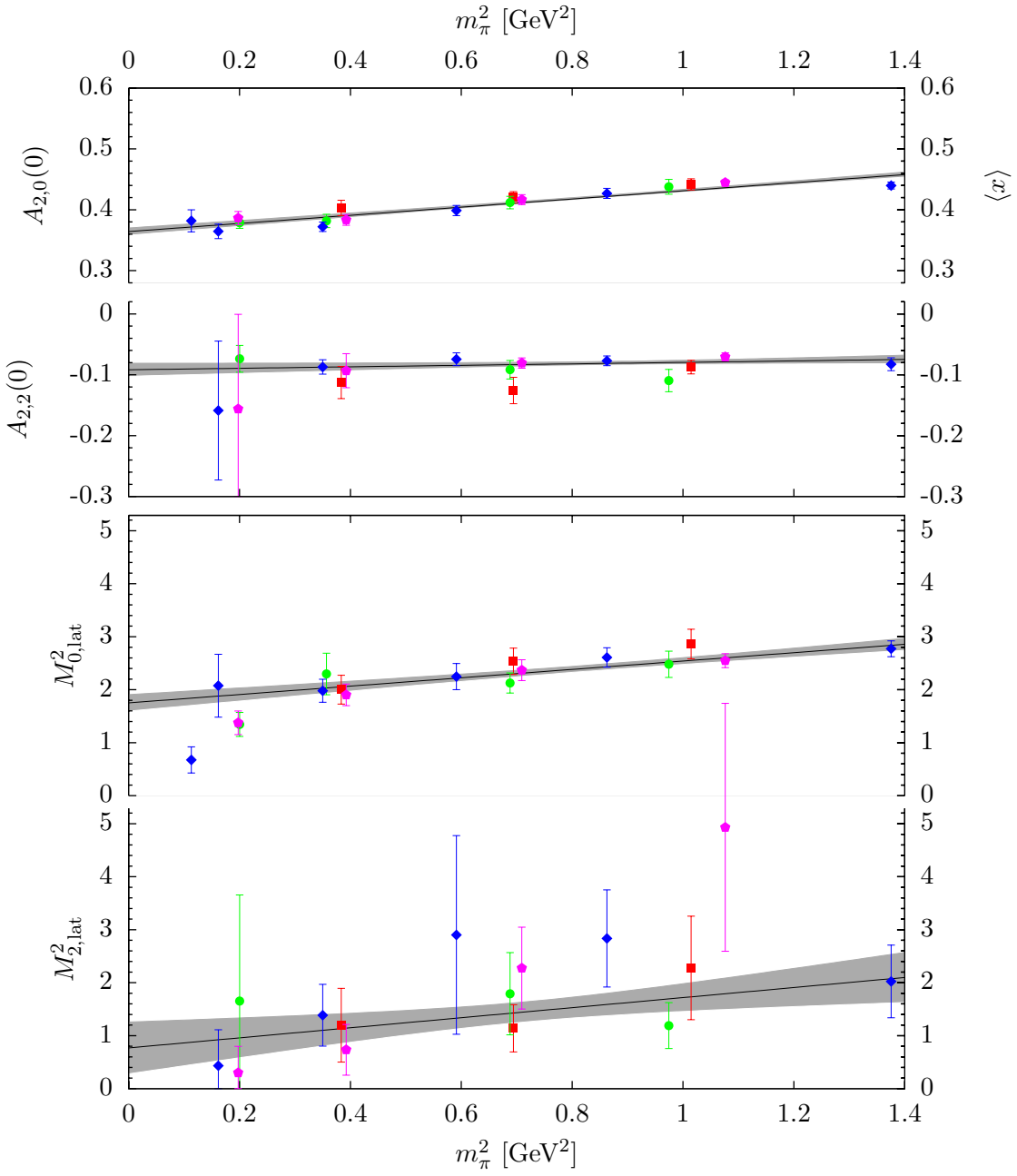

Figure 7.7 | These plots show the pion mass dependence of the forward limit of the two GFFs $A_{2,i}$ (*top*) and the monopole mass extracted from Eq. (7.12) (*bottom*). The solid lines and error bands correspond to fits ($m_\pi^2 > 0.3\,\mathrm{GeV}^2$) as discussed in Sec. 7.2.3.

with $m_\pi^2 > 0.3\,\mathrm{GeV}^2$. The parameters we find are $c_0 = 1.97(13)\,\mathrm{GeV}^2$ which corresponds to an extrapolated squared mass, $c_1 = 0.66(14)$ (the slope of the extrapolation) and $c_2 = -28.4(7.3)\,\mathrm{GeV}^2$ (describing the volume effect), with an $\chi^2/\mathrm{d.o.f.} = 0.74$. The fits are included in the figure. We see from the contour plot in Fig. 7.9.a that the estimated

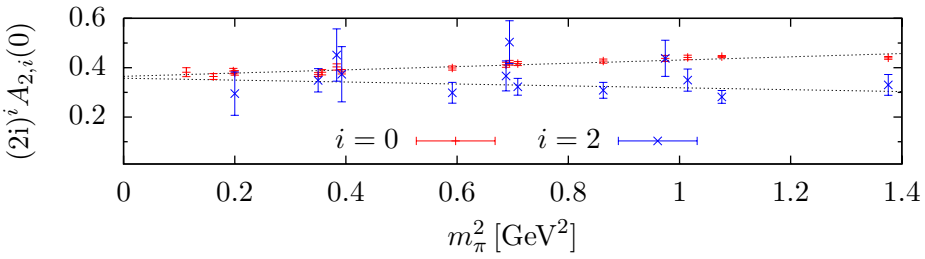

Figure 7.8 | A test of the soft pion theorem. Note that we neglect any form of lattice artifacts in this plot. The dotted lines are linear approximations.

finite size effects are slightly stronger than for the form factor. However, the data points for $M^2_{0,\text{lat}}$ at $m_\pi^2 \approx 0.2\,\text{GeV}^2$ agree within errors, indicating the absence of finite size effects. Because of the exploratory nature of our finite size estimate, we will proceed as in Chapter 6, i.e. we exclude the lightest lattices where we anticipate corrections due to the finite volume from further fits. We include them in our plots for reference only. The analysis of the data for $M_{2,\text{lat}}$ is again more cumbersome. The plot in Fig. 7.10 already shows that there is no significant effect. The fits are also not stable against including only the finite size runs or additional lattices as input. We thus have no handle to even estimate the effect of small physical volumes.

7.2.3 Extrapolations in Pion Mass

The extrapolation of our results to the physical pion mass will once again be performed linearly in the lattice pion mass. We start by considering the forward limit and the monopole mass separately, followed by a global fit reducing the total number of parameters involved.

Forward Limit and Monopole Mass

We use the linear ansatz

$$A_{2,i}(0, m_\pi^2) = c_0^i + c_1^i m_\pi^2 \;\text{ and }\; M_i^2(m_\pi^2) = d_0^i + d_1^i m_\pi^2 \tag{7.14}$$

for the forward limit and monopole mass, respectively. The fit parameters, obtained by fits to our lattice data with $m_\pi^2 > 0.3\,\text{GeV}^2$, are given in Table 7.3. The corresponding fits are included in Fig. 7.7. Comparing the extrapolated value of $A_{2,0}(0) = 0.261(4)$ to the (averaged) previous result for $\langle x\rangle^{\overline{\text{MS}}}_{(\boldsymbol{p}\neq 0)} = 0.268(8)$ shows good agreement between the two approaches. Note that the current technique combines all operator combinations and momenta that yield $\boldsymbol{q} = 0$ by our over-constrained fit to Eq. 7.11 and the lattice ratio $R(\tau)$.

Since the linear relation between M_i^2 and m_π^2 is only motivated by the plot itself, we also tested an extrapolation of the monopole mass against the pion mass squared. It yields a very similar (somewhat larger) χ^2 with larger extrapolated monopole masses ($M_0^{\text{phys}} = 1.349(52)\,\text{GeV}$ and $M_2^{\text{phys}} = 0.98(22)\,\text{GeV}$). We consider the difference between the two extrapolations as systematic uncertainty.

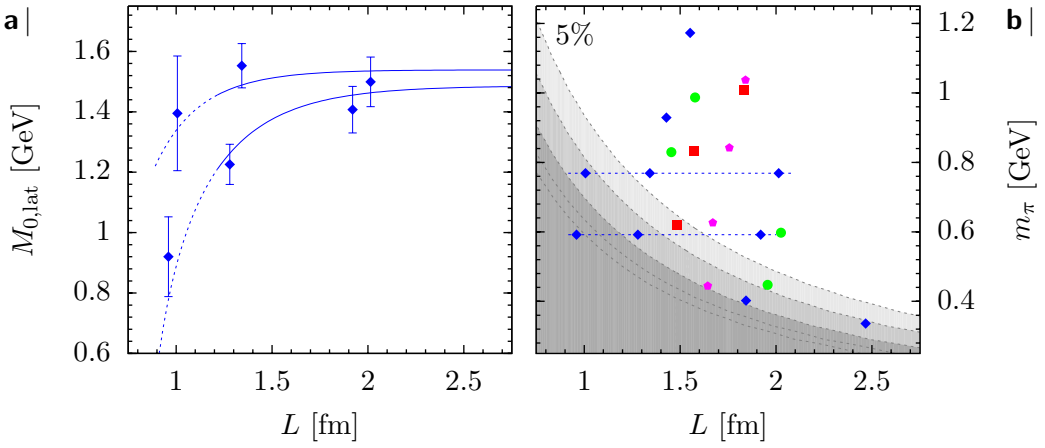

Figure 7.9 | Our estimated finite size effect for M_0^{lat} as discussed in the text. **a** | shows the finite size runs, **b** | gives an overview of lattices in the m_π-L plane with contours corresponding to the relative shift of 5%, 10%, 20%, 30% and 40%.

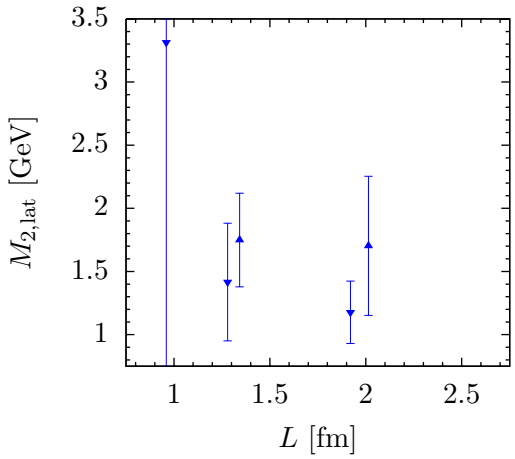

Figure 7.10 | Monopole masses M_2^{lat} for our finite size lattices, with no visible effect.

Combined Fits

From the above, a combined fit to all lattices (again with $m_\pi^2 > 0.3\,\mathrm{GeV}^2$) then follows

$$A_{2,i}(\Delta^2, m_\pi^2) = A_{2,i}(0, m_\pi^2)\left(1 - \frac{\Delta^2}{M_i^2(m_\pi^2)}\right)^{-1}, \tag{7.15}$$

with $A_{2,i}(0, m_\pi^2)$ and $M_i^2(m_\pi^2)$ as given in Eq. (7.14). The results to such fits are shown in Fig. 7.11, where we have shifted the lattice data to the physical point (as it was done in Sec. 6.5); the fit parameters can be found in Table C.8. With a monopole mass of $M_0 = 1.370(70)\,\mathrm{GeV}$ and a forward value of $A_{2,0}^{\overline{\mathrm{MS}}}(0) = 0.261(5)$, the combined fit to $A_{2,0}$ yields a similar result as the separate extrapolations discussed above. A combined fit also makes it easy to try different exponents again, not just a monopole form (using Eqs. (7.12) and (7.14)). Results for up to $p = 4$ are given in the table. Since the derivative with respect to Δ^2 does not change at $\Delta^2 = 0$ for different p, the pole mass should be of comparable

size for all p, which is indeed what we find. The χ^2 changes very little only, so none of the fits is particularly preferred.

A combined fit to the data for the second form factor turns out not quite as good, which is likely to be connected to the much larger errors, some of the shifted lattice points also having the wrong sign. While the forward value ($A_{2,2}^{\overline{\text{MS}}}(0) = 0.076(5)$) is stable, the monopole mass turns out lower ($M_2 = 0.38(27)\,\text{GeV}$) when using a monopole fit. Using different exponents has little effect on the χ^2, but changes the monopole mass.

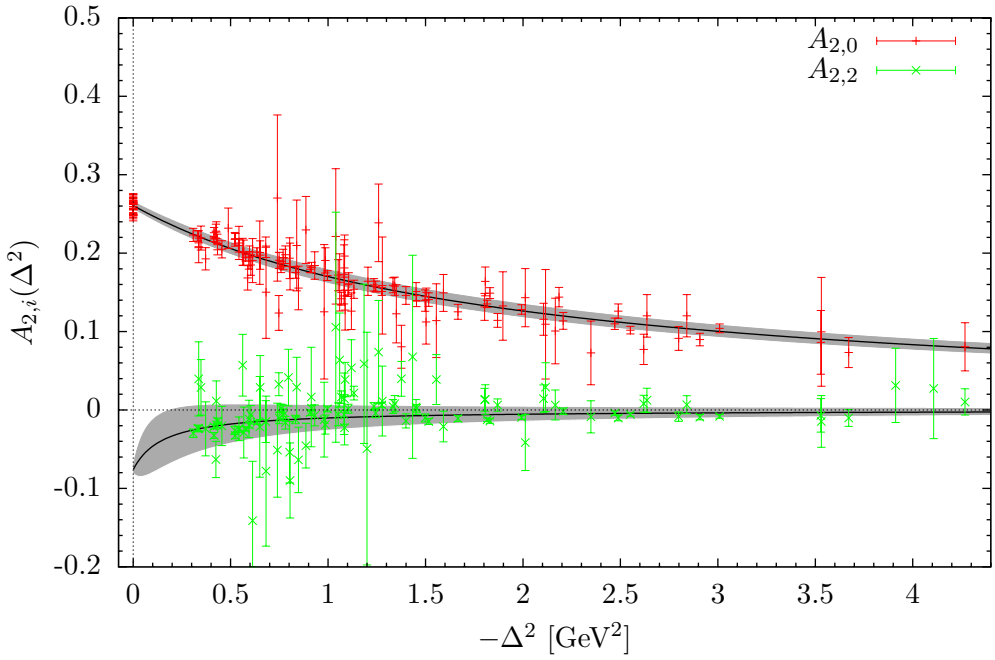

Figure 7.11 | Combined fit of $A_{2,i}(\Delta^2)$ to our lattices. The results are shifted to the physical point. We have omitted data points of $A_{2,0}$ ($A_{2,2}$) with an error bigger than 70% (500%) in the plot for better visibility.

Table 7.3 | Fit parameters to our extrapolations w.r.t. the pion mass. Parameters of the forward results are for renormalised values (RGI). We also provide the results at the physical pion mass in $\overline{\text{MS}}$ at $\mu = 2\text{GeV}$.

i	c_0^i	c_1^i [GeV^{-2}]	χ^2/d.o.f.	$A_{2,i}^{\text{phys, }\overline{\text{MS}}}(0)$
0	0.364(6)	0.067(6)	2.02	0.261(4)
2	-0.092(11)	0.012(12)	1.17	-0.066(8)
i	d_0^i [GeV^2]	d_1^i	χ^2/d.o.f.	M_i^{phys} [GeV]
0	1.75(16)	0.79(17)	0.50	1.329(58)
2	0.77(49)	0.95(63)	0.88	0.89(25)

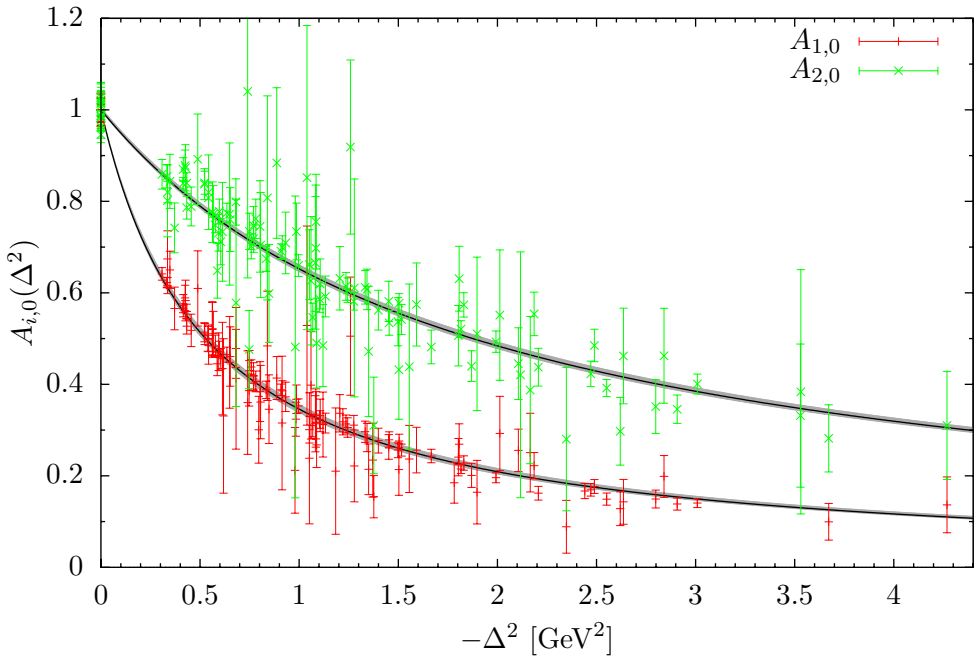

Figure 7.12 | Combined fit of $A_{i,0}(\Delta^2)$ to our lattices, both normalised to one. The comparison of the two results shows that the distribution of quarks becomes narrower for their momentum fraction $x \to 1$. The results have been shifted to the physical pion mass as before and we have omitted data points with an error larger than 70% in the plot.

7.2.4 Discussion of the Off-Forward Results

Our results for the second moment of the pion vector GPD H_π^q showed the expected value in the forward limit. From our combined fits we find $A_{2,0}^{\overline{\text{MS}}}(0) = 0.261(5)$ and $A_{2,2}^{\overline{\text{MS}}}(0) = -0.076(5)$ with purely statistical errors. The first number reproducing the result from the previous section, which cannot be seen as completely independent information, but rather a test of our fitting procedure analysis codes. The second number is in conjunction with the soft pion theorem.

The monopole masses, which describe the momentum behaviour of the two GFFs, are $M_0^{\text{phys}} = 1.370(70)(20)\,\text{GeV}$ and $M_2^{\text{phys}} = 0.38(27)(9)\,\text{GeV}$, also from our combined fits. Here the first error is statistical, and second reflects a systematic uncertainty in the extrapolation. We note that the error on M_2 is probably underestimated due to the problems with the fit.

We can give a physical meaning to M_0, when we consider the distribution of partons in the transverse plane, $\langle \boldsymbol{r}_\perp^2 \rangle$ (c.f. Sec. 2.4). This is related to the vector GPD $H_\pi^q(x, 0, -\boldsymbol{\Delta}_\perp^2)$, Eq. (2.13), and depends on the momentum carried by the quarks. A larger momentum fraction should be reflected in a narrower distribution. The average impact parameter should in fact be independent of Δ^2 as x goes to one. Since higher moments $M_{n+1}(H_\pi^q)$ in x put more weight on larger momentum fractions, the fall-off of the momentum dependence of $A_{2,0}$ should be smaller than for $A_{1,0}$, until it finally becomes flat for $n \to \infty$. We indeed find this behaviour, as clearly shown in Fig. 7.12 where for clarity we normalised both GFFs to one. It is also obvious from the higher monopole mass for $A_{2,0}$ when

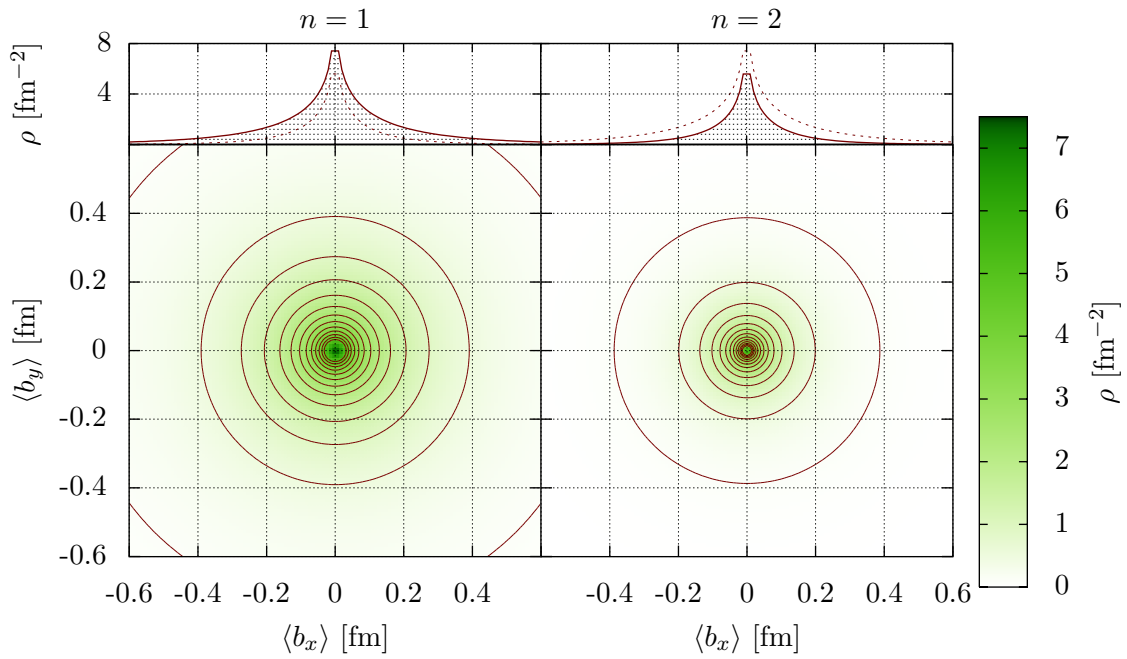

Figure 7.13 | Moments of the transverse distribution $q(x, \boldsymbol{b}_\perp)$ corresponding to $A_{n,0}$ shown as probability densities ρ. The contour lines are equally spaced and identical for both cases. Included on the top are the densities for $\langle b_y \rangle = 0$. We clearly observer a narrower distribution for $n = 2$.

compared to the pion form factor (Chapter 6). A more intuitive approach is to compute the Fourier transform of $A_{n,0}(\Delta^2)$ to impact parameter space, which leads to moments of the distribution $q(x, \boldsymbol{b}_\perp)$, Eq. (2.11). The Fourier transform of our p-pole in Eq. (7.12) to transverse space is [25]

$$A(\boldsymbol{b}_\perp^2) = A(0)\frac{pM_A^2}{2^p \pi\, \Gamma(p)}(\sqrt{p} M_A\, b)^{p-1}\, K_{p-1}(\sqrt{p} M_A\, b) \tag{7.16}$$

with modified Bessel functions and $b = \sqrt{\boldsymbol{b}_\perp^2}$. Our results for $A_{1,0}$ and $A_{2,0}$ are displayed in Fig. 7.13 which now make the narrowing directly visible.

7.3 Conclusion

We have calculated the higher moments of the pion structure with pions from the axial-vector interpolating field. First, we focused on the forward limit that is relevant for pion PDFs. Comparison with phenomenological expectations derived from experiments showed good agreement. Our results also include a lattice prediction that quarks carry about 54% of the pions momentum.

We then examined the second moment of the off-forward distribution. Using a monopole ansatz for the momentum dependence and extracting the monopole masses, we were able to extrapolate our results to the physical pion mass. It was possible to infer a narrowing distribution of quarks, when the momentum fraction is increased. We also found evidence for a soft pion theorem, relating the forward limit of the two GFFs to each other.

The biggest ambiguity in our present analysis stems from lattice artifacts that are not under control yet. In particular, finite volume effects could not be obtained unambiguously but seem to be present for our lightest pion masses. As for the form factor we require additional data points to clarify the situation.

Outlook – The Transverse Spin Structure of the Pion

Although the pion itself has spin zero and cannot be polarised, this is not true for its constituents. Hence, it is worthwhile investigating the Boer-Mulders effect [12] for the pion. This effect refers to an asymmetry in scattering experiments, manifest as a correlation of the transverse momentum of the ejected quark and its polarisation inside the target. These so-called single spin asymmetries (SSA) have recently been subject of numerous theoretical studies. Experimental evidence is however scarce. While the Sivers effect[3] has been measured for example at the HERMES experiment at DESY, the efforts to find the Boer-Mulders effect are only about to start. Again, this will be for a nucleon target. Hence theory and in particular model-free lattice calculations here have a unique opportunity to predict a yet unmeasured effect.

The pion vector and tensor GPDs of this study are the observables to investigate moments of the required spin densities. They relate to distribution functions in the transverse plane that allow for a probabilistic interpretation, as discussed in Sec. 2.4. These in turn allow for an interpretation of SSAs [14]. We recall the impact parameter PDFs in slightly more general form [92]

$$F_\Gamma(x, \boldsymbol{b}_\perp) = \int \frac{z^-}{2\pi}\, e^{\mathrm{i}xp^+z^-} \left\langle \pi(p'^+, \mathbf{0}_\perp)\right| \bar\psi_q(-\frac{z^-}{2}, \boldsymbol{b}_\perp)\Gamma\psi_q(\frac{z^-}{2}, \boldsymbol{b}_\perp) \left|\pi(p^+, \mathbf{0}_\perp)\right\rangle , \qquad [2.11]$$

where we have again used states $\left|\pi(p^+, \mathbf{0}_\perp)\right\rangle$ of fixed light-cone momentum and transverse position. To project onto quarks with definite transverse polarisation $\boldsymbol{s}$, we use the operator $\frac{1}{2}\bar q[\gamma^+ - s^j \mathrm{i}\sigma^{+j}\gamma_5]q$, [25]. The first term is just our vector operator, and the second term becomes proportional to our tensor current upon using the identity $\sigma^{\mu\nu}\gamma_5 = -\frac{1}{2}\epsilon^{\mu\nu\alpha\beta}\mathrm{i}\sigma_{\alpha\beta}$. With the definition of the pion GPDs, Eqs. (2.5a) and (2.5b), and performing the Fourier transform to transverse position, we arrive at the (properly normalised) density for transversely polarised quarks q inside the pion

$$\rho^q(x, \boldsymbol{b}_\perp) = \frac{1}{2}\left(H^q_\pi(x, \boldsymbol{b}_\perp^2) - \frac{s^i\epsilon^{ij}b^j_\perp}{m_\pi}\frac{\partial}{\partial \boldsymbol{b}_\perp^2} E^q_{\mathrm{T}\,\pi}(x, \boldsymbol{b}_\perp^2)\right). \qquad (8.17)$$

Here $H^q_\pi(x, \boldsymbol{b}_\perp^2)$ and $E^q_{\mathrm{T}\,\pi}(x, \boldsymbol{b}_\perp^2)$ are the Fourier transformed GPDs, c.f. Eqs. (2.12a) and (2.12b) (where we denoted them q and q_T). Our lattice data again yields moments of the density $\rho(x, \boldsymbol{b}_\perp)$.

Since the Fourier transform is taken for $\boldsymbol{\Delta}_\perp$ while $\Delta^+ = 0$, only form factors which have a factor of ξ^0 in Eqs. (2.25a) and (2.25b) survive. Hence we need the vector GFFs $A_{n,0}$ that we discussed in the previous chapters, and the tensor GFFs $B_{\mathrm{T}\,n,0}$ that have not

[3] The Sivers effect also generates SSAs but requires a polarised target and does not apply to the pion.

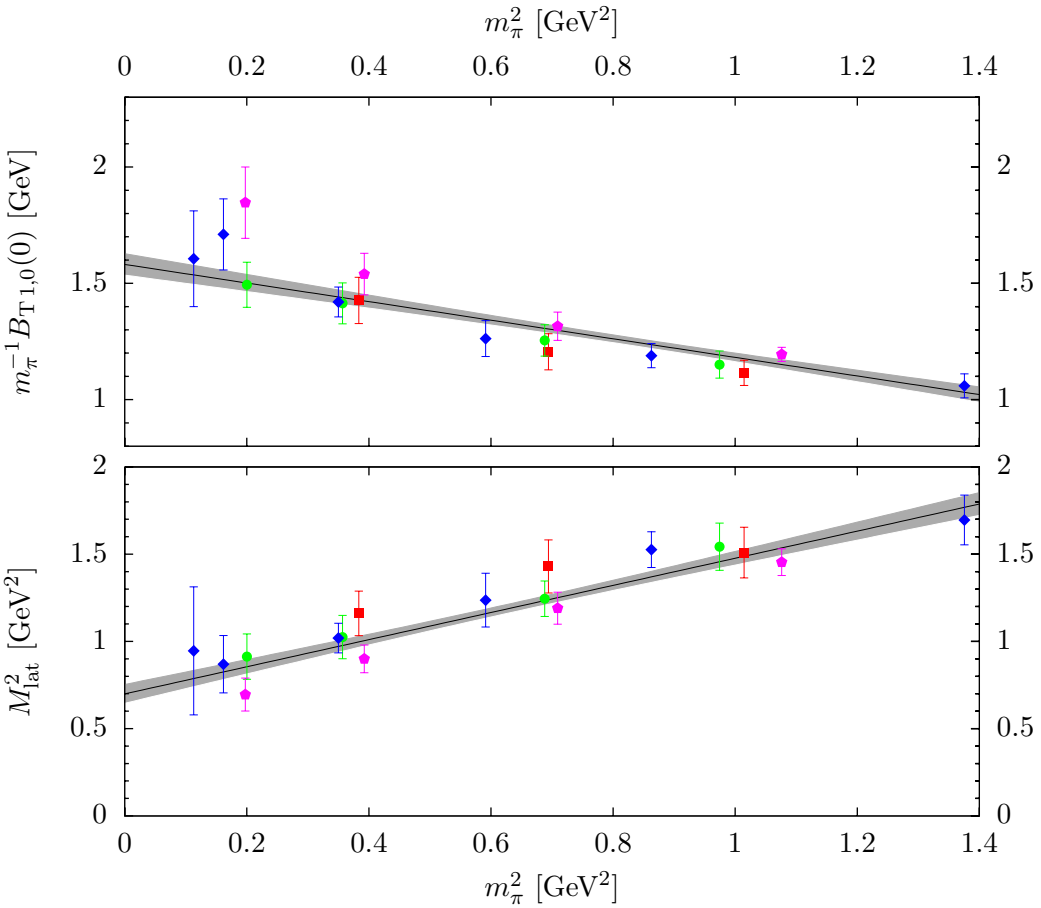

Figure 8.14 | Preliminary extrapolations of the norm $B_{\mathrm{T}\,1,0}(0)$ (*top*, at $\overline{\mathrm{MS}}$ with $\mu = 2\,\mathrm{GeV}$) and dipole mass M (*bottom*) of the tensor form factor $B_{\mathrm{T}\,1,0}(\Delta^2)$.

been covered yet. We will now provide a preliminary outlook on the first Mellin moment of the density ρ.

The momentum dependence of $B_{\mathrm{T}\,1,0}(\Delta^2)$ is fitted with the customary p-pole ansatz, Eq. (7.12). We want to note again that this ansatz provides a good description of our lattice data but is somewhat arbitrary and not motivated by physics arguments. As already pointed out in Sec. 7.2.1, the constraint of having regular densities at the origin limits the possibilities to $p > 3/2$. The lattice data is not very sensitive to the choice of p, and we took a fixed $p = 2$ for simplicity. The χ^2/d.o.f. for such a choice varies from 0.3 to 2.3 for our different lattices.

The extrapolation of the resulting dipole masses is shown in Fig. 8.14. It follows a linear relation between the squared dipole mass M_{lat} and the pion mass squared. Using all lattices and neglecting any lattice artifacts we obtain a preliminary result of $M^{\mathrm{phys}} = 0.845(33)\,\mathrm{GeV}$. The extrapolation of the forward value $B_{\mathrm{T}\,1,0}(0)$ is also included in Fig. 8.14. The form of the extrapolation is guided by chiral perturbation theory that finds a vanishing forward value in the chiral limit [90]. We thus extrapolate $m_{\pi,\mathrm{lat}} B_{\mathrm{T}\,1,0}(0)$ against the squared pion mass to find $B_{\mathrm{T}\,1,0}(0) = 0.219(6)$ at the physical point in the $\overline{\mathrm{MS}}$-scheme with $\mu = 2\,\mathrm{GeV}$. For both extrapolations, the two lattices at $m_\pi^2 \approx 0.2\,\mathrm{GeV}^2$

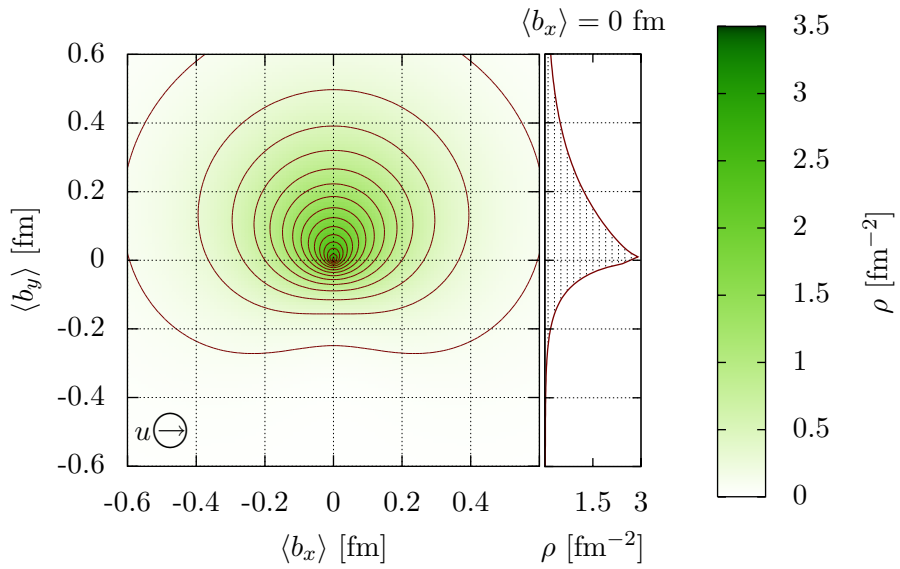

Figure 8.15 | Preliminary first moment of the density of transversely polarised ($\boldsymbol{s} = (1, 0)^{\mathrm{T}}$) u-quarks inside a π^+ in the impact parameter plane. Clearly visible is the shift along the positive b_y direction suggesting a correlation between quark spin and orbital momentum.

(hexagon and circle) suggest that finite size effects are important since they have a different physical volume. The extrapolations, however, go through the data point with the bigger volume.

To arrive at the transverse densities given in Eq. 8.17, we finally need to Fourier transform the found p-poles. We follow [25], and obtain the preliminary densities shown in Fig. 8.15. Very clearly, we observe a shifted distribution for polarised quarks in the pion. This is similar to observations made for the nucleon and also in line with recent model calculations [92, 93]. Note that the specific shape of the distribution, especially near the centre, depends on the chosen p-pole and its extrapolation. The predictability for small values of $\boldsymbol{b}_\perp$ is further somewhat restricted by the lattice calculation, since it requires a large momentum transfer which is limited on the lattice. Furthermore, one should bear in mind that the lattice spacing a also imposes a lower bound on the possible resolution.

The interpretation of this result is intuitive in a semi-classical way [14]. Consider the pion as a sphere moving in the z-direction, Fig. 8.16. A rotation around b_x would then add (subtract) to the velocity in the z-direction for $b_y > 0$ ($b_y < 0$), and thus change the distribution of longitudinal momenta depending on the transverse position. The effect an observer at rest would be a quark density shifted towards positive b_y in the transverse plane. Of course the pion is not a sphere, but rather a Lorentz contracted disc, making an interpretation in terms of quark angular momentum more difficult.

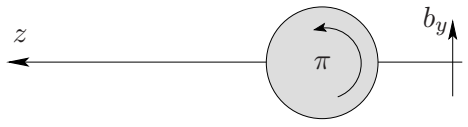

Figure 8.16 | A classical rotating pion to explain the increased density of quarks for $b_y > 0$.

A more detailed analysis of the densities of transversely polarised quarks will follow in the near future. This will include an investigation of the momentum dependence, the extrapolation to the physical pion mass and lattice artifacts.

Summary

In this thesis, we have discussed several aspects of the pion structure that are accessible with lattice QCD. In our introduction, we briefly mentioned QCD phenomenology for the pion that is obtained from experiments, namely the electromagnetic form factor connected to the charge radius, and the parton distribution functions (PDFs) which provide probabilities of finding a parton with a certain momentum fraction (Chapter 1). These are embedded in the more general framework of generalised parton distributions (GPDs) for which we gave a short review in Chapter 2 and which form the basis of this work. Although this concept is not new, it has recently been rediscovered and is now actively investigated in both, theory and experiment. We gave the definition for the pion case and showed how the GPDs relate to the known observables. In particular, we tried to convey an intuitive picture. The intuition can however be misleading if one does not constrain oneself to transverse space as we tried to stress. Only then is a probabilistic interpretation possible. Special attention was paid to Mellin moments of GPDs that are parametrised in generalised form factors relevant for lattice calculations.

The two subsequent Chapters 3 and 4 were devoted to an introduction to lattice QCD and the lattice techniques we used. Here we started from the QCD Lagrangian and the path integral, to then explain our lattice gauge and fermion action, both going back to Wilson. For the latter we used the clover improved version for our dynamical two flavour simulations. We then gave details of the calculation of two- and three-point functions on the lattice, as well as the operators involved and how the matrix elements are extracted from the lattice data by building suitable ratios.

The discussion of our numerical results was organised in separate parts: Chapter 5 gave a short overview of pion two-point functions from which pion energies and the dispersion relation can be extracted. The pion form factor was used in Chapter 6 for an exhaustive explanation of our methods to analyse the data. We investigated the momentum dependence of the form factor and its extrapolation to physical pion masses. We also payed attention to the lattice artifacts appearing in any lattice simulation. That is we explored discretisation errors and the effect of improving the vector current. We also tried to estimate the size of finite volume corrections. This allowed us to compare with results from chiral perturbation theory. In Chapter 7 we applied the established methods to the analysis of higher moments of the forward distributions and the second moment of the non-forward case. While the form factor lead to the charge radius of the pion, this now made it possible to derive pion PDFs and densities of quarks in the transverse plane. Finally, we gave an outlook on the densities of polarised quarks in the pion – an observable which provides novel information about the pion structure and has not been measured in experiments yet.

While our results are in excellent agreement with experiments in case of the form factor, and compatible with phenomenological results for the PDFs, their accuracy is still limited by ambiguities in the chiral extrapolation and lattice artifacts introducing systematic uncertainties. Our analysis showed that discretisation errors can be neglected or are

at least small, certainly at the level of present statistical errors. More problematic are finite size effects, which need better analytic control. This is in reach, with additional simulations at light quark masses, also at different volumes, that are just being performed. Nevertheless, additional input from chiral perturbation theory (for example [80]) will be necessary to fully clarify the finite volume effects.

Apart from the caveats just mentioned, lattice QCD has provided valuable insights into the structure of the pion. The quark densities in the transverse plane are unprecedented and not yet measured in experiments. It is indeed unclear if the necessary experiments are feasible. Furthermore, the predictions from lattice QCD can now be used to challenge our understanding of the strong force when compared to model calculations.

Appendix

A Our Ensemble of Lattices

Our simulation is performed using a rational hybrid Monte Carlo simulation. Independent configurations are obtained every 40 trajectories. We use the multiple source technique to be able to use every fifths configuration. The parameters of our lattices are given in Table A.1. The scale is set using the Sommer parameter with $r_0 = 0.467$ fm.

Table A.1 | Overview of our lattice parameters. For physical units the Sommer parameter with $r_0 = 0.467$ fm has been used. The error on m_π is purely statistical.

β	#	κ	$N^3 \times T$	m_π [GeV]	a [fm]	L [fm]	$m_\pi L$	N_{traj}
5.20	1	0.13420	$16^3 \times 32$	1.007(2)	0.115	1.8	9.4	$\mathcal{O}(5000)$
	2	0.13500	$16^3 \times 32$	0.833(3)	0.098	1.6	6.6	$\mathcal{O}(8000)$
	3	0.13550	$16^3 \times 32$	0.619(3)	0.093	1.5	4.7	$\mathcal{O}(8000)$
5.25	4	0.13460	$16^3 \times 32$	0.987(2)	0.099	1.6	7.9	$\mathcal{O}(5800)$
	5	0.13520	$16^3 \times 32$	0.829(3)	0.091	1.5	6.1	$\mathcal{O}(8000)$
	6	0.13575	$24^3 \times 48$	0.597(1)	0.084	2.0	6.1	$\mathcal{O}(5900)$
	7	0.13600	$24^3 \times 48$	0.447(1)	0.081	2.0	4.4	$\mathcal{O}(5200)$
5.26	8	0.13450	$16^3 \times 32$	1.011(3)	0.099	1.6	8.1	$\mathcal{O}(4000)$
5.29	9	0.13400	$16^3 \times 32$	1.173(2)	0.097	1.6	9.2	$\mathcal{O}(4000)$
	10	0.13500	$16^3 \times 32$	0.929(2)	0.089	1.4	6.7	$\mathcal{O}(5600)$
	11	0.13550	$24^3 \times 48$	0.769(2)	0.084	2.0	7.9	$\mathcal{O}(2000)$
	12	0.13590	$24^3 \times 48$	0.592(2)	0.080	1.9	5.8	$\mathcal{O}(5900)$
	13	0.13620	$24^3 \times 48$	0.402(3)	0.077	1.9	3.8	$\mathcal{O}(5600)$
	14	0.13632	$32^3 \times 64$	0.336(2)	0.077	2.5	4.2	$\mathcal{O}(2400)$
5.40	15	0.13500	$24^3 \times 48$	1.037(1)	0.077	1.8	9.7	$\mathcal{O}(3700)$
	16	0.13560	$24^3 \times 48$	0.842(2)	0.073	1.8	7.5	$\mathcal{O}(3500)$
	17	0.13610	$24^3 \times 48$	0.626(2)	0.070	1.7	5.3	$\mathcal{O}(3900)$
	18	0.13640	$24^3 \times 48$	0.444(3)	0.068	1.6	3.7	$\mathcal{O}(5100)$

Table A.2 | Values for r_0/a for our different β-values; taken in the chiral limit.

β	5.20	5.25	5.29	5.40
r_0/a	5.444(72)	5.851(95)	6.158(53)	6.951(54)

Table A.3 | Parameters used for smearing our quark fields. They are generic for one β value where no κ values have been specified.

β	κ_{sea}	N_{smear}	κ_{smear}
5.20		50	0.21
5.25		60	0.21
5.29	0.134	50	0.21
		60	0.21
	0.13632	65	0.21
5.40	0.135, 0.1356	65	0.21
	0.1361, 0.1364	0.75	0.21

B Lattice operators

The general form of our lattice operators is given by

$$\mathcal{O}_{\mu\mu_1\mu_2\ldots\mu_n} = F_{ff'}\,\bar{\psi}^{(f)}\Gamma\overleftrightarrow{D}_{\mu_1}\overleftrightarrow{D}_{\mu_2}\ldots\overleftrightarrow{D}_{\mu_n}\psi^{(f')} \tag{B.1}$$

where Γ is an element of the full Clifford algebra, i.e. we compute $\Gamma \in \{1, \gamma_5, \gamma_\mu, \gamma_5\gamma_\mu, \sigma_{ij}\}$ with $i, j = 1, \ldots, 4$ and $i < j$ (the derivative was defined in Eq. (4.18)). The above definition thus includes both, the vector as well as the tensor operators, Eqs. (4.17a) and (4.17b).

We use the abbreviation $\{\ldots\}$ for symmetrisation of indices. The operator combinations that are used for the forward matrix elements of the vector current have the simplifying choice $\boldsymbol{p} = (1,0,0), (0,1,0)$ and $(0,0,0)$. We label the 'forward operators' explicitly with $\mathcal{O}_{v2a}$, $\mathcal{O}_{v2b}$, $\mathcal{O}_{v3}$ and $\mathcal{O}_{v4}$ [44]. A complete list of operators can be found in [43]. The subset we use is:

$\boldsymbol{n = 0}$, $\tau_1^{(4)}$, $C = -1$

$$\mathcal{O}_\mu\,, \quad 1 \le \mu \le 4. \tag{B.2}$$

$\boldsymbol{n = 1}$, $\tau_3^{(6)}$, $C = +1$

$$\mathcal{O}_{v2a} = \mathcal{O}_{\{\mu\nu\}}\,, \quad 1 \le \mu < \nu \le 4, \tag{B.3}$$

$\tau_1^{(3)}$, $C = +1$

$$\mathcal{O}_{v2b} = \mathcal{O}_{44} - \frac{1}{3}\left(\mathcal{O}_{11} + \mathcal{O}_{22} + \mathcal{O}_{33}\right)\,. \tag{B.4}$$

The non-forward moments have additional operators and a slightly different linear combination (however, we still have $\tau_1^{(3)}$, $C = +1$):

$$\frac{1}{2}(\mathcal{O}_{11} + \mathcal{O}_{22} - \mathcal{O}_{33} - \mathcal{O}_{44})\,, \quad \frac{1}{\sqrt{2}}(\mathcal{O}_{33} - \mathcal{O}_{44})\,, \quad \frac{1}{\sqrt{2}}(\mathcal{O}_{11} - \mathcal{O}_{22}) \tag{B.5}$$

$\boldsymbol{n = 2}$, $\tau_1^{(8)}$, $C = -1$

$$\mathcal{O}_{v3} = \mathcal{O}_{\{44\mu\}} - \frac{1}{2}\left(\mathcal{O}_{\{22\mu\}} + \mathcal{O}_{\{33\mu\}}\right)\,, \quad \mu = 1, 2. \tag{B.6}$$

$\boldsymbol{n = 3}$, $\tau_1^{(2)}$, $C = +1$

$$\mathcal{O}_{v4} = \mathcal{O}_{\{1144\}} + \mathcal{O}_{\{2233\}} - \frac{1}{2}\left(\mathcal{O}_{\{1133\}} + \mathcal{O}_{\{1122\}} + \mathcal{O}_{\{2244\}} + \mathcal{O}_{\{3344\}}\right)\,, \quad 1 \leftrightarrow 2. \tag{B.7}$$

We have also stated the irreducible representation of the hypercubic group $H(4)$ the operators belong to: $\tau_k^{(l)}$, where l is the dimension of the representation and k labels different representations of the same dimension. C is the charge conjugation parity of the operator. Note that the operators are all traceless and symmetrised appropriately.

C Compiled data

Table C.1 | Monopole masses M_{lat} obtained from fits to (6.2) for the axial pion current. Also included is the calculated monopole mass (in finite volume) together with the estimated finite size shift from the fit to (6.15). Errors are statistical only.

#	M_{lat} [GeV]	M_{vol} [GeV]	ΔM_{vol} [MeV]
1	1.105(22)	1.083	0.3
2	0.997(21)	0.984	4.6
3	0.880(24)	0.894	38.3
4	1.080(20)	1.071	1.2
5	0.975(18)	0.979	7.8
6	0.870(22)	0.870	8.6
7	0.747(18)	0.770	52.0
8	1.066(25)	1.084	0.9
9	1.157(20)	1.180	0.3
10	1.051(15)	1.036	4.0
11	0.971(14)	0.955	1.4
12	0.854(15)	0.863	12.6
13	0.783(29)	0.699	108.2
14	0.708(43)	0.720	69.0
15	1.099(11)	1.100	0.2
16	0.981(14)	0.991	2.0
17	0.847(17)	0.871	19.8
18	0.690(18)	0.708	112.6

Table C.2 | Constants c_i and c_i' for the chiral extrapolation formulae, Eqs. (6.21) and (6.22)

	1	2	3	4	5	6
$c_i \times 10^4$	63.3257	2.40609	1.57234	1.26988	0.80203	2.74602
c_i'	0.138852	0.694077	0.453568	0.366318	0.231359	0.792135

Table C.3 | Moments of the forward vector GPD. The given values are renormalised RGI matrix elements and not in $\overline{\text{MS}}$. We also give the used fit ranges. For $\boldsymbol{p} \neq 0$ two momenta are averaged. Errors are statistical only.

#	$\mathcal{O}_{v2a}$		$\mathcal{O}_{v2b}$				$\mathcal{O}_{v3}$		$\mathcal{O}_{v4}$	
	$\boldsymbol{p} \neq 0$		$\boldsymbol{p} \neq 0$		$\boldsymbol{p} = 0$		$\boldsymbol{p} \neq 0$		$\boldsymbol{p} \neq 0$	
1	0.452(17)	3-13	0.4878(33)	3-13	0.4881(18)	5-11	0.244(11)	5-11	0.160(10)	5-11
2	0.408(29)	3-13	0.448(15)	3-13	0.4512(85)	5-11	0.248(19)	3-13	0.162(20)	5-11
3	0.390(51)	3-13	0.442(20)	3-13	0.4285(71)	5-11	0.219(33)	3-13	0.153(43)	5-11
4	0.435(22)	3-13	0.4671(54)	5-11	0.4706(23)	5-11	0.228(15)	5-11	0.151(14)	5-11
5	0.400(27)	3-13	0.4388(82)	5-11	0.4485(30)	5-11	0.236(17)	3-13	0.131(19)	5-11
6	0.394(27)	5-19	0.3930(76)	7-17	0.3955(39)	7-17	0.235(19)	5-19	0.152(47)	9-15
7	0.392(66)	4-19	0.384(21)	7-17	0.3897(73)	7-17	0.273(53)	8-16	0.29(12)	9-15
9	0.475(18)	3-13	0.4940(35)	5-11	0.4986(19)	5-11	0.2559(96)	3-13	0.170(12)	5-11
10	0.459(22)	3-13	0.4706(66)	5-11	0.4633(22)	5-11	0.247(14)	5-11	0.169(14)	5-11
11a	0.29(26)	5-11	0.48(12)	5-11	0.5045(90)	5-11	0.127(87)	5-11	0.179(82)	5-11
11b	0.464(32)	3-13	0.447(10)	5-11	0.4539(40)	5-11	0.271(20)	3-13	0.193(23)	5-11
11	0.435(20)	5-19	0.4256(49)	7-17	0.4312(34)	7-17	0.224(17)	7-17	0.171(28)	9-15
12a	0.49(179)	5-11	0.385(84)	5-11	0.612(47)	5-11	0.20(23)	5-11	0.13(17)	5-11
12b	0.390(46)	3-13	0.443(15)	3-13	0.4854(69)	3-13	0.224(32)	5-11	0.172(35)	5-11
12	0.388(17)	5-19	0.3969(60)	7-17	0.4046(28)	7-17	0.216(14)	7-17	0.165(34)	9-15
13	0.405(83)	5-19	0.409(41)	9-15	0.397(11)	7-17	0.302(65)	7-17	–	
14	0.413(86)	10-22	0.349(32)	10-22	0.386(18)	8-24	0.224(88)	10-22	–	
15	0.462(13)	5-19	0.4672(33)	9-15	0.4705(16)	6-18	0.2549(85)	6-18	0.160(13)	9-15
16	0.450(16)	5-19	0.4469(40)	6-18	0.4407(23)	6-18	0.258(11)	6-18	0.183(19)	9-15
17	0.362(27)	5-19	0.3931(74)	5-19	0.4065(43)	9-15	0.223(20)	6-18	0.109(38)	9-15
18	0.389(64)	5-19	0.396(24)	9-15	0.4114(95)	8-16	0.202(52)	9-15	0.109(98)	9-15

Table C.4 | The *upper* table contains the renormalisation constants for our operators to obtain RGI matrix elements. The errors are systematic uncertainties from the extrapolation. The conversion factors from the RGI point to the $\overline{\text{MS}}$ scheme at a certain scale μ are given in the *lower* table. The errors are estimates due to the uncertainty in Λ_{QCD}. Both from [94].

	β			
$Z_{\mathcal{O}}^{\text{RGI}}(\beta)$	5.20	5.25	5.29	5.40
$\mathcal{O}_{v2a}$	1.50(2)	1.51(2)	1.52(1)	1.56(1)
$\mathcal{O}_{v2b}$	1.51(3)	1.51(2)	1.53(2)	1.57(2)
$\mathcal{O}_{v3}$	2.40(5)	2.40(5)	2.40(5)	2.48(5)
$\mathcal{O}_{v4}$	3.75(10)	3.70(10)	3.70(10)	3.85(10)

	μ^2 [GeV^2]		
$Z_{\mathcal{O}}^{\overline{\text{MS}},\,\text{RGI}}(\mu)$	2	4	5
$\mathcal{O}_{v2}$	0.76641(1.5%)	0.71544(2.5%)	0.70183(3%)
$\mathcal{O}_{v3}$	0.65174(1.5%)	0.58648(2%)	0.56943(2.5%)
$\mathcal{O}_{v4}$	0.57979(1%)	0.50844(2%)	0.49008(2.5%)

Table C.5 | The moments of the PDFs in the **chiral limit** ($m_\pi = 0$), separately for our different β values. All values are RGI matrix elements.

	β			
	5.20	5.25	5.29	5.40
$\mathcal{O}_{v2a}$	0.336(65)	0.365(43)	0.374(21)	0.352(34)
$\mathcal{O}_{v2b}\,(\boldsymbol{p} = 0)$	0.389(11)	0.361(6)	0.379(3)	0.376(5)
$\mathcal{O}_{v2b}\,(\boldsymbol{p} \neq 0)$	0.399(27)	0.352(12)	0.373(6)	0.376(9)
$\mathcal{O}_{v3}$	0.227(42)	0.242(29)	0.205(16)	0.231(24)
$\mathcal{O}_{v4}$	0.158(49)	0.117(53)	0.166(28)	0.152(44)

Table C.6 | This table contains the fitted parameters for the continuum limit. The notation is $c_0 + c_1 a^i$ for the linear fit (w.r.t. $i = 2$ for $\langle x \rangle$ and w.r.t. $i = 1$ otherwise). The constant is given by c. All values are RGI matrix elements again.

	c_0	c_1	χ^2/d.o.f.	c	χ^2/d.o.f.
$\mathcal{O}_{v2a}$	0.356(124)	1.6(21.8)	0.26	0.365(16)	0.26
$\mathcal{O}_{v2b}\,(\boldsymbol{p} = 0)$	0.382(19)	-1.1(3.3)	4.90	0.376(2)	4.95
$\mathcal{O}_{v2b}\,(\boldsymbol{p} \neq 0)$	0.392(37)	-3.7(6.6)	1.82	0.371(5)	1.97
$\mathcal{O}_{v3}$	0.230(168)	-0.2(2.2)	0.82	0.218(12)	0.82
$\mathcal{O}_{v4}$	0.182(260)	-0.3(3.4)	0.33	0.155(20)	0.33

Table C.7 | Fits to a p-pole form for $A_{2,i}$. Some of the fits seem to break down with very large masses or exponents (with errors of comparable size) and we omitted these in the table. The forward limit (norm of the fit) is the renormalised value and corresponds to $\langle x \rangle^{\mathrm{RGI}}$ for $i = 0$.

#	M_0	p_0	χ^2/d.o.f.	$M_0\,(p_0 = 1)$	$A^{\mathrm{RGI}}_{2,0}(0)$	χ^2/d.o.f.
1	1.61(19)	0.71(44)	0.23	1.692(82)	0.442(9)	0.23
2	1.55(17)	0.86(48)	0.65	1.593(78)	0.420(9)	0.58
3	1.63(20)	7.0(30.3)	0.54	1.414(95)	0.403(13)	0.68
4	1.73(20)	2.2(3.0)	0.17	1.575(78)	0.438(12)	0.24
5	1.64(15)	2.8(3.2)	0.48	1.458(65)	0.412(10)	0.68
6	1.66(33)	5.7(53.7)	0.65	1.515(129)	0.382(11)	0.60
7	1.10(21)	0.68(67)	0.89	1.159(98)	0.379(9)	0.76
9	1.76(10)	1.59(90)	1.09	1.665(45)	0.440(6)	1.08
10	1.64(13)	1.08(47)	1.05	1.615(56)	0.427(8)	0.92
11	1.57(20)	1.7(2.8)	0.19	1.499(82)	0.399(8)	0.19
12	1.45(19)	1.3(1.6)	1.02	1.407(77)	0.372(8)	0.91
13	–	–	–	1.440(205)	0.365(12)	1.83
14	0.41(48)	0.16(22)	0.56	0.822(150)	0.382(18)	0.68
15	1.68(10)	1.7(1.2)	1.71	1.596(41)	0.445(4)	1.61
16	1.54(15)	1.01(60)	0.48	1.539(63)	0.417(8)	0.43
17	1.32(15)	0.76(41)	1.35	1.379(74)	0.383(9)	1.18
18	1.17(23)	1.0(1.0)	0.85	1.173(94)	0.386(11)	0.71

#	M_2	p_2	χ^2/d.o.f.	$M_2\,(p_2 = 1)$	$A^{\mathrm{RGI}}_{2,2}(0)$	χ^2/d.o.f.
1	0.020(18)	0.316(54)	5.60	1.509(323)	0.087(11)	5.64
2	0.022(16)	0.484(67)	1.70	1.067(208)	0.126(22)	1.78
3	–	–	–	1.094(317)	0.112(26)	0.82
4	0.041(159)	0.480(81)	1.57	1.090(198)	0.110(18)	1.72
5	0.025(3.7)	0.414(101)	1.33	1.338(290)	0.092(15)	1.49
6	0.045(53)	0.409(98)	0.68	0.977(249)	0.069(13)	0.60
7	0.035(1.01)	.304(217)	1.02	1.286(778)	0.074(22)	0.92
9	0.017(12)	0.390(48)	5.06	1.422(241)	0.083(11)	5.46
10	0.020(16)	0.339(47)	3.31	1.684(272)	0.077(8)	3.44
11	0.024(6.2)	0.237(96)	2.14	1.703(550)	0.075(11)	2.14
12	0.029(30)	0.350(70)	0.65	1.177(247)	0.087(12)	0.68
13	0.027(423)	0.568(318)	0.97	0.657(519)	0.16(11)	0.81
14	–	–	–	–	–	–
15	0.001(2)	0.183(33)	3.76	2.221(526)	0.070(6)	3.56
16	0.020(18)	0.306(48)	1.88	1.508(256)	0.081(9)	2.00
17	0.027(96)	.536(139)	1.58	0.857(279)	0.093(28)	1.49
18	0.079(517)	0.722(310)	0.57	0.546(448)	0.16(16)	0.47

Table C.8 | Combined fits to $A_{2,i}$ with different p-poles (all results obtained in the $\overline{\text{MS}}$-scheme at $\mu = 2\,\text{GeV}$).

	p	c_0	c_1	d_0	d_1	χ^2/d.o.f.	$M_{2,i}^{\text{phys}}$ [GeV]	$A_{2,i}^{\text{phys}}(0)$
$A_{2,0}$	1	0.260(4)	0.049(5)	1.86(19)	0.70(22)	1.18	1.370(70)	0.261(5)
	2	0.257(4)	0.049(5)	2.19(20)	0.78(23)	1.19	1.484(67)	0.258(5)
	3	0.256(4)	0.049(4)	2.32(21)	0.81(23)	1.23	1.527(68)	0.257(5)
	4	0.256(4)	0.049(4)	2.38(21)	0.83(23)	1.27	1.548(68)	0.257(4)
$A_{2,2}$	1	-0.077(5)	0.019(4)	0.11(27)	2.47(49)	2.27	0.39(27)	-0.076(5)
	2	-0.070(4)	0.016(4)	0.32(38)	3.25(65)	2.35	0.62(26)	-0.070(4)
	3	-0.069(3)	0.015(3)	0.41(42)	3.49(70)	2.38	0.69(26)	-0.068(4)
	4	-0.068(3)	0.015(3)	0.47(44)	3.61(73)	2.39	0.73(26)	-0.068(4)

Acknowledgements

I would like to thank Andreas Schäfer for offering me such an interesting topic for my PhD thesis and for the stimulating discussions we had. I am indebted to Markus Diehl for supervising my work and the opportunity to join the Helmholtz Nachwuchs-Forschergruppe. I also want to thank Gerrit Schierholz for the various discussions and for supporting my visit to Edinburgh.

Furthermore it is a pleasure to thank my colleagues of the QCDSF collaboration for sharing their insights into physics and help with the various technical problems. In particular I should like to mention: Meinulf Göckeler, Philipp Hägler, Roger Horsley, Dirk Pleiter and James Zanotti.

I also do not want to miss the fruitful discussions and help within the DESY theory group, especially: Daniela Amrath, Alessandro Bacchetta, Jan Hamann, Tobias Kleinschmidt, Wolfgang Kugler, Kai Schmidt-Hoberg and Jan Wennekers. Some of you also helped me with proof-reading my thesis and I appreciate that a lot.

This work surely would not have been possible without the gauge configurations generated and provided within the QCDSF, UKQCD and DIK collaborations. Not to forget the computer time on APEmille and apeNEXT to compute the three-point functions. I also acknowledge financial support by the Helmholtz Association and the EU Integrated Infrastructure Initiative “Hadron Physics”.

Finally I want to thank my parents for supporting me over the years and Danni for everything else.

Bibliography

[1] T. Muta, *Foundations of Quantum Chromodynamics*, 2nd ed. (World Scientific Publishing, 2000).

[2] M. E. Peskin and D. V. Schroeder, *An Introduction to Quantum Field Theory* (Perseus Books, 1995).

[3] F. Halzen and A. D. Martin, *Quarks and Leptons: An Introductory Course in Modern Particle Physics* (John Wiley & Sons, 1984).

[4] R. W. Mcallister and R. Hofstadter, Phys. Rev. **102**, 851 (1956).

[5] E. D. Bloom *et al.*, Phys. Rev. Lett. **23**, 930 (1969); M. Breidenbach *et al.*, Phys. Rev. Lett. **23**, 935 (1969).

[6] Particle Data Group Collaboration, W. M. Yao *et al.*, J. Phys. **G33**, 1 (2006).

[7] K. Wijesooriya, P. E. Reimer, and R. J. Holt, Phys. Rev. **C72**, 065203 (2005), nucl-ex/0509012.

[8] M. Glück, E. Reya, and I. Schienbein, Eur. Phys. J. **C10**, 313 (1999), hep-ph/9903288.

[9] R. K. Bhaduri, *Models of the Nucleon: From Quarks to Soliton* Volume 22 of *Lecture notes and supplements in physics* (Addison-Wesley, 1988); F. E. Close, *An Introduction to Quarks and Partons* (Academic Press, 1979).

[10] European Muon Collaboration, J. Ashman *et al.*, Phys. Lett. **B206**, 364 (1988); European Muon Collaboration, J. Ashman *et al.*, Nucl. Phys. **B328**, 1 (1989).

[11] X.-D. Ji, Phys. Rev. **D55**, 7114 (1997), hep-ph/9609381.

[12] D. Boer and P. J. Mulders, Phys. Rev. **D57**, 5780 (1998), hep-ph/9711485.

[13] D. W. Sivers, Phys. Rev. **D43**, 261 (1991).

[14] M. Burkardt, Int. J. Mod. Phys. **A18**, 173 (2003), hep-ph/0207047; M. Burkardt and D. S. Hwang, Phys. Rev. **D69**, 074032 (2004), hep-ph/0309072.

[15] A. V. Belitsky and A. V. Radyushkin, Phys. Rept. **418**, 1 (2005), hep-ph/0504030.

[16] M. Diehl, Phys. Rept. **388**, 41 (2003), hep-ph/0307382.

[17] M. Burkardt, Phys. Rev. **D62**, 071503 (2000), hep-ph/0005108.

[18] J. C. Collins and A. Freund, Phys. Rev. **D59**, 074009 (1999), hep-ph/9801262.

[19] J. P. Ralston and B. Pire, Phys. Rev. **D66**, 111501 (2002), hep-ph/0110075.

[20] A. V. Belitsky and D. Müller, Nucl. Phys. **A711**, 118 (2002), hep-ph/0206306.

[21] M. Diehl, Eur. Phys. J. **C25**, 223 (2002), hep-ph/0205208, Erratum-ibid. **C31**, 277 (2003).

[22] X.-D. Ji and R. F. Lebed, Phys. Rev. **D63**, 076005 (2001), hep-ph/0012160.

[23] P. Hägler, Phys. Lett. **B594**, 164 (2004), hep-ph/0404138.

[24] W. Greiner and J. Reinhardt, *Field Quantization* (Springer, 1996).

[25] M. Diehl and P. Hägler, Eur. Phys. J. **C44**, 87 (2005), hep-ph/0504175.

[26] X.-D. Ji, J. Phys. **G24**, 1181 (1998), hep-ph/9807358.

[27] K. G. Wilson, Phys. Rev. **D10**, 2445 (1974).

[28] I. Montvay and G. Münster, *Quantum Fields on a Lattice* (Cambridge University Press, 1997); H. J. Rothe, *Lattice gauge theories: An Introduction* (World Scientific Publishing, 2005).

[29] S. Duane, A. D. Kennedy, B. J. Pendleton, and D. Roweth, Phys. Lett. **B195**, 216 (1987).

[30] K. G. Wilson, New Phenomena In Subnuclear Physics. Part A. Proceedings of the First Half of the 1975 International School of Subnuclear Physics, Erice, Sicily, July 11 - August 1, 1975, ed. A. Zichichi, Plenum Press, New York, 1977, p. 69, CLNS-321.

[31] P. H. Ginsparg and K. G. Wilson, Phys. Rev. **D25**, 2649 (1982).

[32] P. Hasenfratz and F. Niedermayer, Nucl. Phys. **B414**, 785 (1994), hep-lat/9308004.

[33] C. Gattringer, Phys. Rev. **D63**, 114501 (2001), hep-lat/0003005; C. Gattringer, Nucl. Phys. Proc. Suppl. **119**, 122 (2003), hep-lat/0208056; C. Gattringer, I. Hip, and C.B. Lang, Nucl. Phys. **B597**, 451 (2001).

[34] D. B. Kaplan, Phys. Lett. **B288**, 342 (1992), hep-lat/9206013; Y. Shamir, Nucl. Phys. **B406**, 90 (1993), hep-lat/9303005.

[35] H. Neuberger, Phys. Lett. **B417**, 141 (1998), hep-lat/9707022; H. Neuberger, Phys. Lett. **B427**, 353 (1998), hep-lat/9801031.

[36] B. Sheikholeslami and R. Wohlert, Nucl. Phys. **B259**, 572 (1985).

[37] ALPHA Collaboration, K. Jansen and R. Sommer, Nucl. Phys. **B530**, 185 (1998), hep-lat/9803017.

[38] S. Basak *et al.*, Phys. Rev. **D72**, 094506 (2005), hep-lat/0506029.

[39] UKQCD Collaboration, C. R. Allton *et al.*, Phys. Rev. **D47**, 5128 (1993), hep-lat/9303009.

[40] C. Alexandrou, S. Gusken, F. Jegerlehner, K. Schilling, and R. Sommer, Nucl. Phys. **B414**, 815 (1994), hep-lat/9211042.

[41] C. Best *et al.*, Phys. Rev. **D56**, 2743 (1997), hep-lat/9703014.

[42] T. Burch *et al.*, PoS **LAT2005**, 097 (2006), hep-lat/0509086.

[43] M. Göckeler *et al.*, Phys. Rev. **D54**, 5705 (1996), hep-lat/9602029.

[44] QCDSF Collaboration, M. Göckeler, R. Horsley, D. Pleiter, P. E. L. Rakow, and G. Schierholz, Phys. Rev. **D71**, 114511 (2005), hep-ph/0410187.

[45] S. Capitani *et al.*, Nucl. Phys. **B593**, 183 (2001), hep-lat/0007004.

[46] M. Guagnelli and R. Sommer, Nucl. Phys. Proc. Suppl. **63**, 886 (1998), hep-lat/9709088.

[47] QCDSF-UKQCD Collaboration, T. Bakeyev *et al.*, Phys. Lett. **B580**, 197 (2004), hep-lat/0305014.

[48] M. Göckeler *et al.*, Nucl. Phys. **B472**, 309 (1996), hep-lat/9603006.

[49] R. Sommer, (1997), hep-ph/9711243.

[50] M. Göckeler *et al.*, Nucl. Phys. **B544**, 699 (1999), hep-lat/9807044.

[51] G. Martinelli, C. Pittori, C. T. Sachrajda, M. Testa, and A. Vladikas, Nucl. Phys. **B445**, 81 (1995), hep-lat/9411010.

[52] T. Draper, R. M. Woloshyn, W. Wilcox, and K.-F. Liu, Nucl. Phys. **B318**, 319 (1989).

[53] W. Wilcox, T. Draper, and K.-F. Liu, Phys. Rev. **D46**, 1109 (1992), hep-lat/9205015.

[54] S. Capitani *et al.*, Nucl. Phys. Proc. Suppl. **73**, 294 (1999), hep-lat/9809172.

[55] LHPC and SESAM Collaboration, Ph. Hägler *et al.*, Phys. Rev. **D68**, 034505 (2003), hep-lat/0304018.

[56] R. Sommer, Nucl. Phys. **B411**, 839 (1994), hep-lat/9310022; ALPHA Collaboration, M. Guagnelli, R. Sommer, and H. Wittig, Nucl. Phys. **B535**, 389 (1998), hep-lat/9806005.

[57] A. Ali Khan *et al.*, (2006), hep-lat/0603028.

[58] C. Aubin *et al.*, Phys. Rev. **D70**, 094505 (2004), hep-lat/0402030.

[59] G. Schierholz, *private communication*.

[60] T. Bhattacharya, R. Gupta, G. Kilcup, and S. R. Sharpe, Phys. Rev. **D53**, 6486 (1996), hep-lat/9512021.

[61] LHP Collaboration, F. D. R. Bonnet, R. G. Edwards, G. T. Fleming, R. Lewis, and D. G. Richards, Phys. Rev. **D72**, 054506 (2005), hep-lat/0411028.

[62] G. Martinelli and C. T. Sachrajda, Nucl. Phys. **B306**, 865 (1988).

[63] RBC Collaboration, Y. Nemoto, Nucl. Phys. Proc. Suppl. **129**, 299 (2004), hep-lat/0309173.

[64] J. van der Heide, J. H. Koch, and E. Laermann, Phys. Rev. **D69**, 094511 (2004), hep-lat/0312023.

[65] A. M. Abdel-Rehim and R. Lewis, Phys. Rev. **D71**, 014503 (2005), hep-lat/0410047.

[66] Bern-Graz-Regensburg (BGR) Collaboration, S. Capitani, C. Gattringer, and C. B. Lang, Phys. Rev. **D73**, 034505 (2006), hep-lat/0511040.

[67] J. N. Hedditch *et al.*, (2007), hep-lat/0703014.

[68] JLQCD Collaboration, S. Hashimoto *et al.*, PoS **LAT2005**, 336 (2006), hep-lat/0510085.

[69] P. A. Boyle, J. M. Flynn, A. Jüttner, C. T. Sachrajda, and J. M. Zanotti, (2007), hep-lat/0703005.

[70] H. Ackermann *et al.*, Nucl. Phys. **B137**, 294 (1978).

[71] NA7 Collaboration, S. R. Amendolia *et al.*, Nucl. Phys. **B277**, 168 (1986).

[72] The Jefferson Lab F_π Collaboration, J. Volmer *et al.*, Phys. Rev. Lett. **86**, 1713 (2001), nucl-ex/0010009; The Jefferson Lab F_π Collaboration, V. Tadevosyan *et al.*, (2006), nucl-ex/0607007; The Jefferson Lab F_π-2 Collaboration, T. Horn *et al.*, (2006), nucl-ex/0607005.

[73] QCDSF/UKQCD Collaboration, D. Brömmel *et al.*, Eur. Phys. J. **C51**, 335 (2007), hep-lat/0608021.

[74] H. B. O'Connell, B. C. Pearce, A. W. Thomas, and A. G. Williams, Prog. Part. Nucl. Phys. **39**, 201 (1997), hep-ph/9501251.

[75] S. Sint and P. Weisz, Nucl. Phys. **B502**, 251 (1997), hep-lat/9704001.

[76] G. P. Lepage and P. B. Mackenzie, Phys. Rev. **D48**, 2250 (1993), hep-lat/9209022.

[77] Particle Data Group Collaboration, S. Eidelman *et al.*, Phys. Lett. **B592**, 1 (2004).

[78] L. Del Debbio, L. Giusti, M. Luscher, R. Petronzio, and N. Tantalo, JHEP **02**, 056 (2007), hep-lat/0610059.

[79] T. B. Bunton, F. J. Jiang, and B. C. Tiburzi, Phys. Rev. **D74**, 034514 (2006), hep-lat/0607001.

[80] J.-W. Chen, W. Detmold, and B. Smigielski, (2006), hep-lat/0612027.

[81] B. Borasoy and R. Lewis, Phys. Rev. **D71**, 014033 (2005), hep-lat/0410042.

[82] M. Göckeler *et al.*, Phys. Rev. **D73**, 014513 (2006), hep-ph/0502212.

[83] U.-G. Meissner and G. Schierholz, (2006), hep-ph/0611072.

[84] J. Bijnens, G. Colangelo, and P. Talavera, JHEP **05**, 014 (1998), hep-ph/9805389.

[85] G. Colangelo, J. Gasser, and H. Leutwyler, Nucl. Phys. **B603**, 125 (2001), hep-ph/0103088.

[86] P. J. Sutton, A. D. Martin, R. G. Roberts, and W. J. Stirling, Phys. Rev. **D45**, 2349 (1992).

[87] W. Detmold, W. Melnitchouk, and A. W. Thomas, Phys. Rev. **D68**, 034025 (2003), hep-lat/0303015.

[88] Zeuthen-Rome (ZeRo) Collaboration, M. Guagnelli *et al.*, Phys. Lett. **B597**, 216 (2004), hep-lat/0403009.

[89] W. Detmold and C. J. D. Lin, Phys. Rev. **D71**, 054510 (2005), hep-lat/0501007.

[90] M. Diehl, A. Manashov, and A. Schäfer, Phys. Lett. **B622**, 69 (2005), hep-ph/0505269.

[91] M. Diehl, A. Manashov, and A. Schäfer, Eur. Phys. J. **A31**, 335 (2007), hep-ph/0611101.

[92] M. Burkardt and B. Hannafious, (2007), arXiv:0705.1573 [hep-ph].

[93] QCDSF Collaboration, M. Göckeler *et al.*, (2006), hep-lat/0612032.

[94] M. Göckeler, *private communication*.